THE DECAY OF KRYPTON 89

THE DECAY OF KRYPTON 89

by

WILLIAM FREDERICK SKIPPER POEHLMAN, B.S., B.Sc.

A Thesis
Submitted to the Faculty of Graduate Studies
in Partial Fulfilment of the Requirements
for the Degree
Master of Science

McMaster University
April 1972

MASTER OF SCIENCE (1972)
(Physics)

MCMASTER UNIVERSITY
Hamilton, Ontario

TITLE:	The Decay of Krypton 89
AUTHOR:	William Frederick Skipper Poehlman, B.S. (Niagara University), B.Sc. (Brock University)
SUPERVISOR:	Dr. M.W. Johns
NUMBER OF PAGES:	viii, 177

SCOPE AND CONTENTS:

The decay of 3.5 minute ^{89}Kr to levels in ^{89}Rb has been investigated with small and large volume Ge(Li) detectors used singly and in coincidence. A total of 160 gamma rays have been attributed to the nuclear process, 120 of which have been incorporated into a proposed decay scheme.

ACKNOWLEDGEMENTS

I wish to express my appreciation to Professor M.W. Johns for his support and guidance. I would also like to thank Dr. B. Singh. Not only has he aided me in exploring the subtleties of nuclear spectroscopy but he has assisted in a major portion of the data analysis.

The many valuable discussions and generous assistance provided me by the members of the beta and gamma ray spectroscopy group, with whom I have been associated, is gratefully acknowledged. Without their help many phases of this work would have been impossible.

It is a pleasure to thank the staff of the McMaster reactor for their assistance in the inumerable sample irradiations. I am especially indebted to the operators for their patience and friendship.

I am very grateful to Jan whose speed and accuracy in the typing of this manuscript have been of great value in the completion of this work.

Also, I would like to thank my parents who have undergone a considerable amount of personal sacrifice so that I might have the opportunity of this education.

Financial support for this project has come from the National Research Council of Canada.

TABLE OF CONTENTS

CHAPTER 1 GENERAL CONCEPTS

CHAPTER 2 DATA ACQUISITION

CHAPTER 3 THE DECAY OF KRYPTON 89

LIST OF FIGURES

LIST OF TABLES

CHAPTER 1

General Concepts

Introduction

Nuclear physics delegates to itself the fundamental problem of understanding, within a theoretical structure, the sub-atomic domain of the nucleus. This is no mean task. The enormous number of variables involved make any direct calculation of the observed properties of nuclear states belonging to the nucleus quite impossible. Thus, the problem is approached piecemeal via the method of models. Physicists have proposed models to explain selected properties of the nuclear states as observed experimentally.

At the present time, different classes of nuclei are best described by different types of models. The nuclear shape provides one useful criterion for classification. Nuclei with a spherical equilibrium shape seem to fit shell and vibrational models. Nuclei with a permanent deformation seem to fit either the rotational or the Nilsson model. Since the shell and vibrational models are the most useful in dealing with the mass region of interest in this thesis, they are discussed in more detail in the following section.

A. Nuclear Models

Observable nuclear properties are a direct result of nucleon interactions which in turn are determined by the nuclear force or potential between nucleons. It is this potential that serves as a starting point for every new nuclear model.

Prior to 1949, the most common potential in use was a central potential, $V(\mathbf{r})$, of either the harmonic oscillator or modified square well type (Green, Sawada and Saxon (1968)). The harmonic oscillator (Powell and Craseman (1961)) was used because of the analytical convenience of its wave functions. The square well potential (Merzbacker (1961)) was developed because it possessed much the same form as the charge density of the nucleus. The solution of the Schroedinger equation with the potentials led to nuclear states or energy levels characterized by three quantum numbers--(n,ℓ,j). These constants of the particle motion represent the orbital angular momentum (ℓ), the total angular momentum (j) and the number of nodes (n) of the radial wavefunction in the solution. However, these results, as illustrated in figure 1-1 failed to account for the behaviour of actual nuclei, and in particular to explain the extra stability associated with nuclei containing certain specified neutron and proton numbers. These "magic numbers" could be explained if the model could create a large gap in the predicted level spacing. Thus "closed shell" effects would be expected when all the levels up to this gap had been filled. The experimental data indicates that special stability is associated with proton and neutron numbers of 2, 8, 20, 50, 82, and 126.

1.1 Shell Models

The simplest shell model which came close to fitting the experimental data was that developed originally by Mayer (1949,1950) and independantly by Haxel, Jensen and Suess (1949,1950). Both groups assumed that each nucleon moved in the static central potential, V(r), created by the averaged interaction among the other nucleons, but, they added a strong spin-orbit (s-ℓ) coupling term. Hence, the simple central potential was modified to

$$V = V(r) - f(r)\ \vec{l} \cdot \vec{s}$$

This spin-orbit term results in the splitting of each level into two states corresponding to the two possible values of j which are present for each ℓ-value. If f(r) is a positive quantity, then the states with $j = \ell + \frac{1}{2}$ are depressed from the original position, while the states with $j = \ell - \frac{1}{2}$ are raised. By empirically adjusting f(r), the interaction strength, the experimentally observed level ordering was obtained (Mayer and Jensen (1966)). Since the magnitude of the splitting increases with the value of ℓ, the effect of the $s - \ell$ interaction is to depress the higher angular momentum states so that they fall within the adjacent shell to create a "gap" in the level spacing and make possible a "closed shell" just below this gap.

The proposed potential is still spherically symmetric so that ℓ and j remain constants of motions for the system. There may, however, be a degeneracy in energy of several of these states as well as a denerac y with respect to the orientation of the total angular momentum (characterized by the quantum number, m_j). Thus an energy (n,ℓ,j) state is actually a superposition of $(2j + 1)$ states, each with its own unique value of m_j.

Figure 1.1 compares the level spacing for a variety of potentials. Column V shows the result of adding the $s - \ell$ term to the square well potential. It illustrates very clearly the gaps in the level spacing created by the spin-orbit force. Because of Pauli's principle, each (n,ℓ,j) state can contain at most $2j + 1$ particles. Therefore, the number of particles needed to completely fill the level structure up to each gap can easily be calculated. These values, the so-called magic numbers are given in the last column of the table.

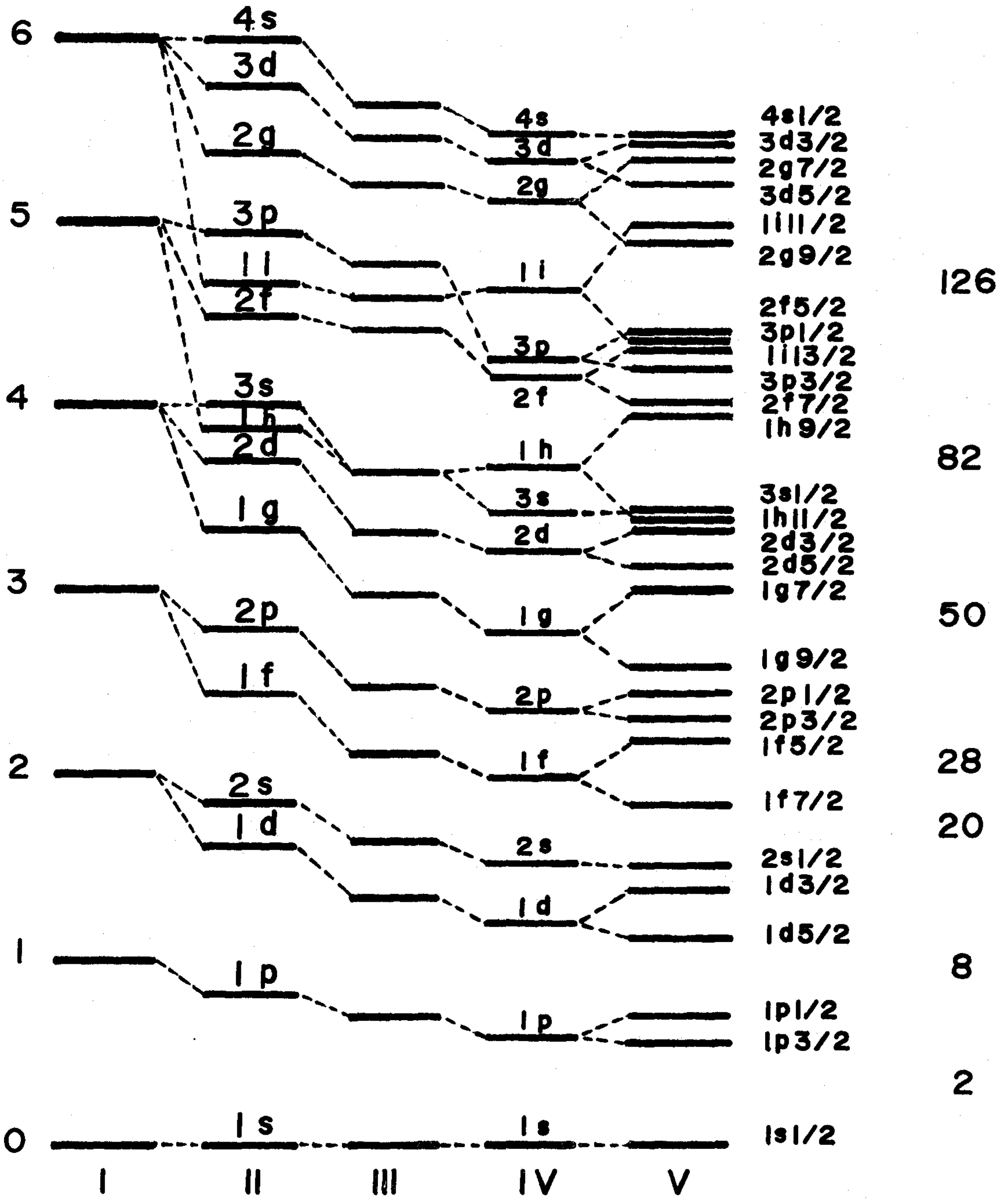

Figure 1.1 Ordering of energy levels according to the shape of the nuclear potential: I. Harmonic oscillator; II. Infinite square well; III. Finite square well; IV. Square well with rounded edges; V. (IV) plus spin orbit coupling.

The aforementioned model is usually termed the extreme single-particle shell model because the potential is assumed to be due to all the other nucleons of the nucleus through which a single unpaired nucleon moves. It is this single particle to which the properties of the nucleus are ascribed.

1.2 Extreme Single-Particle Model

This model assumes that the neutron and proton states fill independently. Hence, the structure of any nucleus is determined by filling the lowest possible energy levels with neutrons and protons until all the particles have been accounted. Figure 1.2 shows the generally accepted ordering of levels for both neutrons and protons. It is noted that there are slight variations in level ordering between the two. These minor inversions in levels are due to the additional energy of coulomb repulsion in the proton group.

Another assumption of this model concerns pairing effects. Whenever any two nucleons with the same (n,ℓ,j) quantum numbers occur, they tend to couple to form an "inert pair" having zero resultant angular momentum and a very stable energy configuration.

The greatest triumph of this model came with the prediction of spin and parities for the ground state of

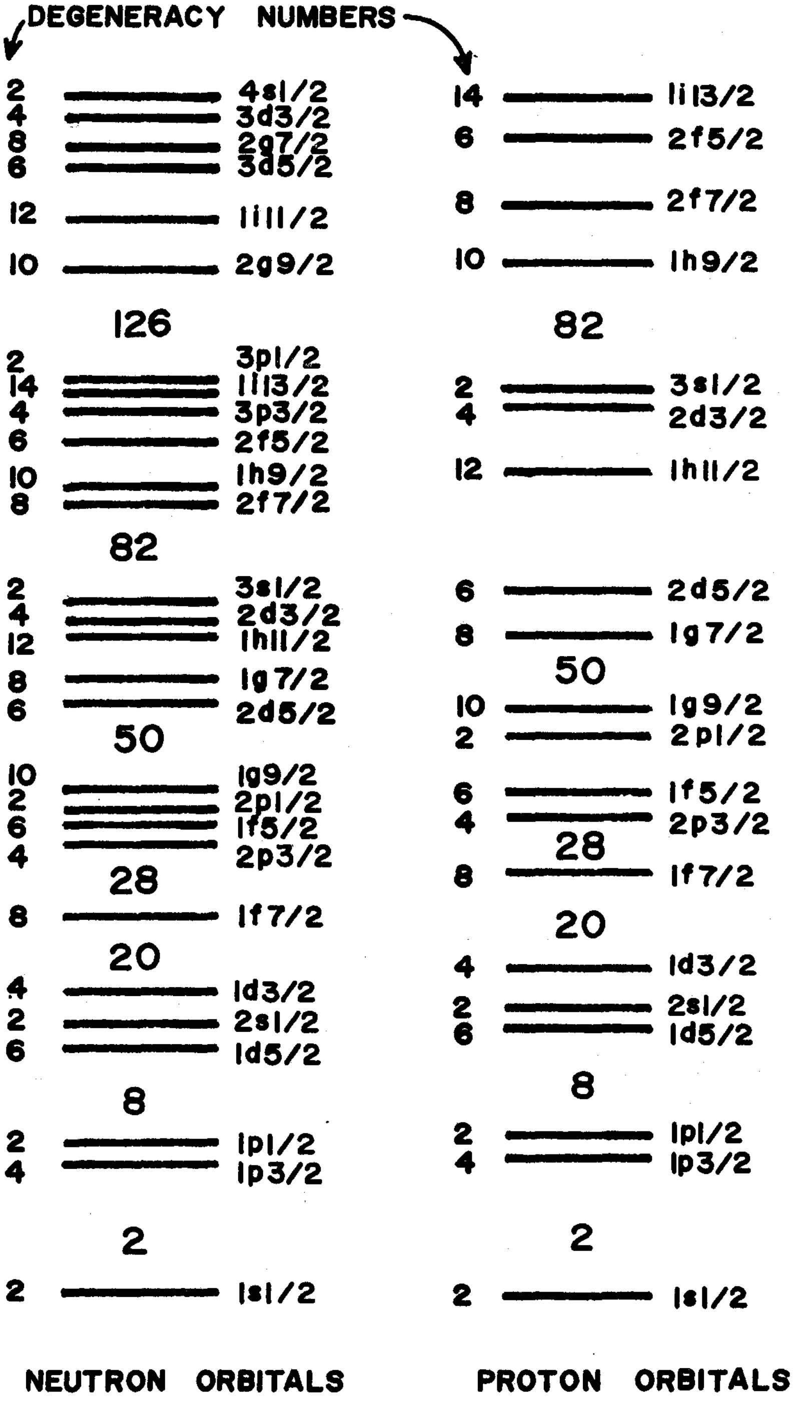

Figure 1.2 Filling order of nuclear orbitals via the shell model.

even-even and odd-even (or even-odd) nuclei. For even-even nuclei all protons and neutrons separately couple pairwise to zero spin. Due to the symmetry of such a configuration, the system exhibits positive parity. This prediction of $J^\pi = 0+$ ground states for all even-even nuclei has been confirmed experimentally. For odd-A nuclei, it is generally found that the experimentally determined J^π of the ground state is given by the J^π of the last unpaired particle as predicted by the level ordering of the model. However, for odd-odd nuclei, the predictions are not so unique. Elaborate rules have been developed empirically (Brennan and Bernstein, 1960) as an aid to configuration determinations. In such a case the lone particles of each group combine in various ways as described by these rules to give a selection of resultant J values of like parity.

Much the same type of analysis is involved in the interpretation of low lying excited state properties. Excited states are formed by promoting one or more nucleons into the higher lying levels which are unoccupied. For even-even nuclei, a single nucleon jumping into a higher shell forms a particle-hole pair. These entities present the same type of problem with respect to J^π coupling as encountered for the odd-odd ground state nucleus above.

Thus, certain assignments become ambiguous in this area. For odd-A nuclei, the predictions are less troublesome to glean from the model. In this case, the excitations are usually due to the promotion of the unpaired particle into an unoccupied state. The resulting nuclear states are then characterized by a J^{π} of the unpaired particle or hole. Although the extreme single-particle model has had great successes in its ability to reproduce easily and understandably some observed experimental facts, the complex level structure of many nuclei have revealed its shortcomings. One of the first improvements to be proposed was the "single-particle model."

1.3 Single Particle Model

The single particle model offers a more realistic approach to the problem of the nuclear potential by including the interactions between all nucleons within a partially filled shell. In this model, the particles in closed shells are considered to be inert while those loose particles outside the filled shell are described by a residual interaction term added to the simple shell model potential. The result of calculations using this potential essentially yields a mixed wave function. By this is meant that the procedure admixes other states into the wave function of interest using the technique of configuration mixing. If the calculation confines the nucleons to a single (n,ℓ,j) state, then the state is deemed pure since no configuration mixing occurs.

Although the shell model has been reasonably successful in forecasting ground state spins and parities, it has been shown to be inadequate in dealing with such quantities as magnetic moments, quadrupole moments, transition probabilities, and the spins and parities of excited states. These quantities are better described in terms of a model based on the collective behaviour of many of the nucleons in the nucleus.

1.4 Collective Motions

In addition to the single particle excitations discussed above, the nucleons in an unfilled shell may interact to produce collective effects which involve the vibrational and rotational degrees of freedom of the nucleus. For nuclei far from a closed shell configuration, the interaction between these many particles results in the nucleus exhibiting a permanent deformation. The nucleus can now be treated as a rigid rotator, yielding a rotational level structure similar to that observed in molecular spectra. However, the nucleus involved in this investigation possesses neutron and proton numbers near to to a closed shell so that these effects are irrelevant. Instead, the nucleus tends to oscillate about its spherical equilibrium shape, in a vibratory manner. Accordingly, a description of the vibrational model follows.

1.5 Vibrational Model

The significant features of a system whose cohesion results from the mutual attraction of the particles were realized in an earlier era through the liquid drop nuclear model. The assumptions used there were incorporated into the vibrational model as developed by Bohr and Mottelson (1953). These include treating the nucleus microscopically as a deformable liquid drop interacting with the unpaired nucleons of the unfilled shell. The nuclear matter is treated as an incompressible fluid without internal structure. This results in suppression of all details concerning particle structure.

In this model the particles outside the core are visualized as moving through many orbits, but in such a sufficiently correlated manner that the over-all space pattern of the surface is slowly changing. Hence, since the surface is distorted at some moment, the potential felt by a particle is not spherically symmetric. This entire process can be described by saying that the particle motion and core surface motion are coupled. In the mathematical expression of this coupling there is a need to introduce collective variables which describe the cooperative modes of motion. Therefore, the nucleus is expanded in terms of the spherical harmonics,

$$Y(\theta,\phi):R(\theta,\phi) = R_o[1 + \sum_{\lambda=0}^{\infty} \sum_{\mu=-\lambda}^{\lambda} \alpha_{\lambda\mu} Y_{\lambda}^{\mu}(\theta,\phi)]$$

where R represents the surface of the vibrating nucleus that normally has an equilibrium shape radius of R_o. This radius is a function of θ and ϕ which are the polar angles with respect to some fixed frame of reference. Any collective motions can now be expressed by time variations imposed on the collective deformation variable $\alpha_{\lambda\mu}$.

The simplest variation of this model considers the nuclear oscillation to be harmonic. In this case, the vibrational motion is that of a surface wave circulating around the nucleus and is characterized by a frequency of ω_λ. These vibrations are called phonons of order λ and have associated with them an angular momentum, λ, and a parity of $(-1)^{-1}$. Being simple harmonic in nature, this type of model predicts excited states at energies:

$$E_{n\lambda} = n_\lambda \hbar \omega_\lambda \qquad n = 1,2,3, \ldots$$

For $\lambda = 1$ the vibrations are simple due to oscillations of the mass center of the nucleus which is not an internal degree of freedom. Hence, this motion cannot be observed experimentally. For $\lambda = 2$, termed quadrupole vibrations, a $J^{\pi} = 2+$ state of energy ω_2 is predicted. For $\lambda = 3$ or octupole vibrations, a $J^{\pi} = 3-$ state is forecast at energy ω_3. Perhaps it should be noted here that a one-phonon-octupole vibration is approximately equal in energy to a coupled two-phonon quadrupole state. Thus, at this energy (that is, $h\omega_3 \sim 2h\omega_2$), in addition to the 3- octupole state, levels of $J^{\pi} = 0+$, 2+, or 4+ are predicted due to the coupling of the two quadrupole phonons. The two-phonon state is degenerate in the simple harmonic approximation described here but in actuality this degeneracy is usually lifted through perturbations created by second order calculations. This results in a multiplet, as illustrated in figure 1.3. There seem to be relatively few vibrational nuclei for which the entire triplet of states have been experimentally observed. Since the level energy, ω_{λ}, is a rapidly increasing function of λ, only small values of λ need be considered in the examination of low lying nuclear states.

For even-even near-spherical nuclei the sets of states in figure 1.3 account for all the low lying states. For odd-A nuclei, the situation is somewhat more complex since the vibrational states and intrinsic single particle

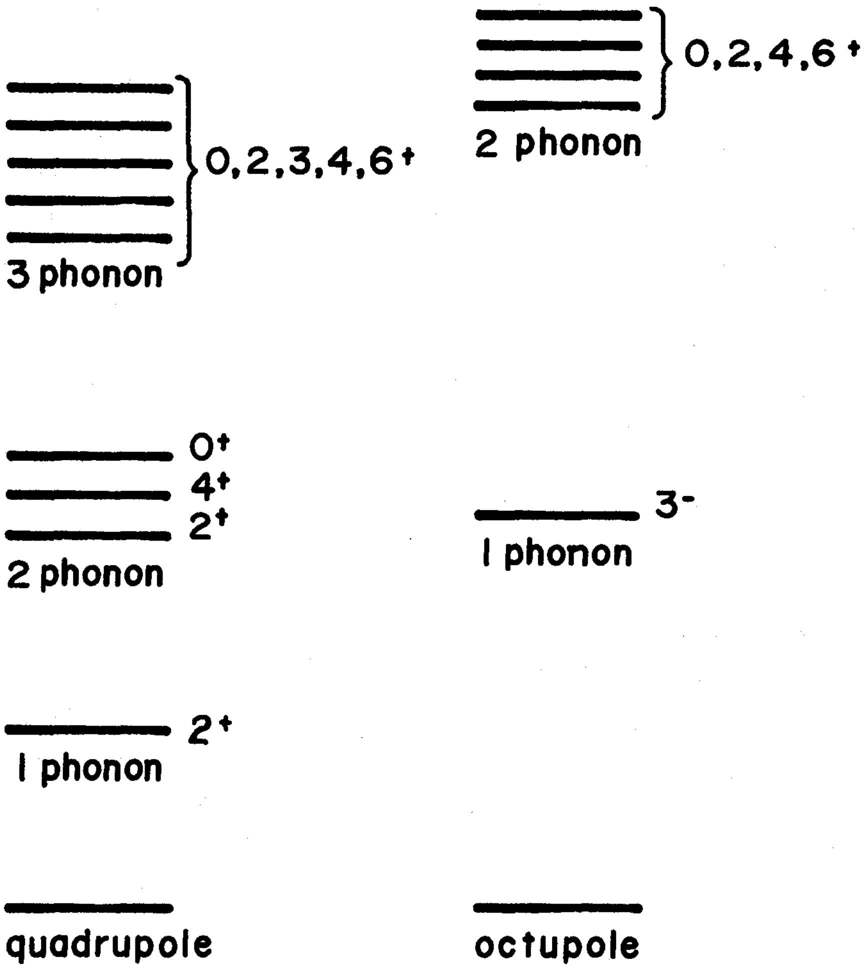

Figure 1.3 Vibrational energy level spectrum.

states now interact through the coupling of the particle and vibrational angular moments. The resultant angular momentum of any given state is then determined by rules similar to those mentioned in the shell model. However, in practice, it is useful only to consider couplings of the low-lying levels of the 2+ quadrupole vibration and the intrinsic states.

In an effort to give the vibrational model a larger region of application in terms of odd-A nuclei, De-Shalit (1961) has recently proposed a core excitation model. The basic tenets of the calculation include: i) the coupling of the collective excitation of the core to the odd nucleon rather than considering the coupling of phonons with the particle states, and ii) the assumption that the core excitation of the nucleus at hand has excited states corresponding in properties (eg., 2+ first excited state) to the core excitation in the neighbouring even-even nucleus.

B Radioactive Decay

In the previous section, an outline of some of the current theories of nuclear structure has been provided. However, this is not the whole story. As mentioned in the introduction of this work, the study of the structure of nuclei can only proceed through the observation of actual nuclear behaviour. Perhaps the most readily observable property is radiation that arises when an unstable nuclear configuration is altered to a more stable one. This section will deal with the production and properties of these radiations.

1.6 Fission

Fission is the process whereby a heavy nucleus gains greater stability by separating into two large fragments. In 1939 O. Hahn and L. Strassemann found alkaline earth metals were produced when uranium was irradiated with neutrons. The origin of these products was first accounted for by L. Meitner and O.R. Frisch (1939) who proposed that when a uranium nucleus absorbed a neutron, it underwent fission producing two fragments. Once the mechanism was understood in general terms, the attention of chemists and physicists (Anderson, Fermi, and Grosse, 1940) quickly turned to the determination of the type, including element, mass, and charge, as well as yields of fission fragments associated with this process. This work can be partially summarized in the fission yield curve of figure 1.4 which shows how the probability of fission depends on mass number for U233 and Pu239 (Katcoff(1960)). As illustrated by these curves it is apparent that large changes in yield occur for

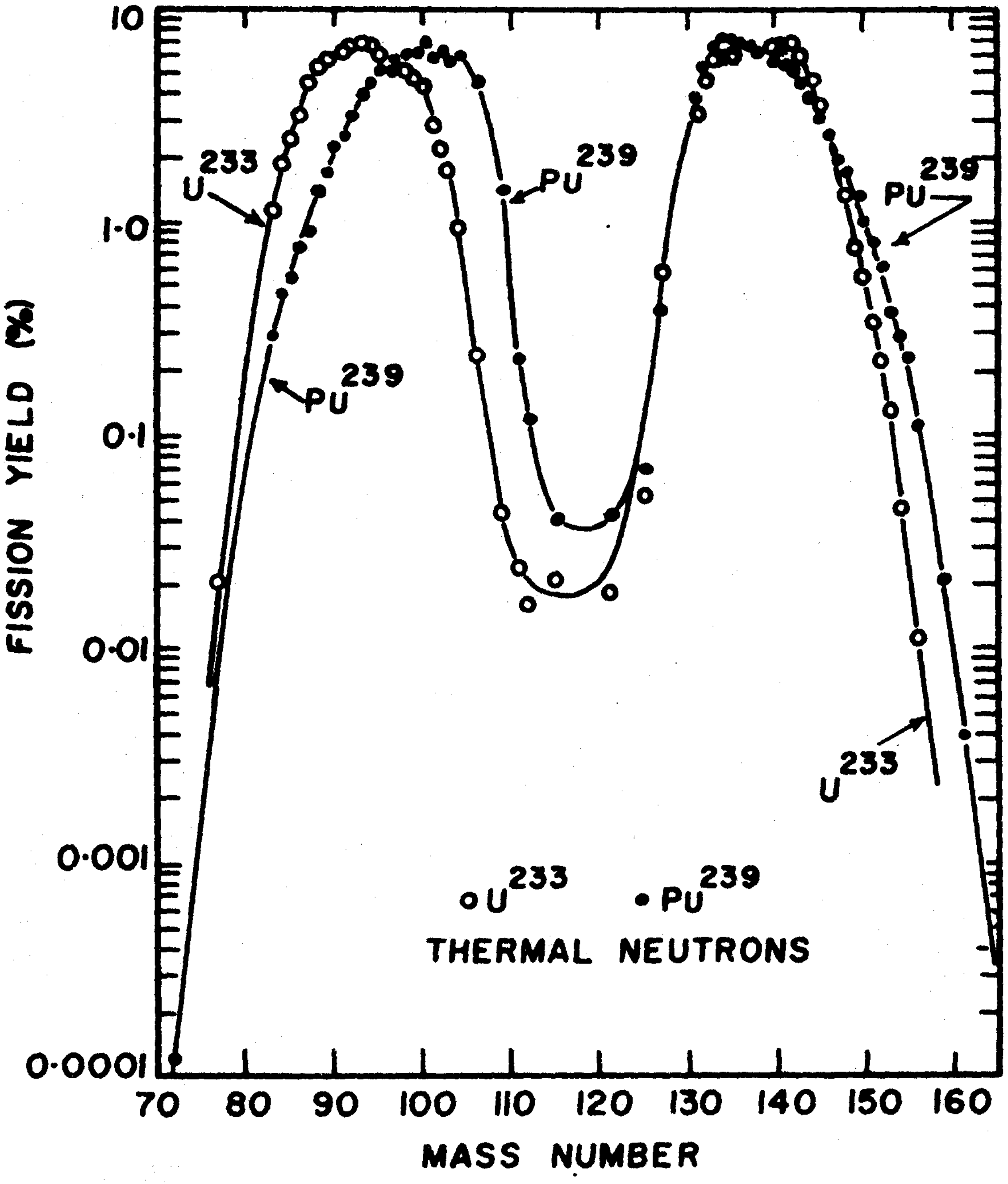

Figure 1.4 Frequency distribution of mass number of fission fragments from fission of U^{233} and Pu^{239}.

relatively small changes in the mass of the fissile material. It became clear very early in these investigations that fission by slow or thermal neutrons is an asymmetric process. That is, most of the fission yield is associated with a light group of nuclei having $85 \leq A \leq 104$ or with a heavy group having $130 \leq A \leq 149$. Together these two groups account for 97 per cent of the fission process (Arya (1966)). It is also clear from the figure that the fission yield at mass 89 is greater for U233 than for a heavier nucleus such as Pu239. Thus, U233 was used as a source of the ^{89}Kr nuclei.

In a similar manner, the fission fragments are also distributed with respect to charge for a given mass. Recent investigations seem to indicate that this distribution is best described by a Gaussian function whose width is constant for all masses (Wolfsberg (1965)); (Norris and Wahl (1966)); (Wahl, Norris, and Ferguson (1966)). Thus the probability of finding a specific Z value in spontaneous fission is

$$P(Z) = (c^{\pi})^{-1/2} \exp\,[-(Z-Z_p)^2 /c]$$

(Wahl, Ferguson, Nethaway, Troutner,
and Wolfsberg (1962)).

where $c \approx 2(\sigma^2)$; $\sigma (\approx 0.59)$ is the variance of the distribution and Z_p is the most probable charge for a given mass chain.

1.7 Fission Products

All heavy fissionable nuclei have neutron excesses. Therefore, when they undergo fission, the resultant products are so neutron rich relative to the adjacent stable nuclei that they decay by successive beta decays until the neutron number reaches a value associated with a stable nucleus. Since the energies involved in these beta decays are large, the process leads to the population of highly excited states in the daughter elements formed by the decay. De-excitation of these states proceeds almost entirely by gamma ray emission so that the decay schemes of such nuclei are expected to be very complex. Another consequence of the large energy release in these successive beta decays is that the nuclides involved have very short half lives. In fact, the decay chain members following fission are characterized, in most cases, by gradually increasing half lives, lower excitation energies and increasing Z until a stable nucleus of the chain is reached. Since the krypton element is of main interest here, table 1.1 presents a chart of the half lives of some members of the krypton decay chains (Kitching (1966)).

1.8 Beta Decay

A nucleus in a very highly excited state loses its energy by nucleon emission. While the emission of a single

TABLE 1.1

Krypton Isotope Decay Chains

$^{95}\mathrm{Kr} \xrightarrow{\text{(short)}}$	$^{95}\mathrm{Rb} \xrightarrow{\leq 2\text{ sec}}$	$^{95}\mathrm{Sr} \xrightarrow{33\text{ sec}}$	$^{95}\mathrm{Y} \xrightarrow{11\text{ min}}$
$^{94}\mathrm{Kr} \xrightarrow{\leq 1\text{ sec}}$	$^{94}\mathrm{Rb} \xrightarrow{2\text{ sec}}$	$^{94}\mathrm{Sr} \xrightarrow{82\text{ sec}}$	$^{94}\mathrm{Y} \xrightarrow{20\text{ min}}$
$^{93}\mathrm{Kr} \xrightarrow{1\text{ sec}}$	$^{93}\mathrm{Rb} \xrightarrow{5\text{ sec}}$	$^{93}\mathrm{Sr} \xrightarrow{8\text{ min}}$	$^{93}\mathrm{Y} \xrightarrow{10\text{ hr}}$
$^{92}\mathrm{Kr} \xrightarrow{2\text{ sec}}$	$^{92}\mathrm{Rb} \xrightarrow{4\text{ sec}}$	$^{92}\mathrm{Sr} \xrightarrow{3\text{ hrs}}$	$^{92}\mathrm{Y} \xrightarrow{4\text{ hrs}}$
$^{91}\mathrm{Kr} \xrightarrow{8\text{ sec}}$	$^{91}\mathrm{Rb} \xrightarrow{72\text{ sec}}$	$^{91}\mathrm{Sr} \xrightarrow{10\text{ h}}$	$^{91}\mathrm{Y} \xrightarrow{59\text{ d}}$
$^{90}\mathrm{Kr} \xrightarrow{32\text{ sec}}$	$^{90}\mathrm{Rb} \xrightarrow{3\text{ min}}$	$^{90}\mathrm{Sr} \xrightarrow{28\text{Y}}$	$^{90}\mathrm{Y} \xrightarrow{64\text{ hrs}}$
$^{89}\mathrm{Kr} \xrightarrow{3\text{ min}}$	$^{89}\mathrm{Rb} \xrightarrow{15\text{ min}}$	$^{89}\mathrm{Sr} \xrightarrow{50\text{ d}}$	$^{89}\mathrm{Y}\ \underline{\text{Stable}}$
$^{88}\mathrm{Kr} \xrightarrow{2\text{ hr}}$	$^{88}\mathrm{Rb} \xrightarrow{18\text{ min}}$	$^{88}\mathrm{Sr}\ \underline{\text{Stable}}$	
$^{87}\mathrm{Kr} \xrightarrow{76\text{ min}}$	$^{87}\mathrm{Rb} \xrightarrow{4.7\text{x}10^{10}\text{Y}}$	$^{87}\mathrm{Sr}\ \underline{\text{Stable}}$	
$^{86}\mathrm{Kr}\ \underline{\text{Stable}}$			
$^{85m}\mathrm{Kr} \xrightarrow{4\text{ hr}}$	$^{85}\mathrm{Rb}\ \underline{\text{Stable}}$		

neutron or proton is most common, in fission, clusters of nucleons are emitted as fragments with energies of the order of hundreds of MeV. These fragments are highly unstable and may lose energy by particle emission or if the energy is less than ~5 MeV, by a succession of beta decays, as described above.

Beta decay proceeds by an interaction which encompasses three types of occurrences listed below:

i) $n \rightarrow p + e^- + \bar{\nu}$ --electron decay

Here, neutron rich nuclei decay through the transformation of a neutron into a proton (which remains in the nucleus causing an internal charge and structure rearrangement) and an electron and anti-neutrino pair which is ejected from the nucleus.

ii) $p \rightarrow n + e^+ + \nu$ --positron decay

In this case, a proton changes into a neutron with the emission of a position and neutron pair.

iii) $p + e^- \rightarrow n + \nu$ --electron capture decay

This reaction describes the capture of an orbital electron by a proton which transforms into a neutron with the emission of a neutrino.

All types of beta decay are assumed to be due to a universal weak interaction, so-called, because it is much weaker than other interactions which occur in nature.

The structure of the universe can largely be described in terms of the strong interaction, involving nuclear forces, the electromagnetic interaction between electric charges, the weak interaction, manifesting itself in beta decay, and the gravitational interaction. Their relative strengths are, respectively,
$1: 1/_{1370} : 10^{-24} : 10^{-46}$ (Preston (1962)).
Because the beta decay process involves the emission of an electron-neutrino pair, the available energy is divided between the electron and the neutrino to give a continuous energy distribution from zero to the maximum energy possible for each. This energy is termed the end-point energy in the beta spectrum and therefore is a measure of the energy available to the beta decay process.

The first realistic model of beta decay was proposed by Pauli in 1934. He hypothesized a three body process involving electron, proton, and a neutrino. The properties of the neutrino, zero charge, intrinsic spin 1/2, and zero rest mass are such as to make its detection very difficult. Direct observation of this elusive particle was finally achieved by Cowan and Reines in 1957.

The theory of beta decay was developed by Fermi (1934) using the main components of Pauli's hypothesis. These results still stand, although the beta decay operators used by him have been modified. This came about from a series of experiments (eg. Wu, et. al. (1957) concerning parity non-conservation in beta decay which were sparked by the proposal of Lee and Yang (1957) that none of the earlier experiments had tested conservation of parity in the weak interaction. As a result of these experiments, it is now clear that the weak interaction operator is of mixed parity and that therefore the principle of conservation of parity, which seems to hold for the strong and electromagnetic interaction is not valid for the weak interaction.

The transition probability, T, for beta decay is given by the so-called Fermi Golden Rule #2 (Eisberg (1964)):

$$T(E) = \frac{2\pi}{\lambda} \left| < \psi_f \left| M_\beta \right| \psi_i > \right|^2 \rho(E) \qquad 1.1$$

where ψ_i and ψ_f represent the initial (neutron) and the final (proton, electron, and neutrino), state wave functions respectively, H_β is the weak interaction Hamiltonian and $\rho(E)$ is the density of final states. Upon integrating the transition probability over suitable variables, the beta decay process becomes (Segre (1964)),

$$N(p)\ dp \propto \left| M_{if} \right|^2 F(z,p) p^2 (E_o - E)^2 S_n dp \qquad 1.2$$

where N(p)dp is the probability that the beta particles are emitted with momentum between p and p+dp. In this expression, the nuclear transition matrix element is $|M_{if}|^2 = |\langle 4_f |H_\beta|4_i\rangle |^2$, Eo is equal to the endpoint energy and E is the energy of the electron of momentum p. Finally F(z,p) is the Fermi function that corrects the momentum distribution for the effect of extranuclear electrons on the emitted electron. S_n is a shape factor (Kotani and Ross (1959)) which will be discussed later.

The most probable beta decay process is one in which the emitted electron carries away no orbital angular momentum. Since the electron and neutrino each have spin 1/2, such a process can only occur between states of the same parity whose spins differ by a maximum of 1 unit. The selection rule for allowed beta decay is then $\Delta\pi$ = No and $\Delta J = \pm 1, 0$. The allowed transitions can be further divided into the Fermi transitions in which the electron and neutrino spins are oppositely directed so that

$$\Delta\pi = \text{No} \qquad \Delta J = 0$$

and the Gamow-Teller transitions in which the electron and neutrino spins are parallel and

$$\Delta\pi = \text{No} \qquad \Delta J = \pm 1, 0 \qquad \text{no } 0 \rightarrow 0$$

If there are no states available for which the allowed beta process can occur, then the much less probable

TABLE 1.2

Beta Decay Selection Rules

Type	ΔJ	$\Delta \pi$
Allowed		
-super	0	No
-unhindered	0,1	No
-hindered	0,1	No
First Forbidden		
-non unique	0,1	Yes
-unique	2	Yes
Second Forbidden	2,3	No
Third Forbidden	3,4	Yes

transitions in which the electron carries away one unit of angular momentum, will become detectable. The selection rule for these so-called first forbidden decays is

$$\Delta\pi = \text{Yes} \quad \Delta J = \pm 2,\ \pm 1, 0$$

If no final states exist to which allowed or first forbidden transitions may proceed, beta processes of still higher forbiddenness can occur associated with

$$\Delta J = 2, 3, 4, \ldots$$

These comments are summarized in Table 1.2.

For allowed beta decays, the shape factor S_o is independent of energy. For first forbidden transitions, S_1 is a complex function of energy but the energy dependence is so weak that, in most cases, it can be treated as a constant. Generally S_n for $n = 2,3,\ldots$ is strongly energy dependent.

The total probability for beta decay, λ, may be obtained by integrating equation 1.2 over all possible values of the momentum. The result is,

$$\lambda = c|M_{if}|^2 f_n (Z, E_o)$$

where $f_n (Z, E_o)$ is a tabulated function of Z and E and $|M_{if}|^2$ is the matrix element for the transition. Frequently, this equation is written in terms of the half life $T_{1/2} = \frac{\ell n 2}{\lambda}$.

In this nomenclature, the product $f_n T_{1/2}$ is called the comparative half life. It is inversely proportional to the square of the nuclear matrix elements.

Figure 1.5 presents a histogram (adapted from Gove (1969)) of the distribution of $f_o T_{1/2}$ values for beta decaying nuclei in the mass range 80 to 100 of concern in this work. Since S_n is not uniquely defined for most forbidden decays, it is customary to set it equal to unity and describe forbidden transitions by values of $f_o T_{1/2}$. The allowed beta transitions in this mass range have log $f_o T_{1/2}$ values ranging from 4 to 7 while first forbidden decays range from 7 to 10. The subgroup with $\Delta\pi$ = yes and $\Delta J = 2$, the so called first forbidden unique cases, have a much smaller scatter in log $f_o T_{1/2}$ values.

Measured values of log $f_o T_{1/2}$ can be used as a indicator of the difference in spin and parity between the two nuclear states connected by beta transitions. Unfortunately, because of the large spread in log $f_o T_{1/2}$ values, it is only a guide.

1.9 Electromagnetic Interaction

Upon completion of nucleon emission or beta decay, the final nucleus can be left in an excited configuration which may proceed to a stable ground state via the emission of electromagnetic radiation. This occurs during the re-

Figure 1.5 Frequency histogram for log fT values

arrangement of one or more nucleons whose charges and magnetic moments also become disturbed. This in turn causes perturbations to the electromagnetic field which results in the radiation of quanta into the nuclear space surrounding the nucleus. The energy associated with this radiation is roughly the energy difference of the two nuclear configurations.

It is convenient to classify the emitted radiation in terms of a multi-pole order, λ, with the quantum of energy involved carrying away λ units of angular momentum. This angular momentum is related to the spin change between the initial and final nuclear states of the transition through the relation

$$|J_i - J_f| \leq \lambda \leq J_i + J_f$$

It is to be noted that transitions for which $J_i = J_f = 0$ are forbidden since no transitions with $\lambda = 0$ occur.

The electromagnetic operators can be classified as electric or magnetic. The electric operators (Eλ) couple states of opposite parity when λ is odd and even parity when λ is even. On the other hand, the magnetic operators (Mλ) couple states of like parity for λ odd and unlike parity for λ even. Since electric and magnetic transitions of the same multipole order differ greatly in transition probabilities, it is possible to experimentally distinguish between them. The selection rules are summarized in table 1.3

(Moszkowski (1968)) which presents the restrictions on ΔJ and $\Delta\pi$ for both types of radiation as well as the transition probabilities expected on the basis of a very naive single particle model (Weisskopf (1951)). These rate estimates are useful as a guide and actual probabilities are often expressed in terms of these single particle estimates (T_{sp}) called Weisskopf units.

In a similar manner to that of beta decay, the transition probability for emission of a photon of energy $h\omega$, connecting the initial (i) and the final (f) states of the nucleus can be expressed as

$$T\ (\sigma,\lambda) \propto \frac{(\lambda + 1)}{\lambda[(2\lambda+1)!!]^2} \left(\frac{\omega}{c}\right)^{2\lambda+1} |O_{if}^{\sigma\lambda}|^2$$

where $(\sigma\lambda)$, the multipolarity, refers to either $M\lambda$ **or** $E\lambda$ transitions and where $|O_{if}^{\sigma\lambda}|^2$ is the transition matrix element involved between states i and f (Enge (1966)). An examination of table 1.3 reveals that as λ increases the transition probability decreases by many orders of magnitude. This rapid decrease, predicted by the Weisskopf model, is in general agreement with experimental observations. However, a notable exception to this trend seems to occur for M1 and E2 transitions. Here, collective effects apparently enhance the E2 rate so much so that it competes with the M1 rate

TABLE 1.3

Gamma Decay Selection Rules and Weisskopf Estimates

Type	Multipolarity ($\sigma\lambda$)	ΔJ	$\Delta\pi$	T_{sp} (in sec^{-1} and E_λ in MeV)
Electric dipole	E1	≤ 1	yes	$1.0 \times 10^{14}\ A^{2/3}\ E_\lambda{}^3 S$
Magnetic dipole	M1	≤ 1	no	$2.9 \times 10^{13}\ E_\lambda{}^3 S$
Electric quadrupole	E2	≤ 2	no	$7.4 \times 10^{7}\ A^{4/3}\ E_\lambda{}^5 S$
Magnetic quadrupole	M2	≤ 2	yes	$8.4 \times 10^{7}\ A^{2/3}\ E_\lambda{}^5 S$
Electric octupole	E3	≤ 3	yes	$3.4 \times 10^{1}\ A^{2}\ E_\lambda{}^7 S$
Magnetic octupole	M3	≤ 3	no	$8.7 \times 10^{1}\ A^{4/3}\ E_\lambda{}^7 S$
Electric 16-pole	E4	≤ 4	no	$1.1 \times 10^{-5}\ A^{8/3}\ E_\lambda{}^9 S$
Magnetic 16-pole	M4	≤ 4	yes	$4.8 \times 10^{-5}\ A^{2}\ E_\lambda{}^9 S$

in cases where the selection rules permit. For these occurrences, the radiation is found to be mixed multipole in character. Experimentally it is found that almost all other transitions are of a pure multipole nature.

1.10 Internal Conversion

A mode of decay which always competes with gamma emission is internal conversion. In this process, the energy released in the nuclear rearrangement is transferred directly to an atomic electron, which is then ejected from the atom. The energy of this electron is equal to that of the transition less the binding energy of the electron shell from which the electron originated. For any given gamma transition several discrete conversion lines will appear. Each corresponds to the internal conversion of electrons from the K, L_1, L_2, L_3, etc. shells. Since the electrons closest to the nucleus have the greatest probability of interacting with it, the K lines are more intense than the L lines, the L lines more than the M lines, and so on.

The competition between internal conversion and gamma ray emission in any given transition is measured by the conversion coefficient defined as

$$\alpha = \frac{Ne}{N_\gamma}$$

where N_e is the number of electrons and N_γ is the number of photons emitted in the transformation per unit time. This coefficient can be further subdivided into quantities depending on the atomic shell from which the electrons are ejected, that is α_k, α_L, etc. These coefficients can yield information regarding the multipolarity of the transition involved and hence the J^π of the nuclear states taking part in the decay.

1.11 Extranuclear Deexcitation

With the loss of an electron in the atomic shells, a vacancy exists which is promptly filled by electrons from the higher order levels; that is, the atom, now in an excited state, attempts to reestablish its ground state through one of two competing processes: Fluorescence is the emission of electromagnetic radiation whose energy corresponds to that of the x-ray region of the spectrum. (Thus, this process is accompanied by the emission of x-rays characteristic of the daughter nuclide). The auger effect is the de-excitation of an atom by electron emission. Here, the orbital electron, excited by a fluorescent photon (x-ray) via an internal photoelectric effect, is termed the auger electron. Its energy of ejection from the atom is simply the difference between the energy of the photon and the binding energy of the electron. In a similar manner to internal conversion, the auger coefficient is defined as the ratio of the number of auger electrons to the number of fluorescent photons (Chase and Rabinowitz (1967)).

CHAPTER 2

Data Acquisition

Introduction

This chapter will delineate the methods and technique used to acquire data on the decay of the krypton 89 nucleus. The first section concerns sample preparation, describing both the irradiation facility and gas transport system with emphasis placed on the method of isolating krypton from the other fission products. The source material, after encapsulation in a leak-proof container, was sent to the Nuclear Research building (which adjoins the reactor) via a pneumatic "rabbit" tube system. The krypton sources were suitably positioned next to the various detectors used. The electronics used to analyze the pulses from these detectors are discussed in the final portion of the chapter.

A. Sample Preparation

The fission process produces a spectrum of light and heavy fission fragments. The lighter mass peak includes krypton nuclei with masses ranging from 85 to 95 as previously illustrated in Table 1.1. This complex mixture of krypton activities can be extracted from the general mass of fission products by means of gas sweeping and chromatography. By proper adjustment of the production, delay, and counting periods, it is possible to concentrate more than 80% of the total krypton activity of the sample in one radio-active species. However, the problem of growth of daughter activities into the initially pure krypton sample is not so readily solved as that of fission fragment separation.

2.1 Irradiation Facility

The irradiation apparatus was developed in 1962 at the McMaster reactor by Okenden and Tomlinson. The facility consists of a fission chamber or an irradiation cell mounted on the end of a twelve foot probe which is inserted into one of the reactor beam ports as shown in figure 2.1. The beam port itself is an aluminum tube extending up to the reactor core. The use of a foot long plug of bismuth positioned between the reactor core and the end of the beam tube serves to attenuate the gamma rays from the core. To minimuze neutron streaming into the beam port floor area the probe is filled with absorbing material in the configuration illustrated by figure 2.2. The flux at the fission chamber head is about 5 x 10^{10} n/cm^2/sec.

The internal construction of the irradiation cell is illustrated in figure 2.2. The chamber used in this investigation was fired with 0.5 grams of U233 deposited

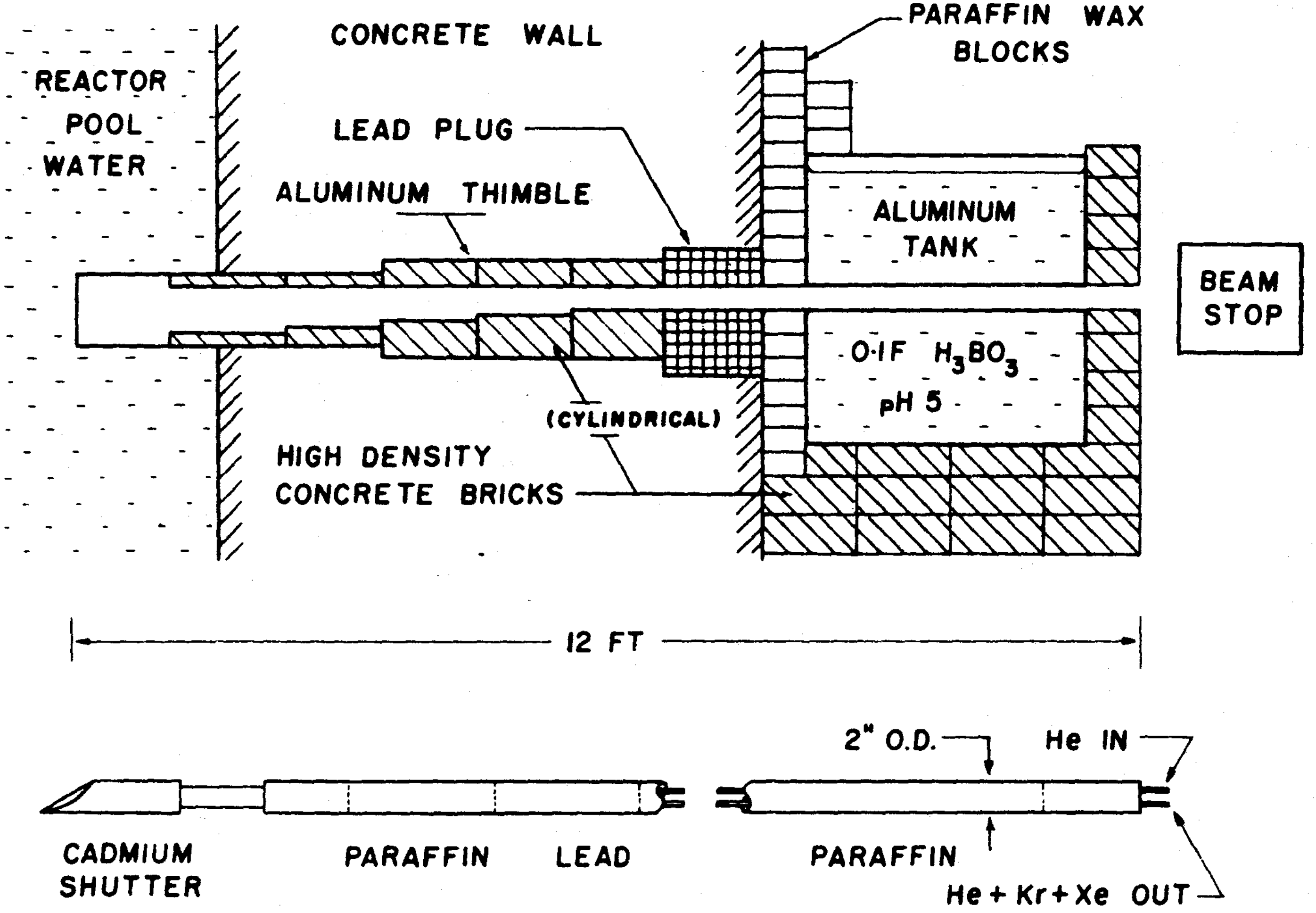

Figure 2.1 Cross section of reactor beam port and gas sweeping through-tube

on hydrous zirconium plates via a technique due to Fiedler (1966). Hydrous zirconium oxide was used as the emanating substance because of its good emanating efficiency, high resistance to radiation damage, and its ability to retain emanating power in the dry helium atmosphere of the gas sweeping apparatus (Archer 1965)). Uranium 233 was selected for its high thermal fission yield of ^{89}Kr relative to the higher mass krypton isotopes.

The irradiation chamber was surrounded by a cadmium sheath with a hinged, gravity-operated shutter on the front end. Normally closed, this shutter was opened by remotely retracting the sheath which in turn lifted the shutter over the rounded head of the chamber. The shutter was closed by gravity when the reverse process of advancing the sheath forward occurred. This arrangement permitted irradiation of the uranium for variable lengths of time with a practical minimum of about two seconds.

2.2 Gas Sweeping System

The gas sweeping apparatus involves two main components: one is the gas transport system and the other is the gas chromatograph column described next. Following irradiation, the noble gas fission products, xenon and krypton, were rapidly emanated from the fissile material, while the highly reactive halogen fragments, bromine and iodine, remained embedded in the adjacent substances.

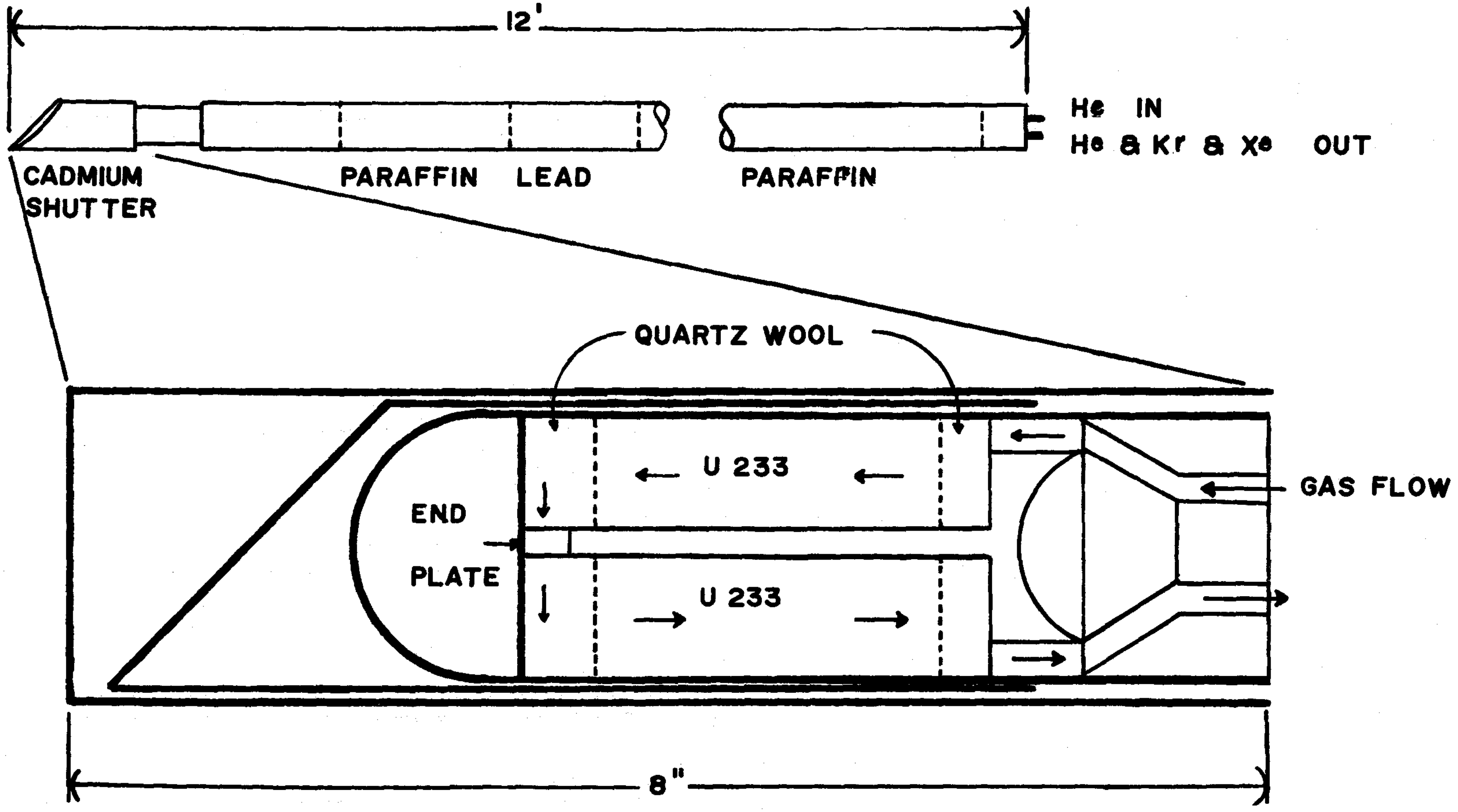

Figure 2.2 Cross section of fission chamber section of through-tube

Thus, once these gaseous products have been removed from the cell via the transport system, only a simple separation of xenon and krypton is required before use can be made of the sample. This was accomplished by chromatographic techniques.

Gas chromatography, using activated charcoal as the extraction agent was first applied by Koch and Grandy (1960). They utilized charcoal at room temperature to effect a separation in 10 to 20 minutes. Okenden and Tomlinson (1962) improved this to 10 to 15 seconds by using powdered charcoal on the surface of glass wool at room temperature. For this work, the extraction of the krypton from the xenon was accomplished immediately by the use of pyrex glass wool held at liquid nitrogen temperatures. This method was developed by Archer (1966). He found that this chromatograph mechanism involved a condensation-evaporation process in which the probability of evaporation of a molecule, following condensation, was an exponential function of time, with reactivity and weight as parameters. For the inert gases, at a given temperature, the capture time was mainly dependent upon the atomic weight, being the longest for radon, followed by xenon, krypton, argon, neon, and helium, in that order. At liquid nitrogen temperatures the adhering time of the heavier xenon isotopes was essentially infinite while that for helium and krypton was near zero.

It is to be noted that this mechanism becomes blocked by any mono-molecular layer of gas present on the glass wool. Thus, the column had to be frequently rejuvenated if its effectiveness is to be maintained. In the case at hand, the column must be placed in a oven at 70°C for several days before each series of experiments. When operating properly, the separation efficiency of the column is very high with less than 0.01% of the xenon fraction remaining in the krypton.

The transport of radioactive fission product gases was accomplished via a helium carrier gas. The flow path through the vinyl and glass tubing was controlled by a set of solenoid valves, in a configuration shown by figure 2.3. Various combinations of valves were opened or closed by electrical relays, each of which was employed to achieve a specific function. Upon completion of each source preparation, the used helium and any remaining radioactive materials were exhausted through a series of traps which cleaned, dried, and decontaminated the residue. The final vapours were monitored for activity and then vented to atmosphere via the reactor building exhaust ducts. These last traps were replaced or renewed daily.

2.3 Krypton Source Production

Selection of a particular fission fragment was accomplished by varying the irradiation and decay periods.

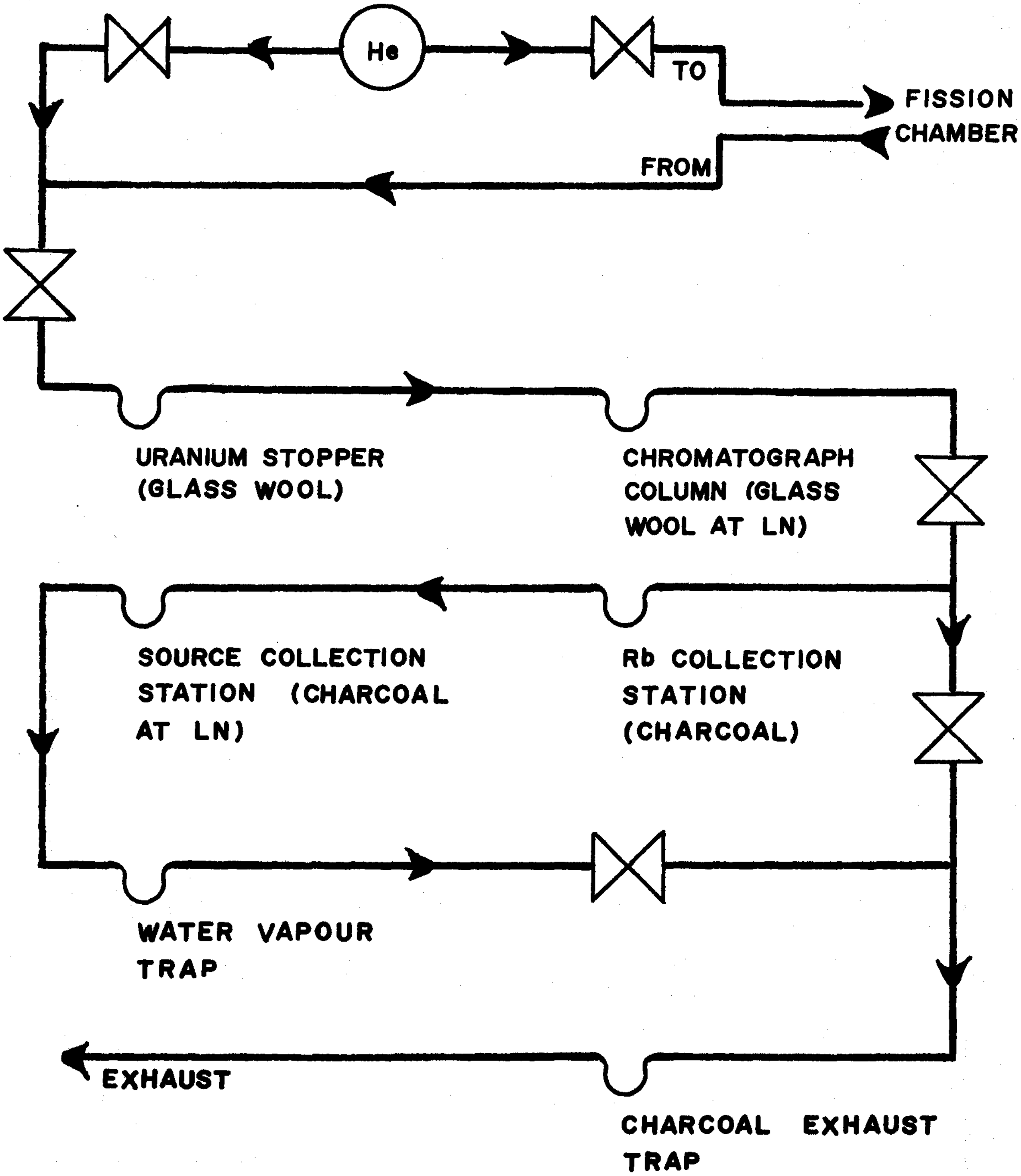

Figure 2.3 Gas sweeping apparatus external to the reactor beam port

Once these had been determined, source strength was chosen by adjusting the distance between the irradiation cell and reactor core. The length of irradiation (that is, the time that the cadmium shutter was open) also affected source intensity; however, this period had to be correlated with the waiting period in such a way as to optimize the specific krypton activity under study. For the production of the 89 isotope, a two minute irradiation time, coupled with a 2.5 minute holding time (during which the shutter remained closed and the carrier gas was at rest) was employed. The short irradiation period kept the ^{88}Kr(2.8 hours) and ^{87}Kr (75 minutes) production low. The long "hold up" time effectively removed all of the 8 second ^{91}Kr and much of the 32 second ^{90}Kr activity. When the hold up time was complete, the contents of the fission chamber were flushed out of the cell, through a uranium trap, into the gas chromatograph, and thence into a pyrex glass U-tube filled with activated charcoal at liquid nitrogen temperatures. (The uranium trap contained glass wool at room temperature and prevented uranium from the irradiation unit escaping from the system.) The total time required for completing the transfer of the radioactive materials from the irradiation cell to the U-tube was 30 seconds. To monitor the transfer process and to provide a guide as to source strength, a Geiger-

Muller survey meter was used to record the activity passing along the transfer line. As soon as the burst of activity had passed, the valves were closed to lock the sample in place. The sample trapped in this manner contained substantial contaminants in the form of the daughter rubiduim activities. Since rubidium at room temperature is a solid which adheres to activated charcoal, the U-tubes were immediately immersed in boiling water and helium carrier gas was "blown" into the tube to separate the krypton activities from its decay products. The freshly prepared krypton activities were carried by the stream to a final U-tube containing nitrogen-cooled, activated charcoal powder and trapped there. This "blow time" of about 15 seconds was determined by the interval required to collect all the activity into the small volume of the counting cell. Since rubiduim activity began to grow into the source again, the U-tube was quickly decoupled from the system and dispatched by "rabbit" from the reactor to the research laboratory. This decoupling and sealing system consisted of two 18 guage x 3 inch long stainless steel hypodermic needles inserted into the ends of the pyrex glass tube through rubber serum stoppers. These provided gas inlet and outlet to the source and upon removal the stoppers sealed the gaseous radioactive source within the tube. To ensure a good seal the U-tube was momentarily placed in boiling water before decoupling so as to allow the rubber to become pliable.

Upon arrival in the research building, the U-tube was removed from the rabbit and was ready to be counted by the analysis apparatus. The total time between termination of the blow time and the initiation of the count time was about 40 seconds. The length of time for which the events were recorded was six minutes for each sample of ^{89}Kr or slightly more than two half-lives; this counting time represented a reasonable compromise between poor statistics with pure samples and good statistics with serious contamination from rubiduim daughters.

The sequence of events involved in source production required 5.5 minutes and the cycle thus provided a good matching of source to counting time. The source production included a cell flushing period in which, after the source had been dispatched pure helium was swept through the irradiation chamber to remove all free fission products. As in the case of source residues, these spent fission products were also directly vented through the exhaust section of the apparatus. For the production of krypton 89 a "flush time" of one minute was employed. When the sample production system was not in use, the probe containing the irradiation cell was retracted six feet from its normal operating position near the core to remove it from the neutron flux.

B. Instrumentation

The disintegration of radioactive nuclei leads to information concerning decay schemes through a study of the resulting gamma ray emissions. Since these emissions are not directly observable, their presence must be determined by intermediate devices positioned between the event and the research worker. An integral part of this detection system is the detector whose primary purpose is to absorb energy from the radiation quanta and then produce an electrical signal proportional to this energy. (To the rest of the apparatus falls the task of amplifying, shaping and finally sorting the signals according to amplitude.) Since, in the current investigation only germanuim semiconductor crystals were used, discussions will be limited to this type of detector.

2.4 Germanium Semiconductor Detectors

In recent years, the germanium semiconductor detector has revolutionized the problem of determining gamma ray energies. The improvement of a factor of ~20 in resolution over the best NaI(Tl) detectors without a large loss in efficiency has made it possible to observe details in gamma ray spectra which could not be resolved by any other means.

Briefly the germanium detector operates as follows. When a quantum of radiation enters a detector, it indirectly produces a trail of electron-hole pairs resulting from interactions with the crystal valence electrons. These charges are made to drift to the electrodes by the application of an electric field, and thus create a charge pulse. The detector must consist of insulating material so that the electric field does not produce a prohibitively large leakage current with its consequent noise contribution. Also, the insulator must be of extremely high purity in order to prevent trapping of the e-h pairs. One method of achieving these conditions is to reverse bias a pure germanium n-p junction diode. This allows application of sufficiently high electric fields without excessive noise generation and minimizes recombination and trapping problems (Miller, Gibson, and Donovan (1962)). In this type of detector, with reverse bias, the holes accumulate near the negative electrode, while the electrons congregate close to the positive electrode. The internal volume is almost free of charge and is called the depletion region over which all of the potential drop is essentially confined. Thus, the high resistivity zone is the radiation sensitive portion of the detector.

For the study of gamma rays, a much larger active volume than can be obtained in the manner described above, is required. An extension of the depletion region can be accomplished by drifting a layer of lithium into a crystal of p-type germanium. The amount of drifted lithium adjusts itself in the p-regions adjacent to the intrinsic section so as to exactly compensate the acceptors present , thus transforming this zone into the high resistivity region required. A super diffusion occurs if a strong reverse bias is applied during heating since this allows the lithium atoms to penetrate further into the crystal (Ouseph and Schwartz (1970)). Diffusion profiles of modern detectors reveal that more than 90% of the volume of the germanium can be converted into the sensitive region by this process (Smith (1972)); (Campbell, Smith, and MacKenzie (1971)).

Ge(Li) detectors must be maintained at liquid nitrogen temperatures. Due to the inherent small band gap of 0.66 eV in germanium, excessive thermally generated leakage currents develop unless the detector is kept cooled. More important, the cooling must be maintained for the life of the device since the lithium drift is not stable at room temperatures.

Ge(Li) detectors are generally fabricated in either a planar or coaxial configuration. Planar detectors consist of an intrinsic zone positioned between a parallel p-type and an n-type region. As a result of this construction, the field gradients are constant, leading to uniform collection times which provide good timing characteristics. But this advantage is offset by the fact that they cannot be made with large volumes and thus have rather poor detection efficiencies. The larger detectors required for high energy gamma ray spectroscopy are usually coaxial in form and may have active volumes of more than 70 cc. These detectors consist of a central p-type zone surrounded by a coaxial section of intrinsic material and then an outer annulus of n-type lithium diffused material. Because of this geometrical configuration, a constant surface leakage current is maintained with increasing length and therefore increasing volume so that collection times remain uniform. However, in the Trapezoidal type detector, variations in charge collection, due to the closed end, give rise to time response characteristics which are undesirable for coincidence measurements (Ewan, Graham, and MacKenzie (1966)). Figure 2.4 depicts the three major types of Ge(Li) detectors currently used in this laboratory (Tavendale (1967)).

The resolution of a germanium (or any)

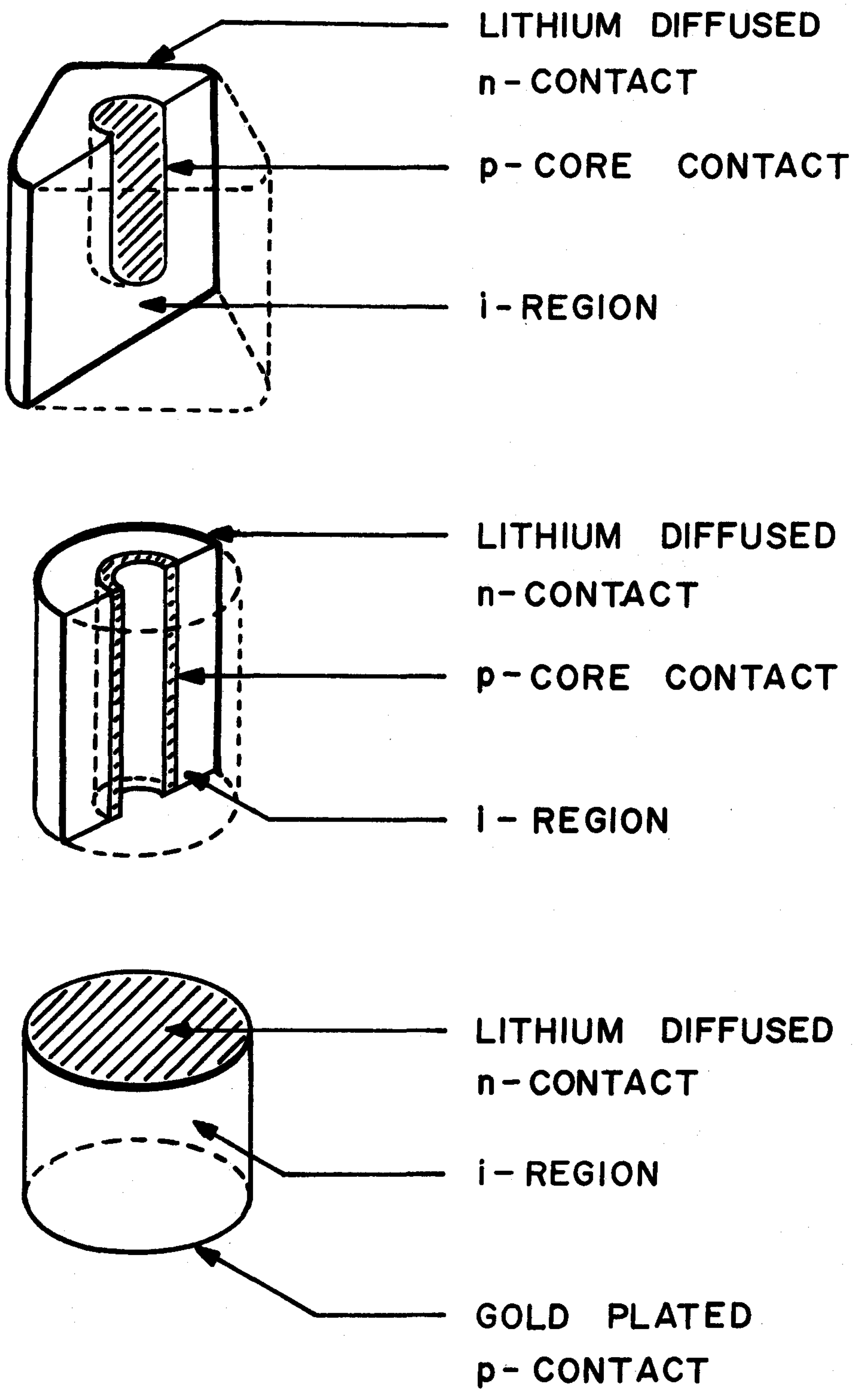

Figure 2.4 Configurations for lithium drifted p-i-n Germanium detectors:
(a) trapezoidal coaxial type
(b) true coaxial type
(c) Planar type

semiconductor device depends on noise generation in the crystal, preamplifier noise, and perhaps most fundamentally, statistics. This statistical limit is created by the numerical uncertainty involved in the process of turning the incident photon energy into free charge carriers. Since the process implies random effects, statistical broadening of a mono-energetic peak can be approximated by Poisson statistics where the full width at half maximum, Γ (a measure of resolution) is 2.354 σ (Bevington (1969)). Here σ^2 is the variance of the distribution and is defined to be $E\varepsilon$ with E as the energy of the incident radiation and ε as the formation energy of an e-h pair. (Strictly speaking, this is not a justified assumption as pointed out by Fano in 1947 with respect to gas counters. That is, multiple events that occur in the energy loss process are correlated and not independent as required by Poisson statistics. Hence

$$\Gamma = 2.354 \sqrt{E\varepsilon F}$$

where F is the Fano factor which is currently empirically estimated at 0.15 (Camp (1967)).) For germanium, $\varepsilon = 2.9$ eV/ ion pair whereas for NaI(Tl), $\varepsilon \sim 300$ eV/ion pair (Walter and Moore (Nov. 1968)). Thus, the limiting resolution of a NaI(Tl) detector may be expected to be $\sim\sqrt{100} = 10$ times worse than that of the Ge(Li) detector.

For this present investigation, a variety of Ge(Li) detection systems have been employed. Resolution specifications and peak-to-Compton figures are quoted for each type in table 2.1.

2.5 Detector Responses

The detection of radiation in matter is possible only through the process of ionization which is directly dependent on three main phenomena. The chief interactions which occur when quanta traverse matter are, the photoelectric effect, the Compton effect, and pair production (Davisson (1966)).

In the photoelectric effect, an incoming gamma ray strikes an atomic electron which is dislodged with an energy of the quantum less the appropriate shell binding energy for the electron. Since the photon is completely dissipated during this action, the energy loss subsequently suffered by the photoelectron in the detector represents the total incident radiation energy and creates the so-called photopeak in response. The probability of the process occurring falls off rapidly with increasing energy so that it is most prominent for gamma rays of energy less that 100 kev.

The Compton effect is the dominant process for

TABLE 2.1

Ge (Li) DETECTOR SPECIFICATIONS

Present Work Terminology	Active Volume	Window Type	Resolution (kev)	Peak-To-Compton Ratio
0.9 cm^3 Det.	1.01 cm^3	0.13 mm Be 150 Å Au	0.8 kev @ 150 kev	~20:1
12 cm^3 Det.	12.10 cm^3	0.5 mm Al	3.2 kev @ 1.33 Mev	14:1
50 cm^3 Det.	49.80 cm^3	0.5 mm Al 1.0 mm teflon	2.9 kev @ 1.33 Mev	20:1

medium energetic gamma photons (0.5-5.0 MeV). It involves a photon-electron interaction in which the photon is not completely absorbed. Thus, the ejected electron and the energy-degraded gamma ray are the resultant products. Because the energy of the electron depends on the angle at which the photon is scattered, the detector response to a monoenergetic gamma ray is a continuum of pulse sizes ranging from zero up to almost the amplitude of the photopeak pulse. The corresponding spectral shape is a "knee" which is commonly referred to as the Compton edge. The scattered photon is now reduced in energy and, unless it escapes to detector surroundings, undergoes other interactions within the crystal. This results in further energy transfer to the detector. Thus, as the active volume increases, the probability of multiple interactions also increases and the number of full energy deposits in the crystal grows at the expense of the Compton distribution. Ideally, an infinite photopeak-to-Compton ratio would be desirable. In fact, with large detectors, this ratio is quoted as a figure of merit for commercially available detection systems. Values of this ratio in excess of 30:1 (measured from the lines in ^{60}Co) are not uncommon.

When the incident photon energy becomes greater than $2m_oc^2$ or 1.022 MeV, pair production begins to compete with the other two processes. The relative probability of occurrence for the three interactions as a function of energy is shown in figure 2.5 for a typical Ge(Li) detector (Goulding (1964)). In pair production an electron-positron pair is created from a photon in the field of the nucleus as required by momentum considerations (Christy and Pytte (1965)). The effect proceeds roughly as Z^2 and increases rapidly with energy above the threshold of 1.022 MeV. The detector response for this process produces spectral peaks at energies of 511 and 1022 keV below the photopeak. The magnitude of these so-called single escape (SEP) and double escape (DEP) peaks depends on the detector size. For small volume detectors, these SEP and DEP are large compared to the full energy peak. For large detectors, they are much less pronounced but still cannot be ignored in analyzing a complex spectrum.

In all of the spectra of this study a peak is observed at 511 keV. This arises from annihilation radiation detected when positrons which are created from pair production in the surrounding material of the detector, annihilate.

2.6 Amplification

In all nuclear detection systems, amplification of detector produced pulses, is achieved via a two step process: preamplification with slight (if any) signal

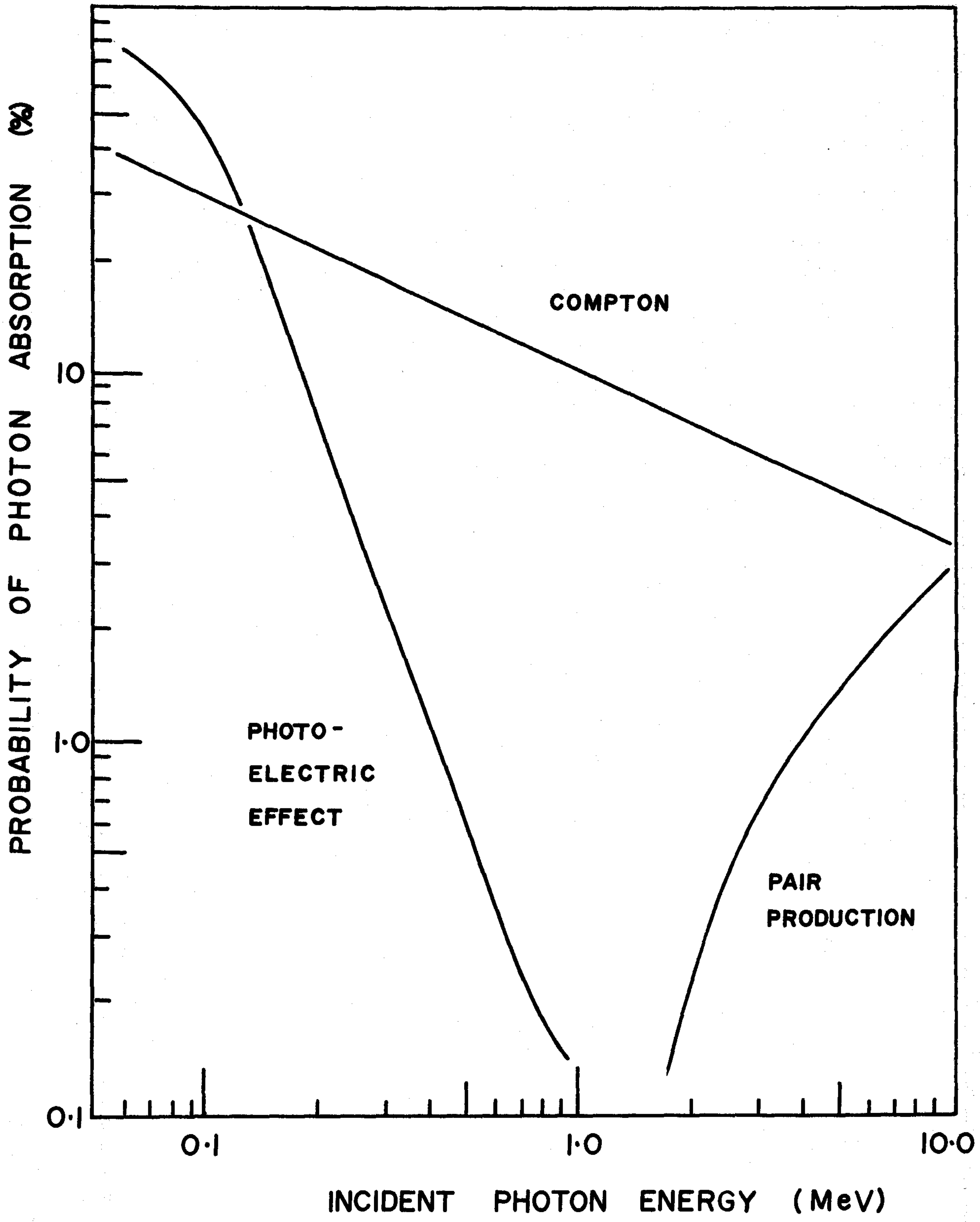

Figure 2.5 Probability of total absorption of γ-ray photons in a Ge(Li) detector 3 mm thick.

gain and linear amplification with pulse shaping.

The signal resulting from a gamma ray interaction in the detector is essentially a charge pulse proportional to the number of ion pairs produced in the intrinsic region of the detector. This signal is amplified via a charge sensitive preamplifier which produces, proportional to the input charge, an output voltage (~50-500 m Volts) acceptable to the main linear amplifier, the next in-line device. The output pulse has a fast rise time (~50 nsec) but falls exponentially with a time constant of about 10 microseconds. This is long enough so as not to interfere with pulse shaping in the main amplifier yet short enough to reduce pile-up effects (Blatt (1967)).

The noise in the preamplifier of modern Ge(Li) detectors is responsible for significant loses in resolution. The chief offender is the initial input stage, involving a field effect transistor. The noise in this FET can be reduced by cooling it along with the detector. For this reason, Ge(Li) detectors are rarely sold without a matching preamplifier as part of the detection package. There is also another intricate tie between the two units. The amount of noise generated by the FET is proportional to the capacitance to which it is connected and therefore directly proportional to the detector area. Thus, there is an important trade-off between detector size and preamplifier noise (Gibson, Miller and Donovan (1966)).

Pulse shaping in a linear amplifier serves two purposes: it maximizes the signal-to-noise ratio (Snr), and minimizes the system resolving time. As expected, these two aspects are so related that the optimization of the Snr is usually achieved at the expense of the resolving time and vice-versa. However, for spectral measurements, there is usually a narrow region of operation where a fairly good compromise exists.

In order to maximize the Snr, most main amplifiers employ two resistor-capacitor filters in tandem. The first is a CR high-pass filter which attenuates low frequency components of the input waveform. This is followed by an RC integrator having low-pass filtering characteristics where the rise time of the pulse or the high frequency component is slowed. However, the resultant signal usually possesses too long a duration time so that the probability of successive pulse overlap for high count rates is large. To reduce this pile-up effect, a second clipping or differentiation circuit is added as shown in figure 2.6(c). Thus, the pulse is shortened, but at the expense of the Snr (Malmstadt, Enke, and Toren (1963)). Consequently, selection of the appropriate time constants of the RC

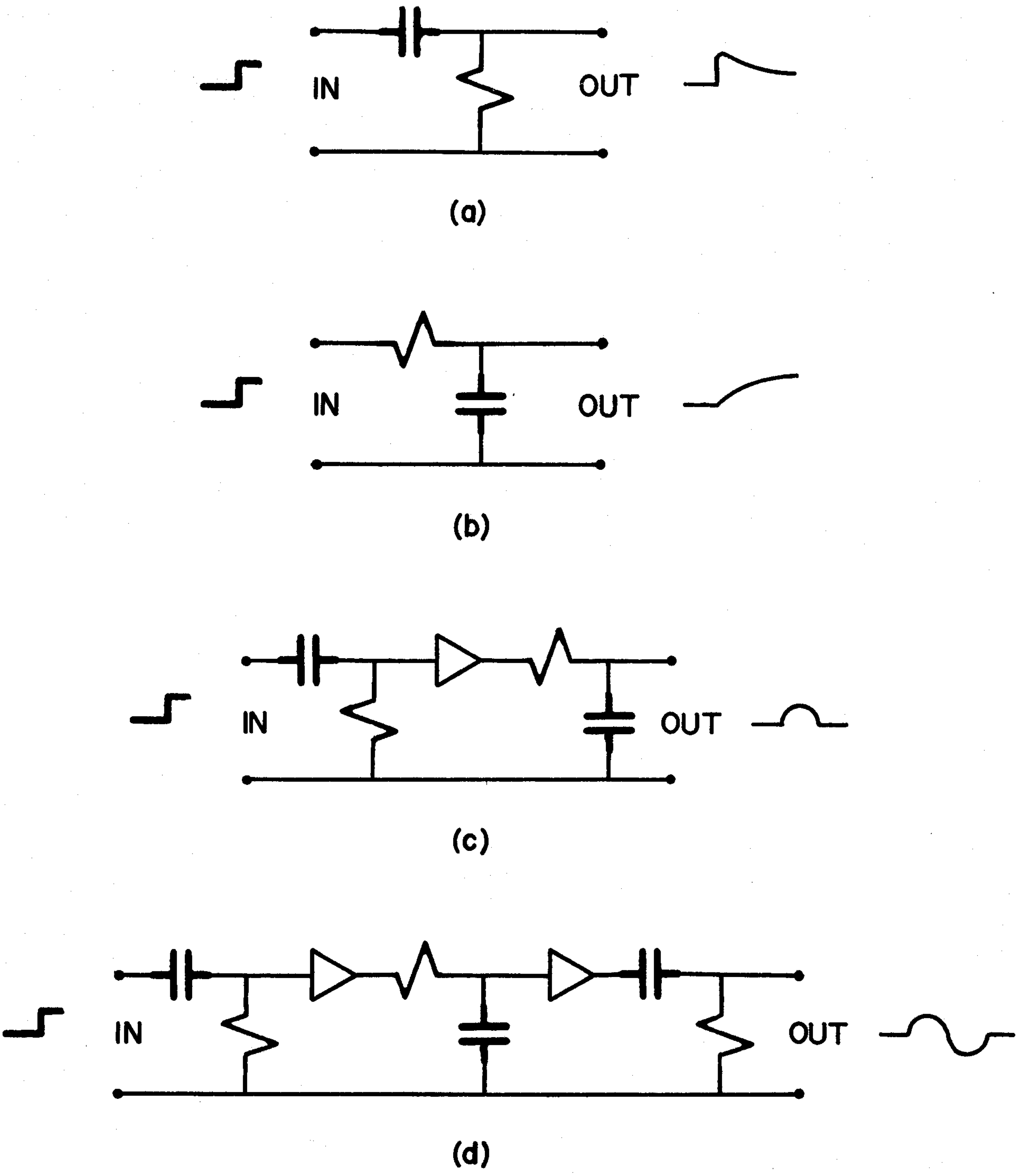

Figure 2.6 Resistor-Capacitor shaping methods:

(a) CR differentiation
(b) RC integration
(c) CR-RC pulse shaping
(d) doubly differentiated RC shaping.

filters to provide optimum performance must be made empirically for each experiment. Typical pulse shapes include a 1 μsec decay time and a maximum pulse height of 10 volts.

2.7 Multichannel Analysis

In order to obtain energy measurements from the detection system, the shaped pulses from the linear amplifier must be sorted according to height. This is the task of the multichannel analyzer.

The heart of the device is an analogue-to-digital converter (ADC) whose sole purpose is to convert the voltage pulse into a digital number. Present generation ADC's use Wilkinson type converters in which the pulse is allowed to charge a capacitor with a constant current leakage. Simultaneously, a high frequency clock drives a register, called the advance channel scaler (ACS). The ACS records the number of pulses in the oscillator's digital pulse train the duration of which coincides with the discharge of the capacitor. Termination occurs when the charge reaches a predetermined level. Thus, the number in the scaler is a digital representation of the amplitude of the input pulse. For the duration of analysis time in the ADC, a converter busy (CB) signal is active. When addressing is complete the CB pulse is deactivated (Goulding (1966)).

The memory unit is another major component housing the magnetic core memory and its associated registers. On termination of the CB pulse, a memory busy signal (MB) appears. This allows the number in the advance channel scaler to be loaded into an address register of the memory. When this is done, the contents of the memory corresponding to this generated address are extracted from core and placed in a memory register. (Detailed operation of magnetic cores is contained in <u>Basic Electronics</u> prepared by the US bureau of Naval Personnel (Dover Publications, Inc. New York (1968)).) The register is incremented and its number is replaced in core at the original address. Upon completion of the storage cycle, the MB pulse is deactivated. The MB and CB indicators, when taken as a pair cause a linear gate to close. This linear gate is used to block the acceptance of an input pulse by the ADC (that is, it prevents entry of another signal during analysis and memory update times)(Chase 1962)).

To the above basic components it was found necessary to add a digital spectrum stabilizer due to severe system gain drifts for single parameter work (this will be discussed in more detail in the next section). These drifts cause shifts in the channel locations of any given peak in the spectrum. They can be caused by the detector, amplifier, ADC, or all three. Correction for gain problems is accomplished via a subtract scaler in the unit whose output is applied to the pulse train output from the ACS of the ADC. The detected error is obtained by monitoring the output from a precision pulse generator which reflects drift from all preceding system components. A typical device configuration for this work is shown in figure 2.7 of the next section.

In order to round out the description of multichannel pulse height anlaysis systems, remaining components will be briefly mentioned here. An oscilloscope display unit is used to provide visual monitoring of memory contents. For permanent and numerical results, the spectrum can be placed on magnetic tape for later computer decoding. This is accomplished through the buffer control unit which presents to the tape transport the memory contents for transcription.

C. Technique and Analysis

In order to construct a nuclear decay scheme, it is necessary to determine the energy, and intensity of each gamma ray, and, in addition, to establish any time correlations between them. Single parameter experiments were carried out to achieve the first aim. Timing experiments using a two channel coincidence spectrometer were performed for the second.

2.8 Single Parameter Experiments

A thin window planar detector of active volume, ~0.9 cm^3, was employed for low energy runs, and a large volume, ~50 cm^3, Ge(Li) detector was used for most of the high energy runs. Both experiments employed the electronics shown schematically in figure 2.7. The inclusion of the spectrum stabilizer removed gain shifts. These were troublesome with the rapidly decaying sources and the consequent changes in analyzer dead time typical of these experiments.

The analysis of most of the spectra obtained in these experiments were performed via a computer program, JAGSPOT, developed at the Chalk River Nuclear Laboratories (Williams and McPherson (1968)), and modified by members of this laboratory for use with the McMaster CDC 6400 computer. This program constructs a non-linear least-square fit of the data in a region containing up to six peaks, to an analytical function of the form

$$I(x) = \alpha + \beta x + \sum_{i=1}^{n} I_i \int_{-\infty}^{Z_i} e^{\varepsilon(y-Z_i)} e^{-\delta(x-y)^2} dy$$

$$(n \leq 6)$$

where α, β, δ, ε, I_i and Z_i are the parameters of the calculation. For a single peak ($n = 1$) the function describes a linear background ($\alpha+\beta x$) upon which is super-

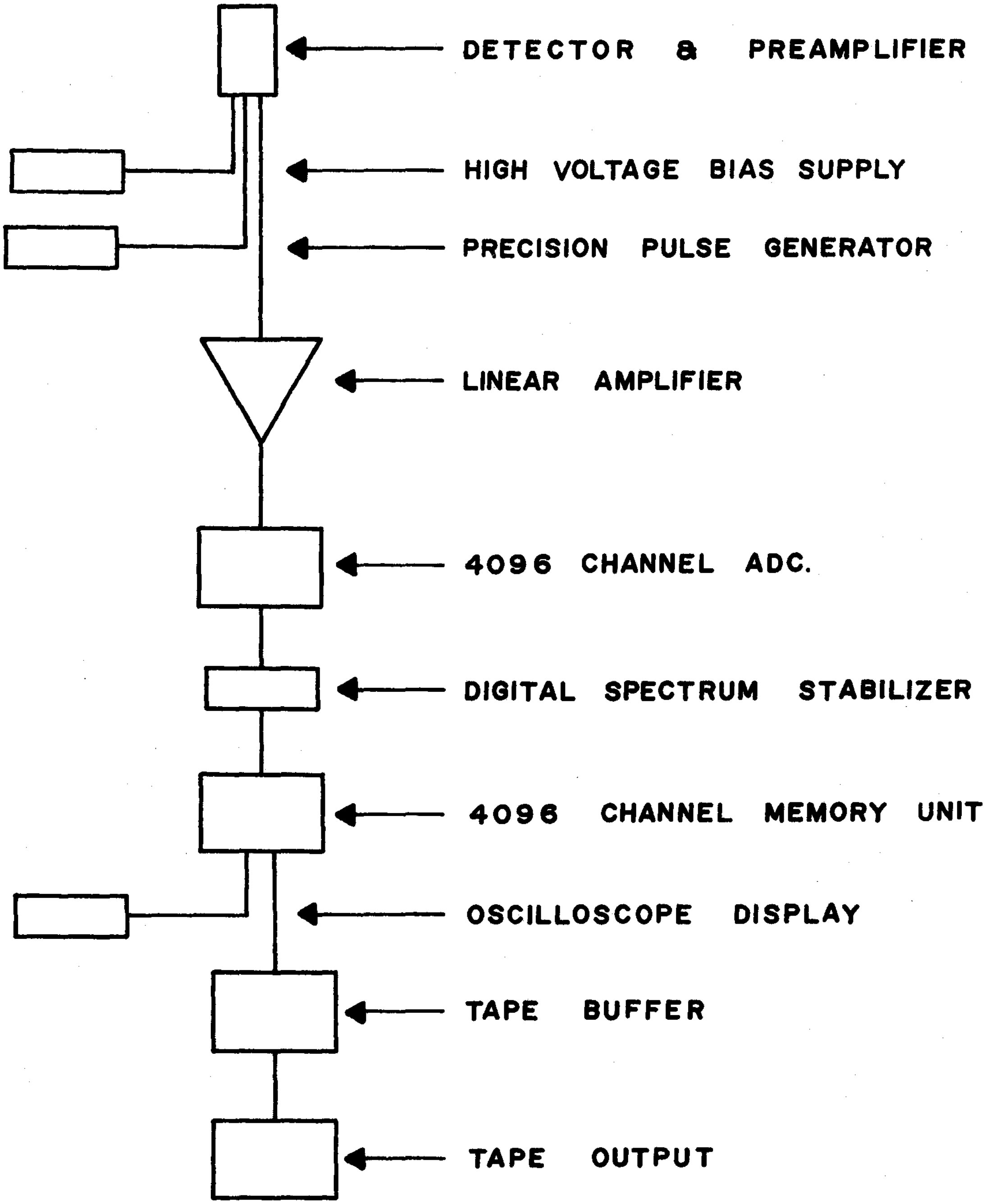

Figure 2.7 Schematic diagram of the electronic configuration associated with single parameter experiments.

posed a skewed gaussian shape. The character of this gaussian is determined by the integral which represents an error function (Hofstetter (1964)) of variance $1/2\,\delta$ with modulated amplitude $e^{\varepsilon(y-Z_i)}$. The number of counts at any channel, x, is found by summing the contributions from this family of gaussians formed as y runs from $-\infty$ to Z_1, where Z corresponds to a peak position based on a pure gaussian shape. The integrand, which is the envelope of this family, is a skewed peak, whose point of inflection on the high energy side is at Z_1. This above procedure is followed for regions with up to six peaks.

The calculation is initiated by starting with a zeroth approximation to each of the various parameters and then performing a least square calculation to obtain a first order estimate of each parameter. With these improved parameters, the process is repeated until the changes in the parameters of successive iterations is less than the error associated with each parameter. Since $1/\delta$ and $1/\varepsilon$ were found to be linear functions of energy (channel number), it was advantageous to determine these functions from the strong peaks in the spectrum. They could then be used to obtain appropriate values of $1/\varepsilon$ and $1/\delta$ for application to weak or unresolved peaks. The fitting procedure for such cases now involved only four parameters instead of six and thus made the analysis much more reliable. As a final result for the peak fitting section of the program, positions and areas of all fitted components were produced together with probable errors. These errors reflected the uncertainties due to parameters and statistics.

In most cases, the spectral peak generating portion of JAGSPOT provided comparable results to a Dupont 310 curve Resolver used in the low energy and very high energy "singles" runs. This device is a modified analog computer consisting of five series function generators each capable of producing a single distribution function on a cathode ray tube. Any given number of these functions can be positioned, shaped, and summed, until a trace is obtained which matches the experimental curve envelope. For the low energy run, a basic gaussian shape was employed requiring no assymetrical additions. However, for the high energy spectrum. a slight low energy skew was added to the curve to match the shape of strong singlet peaks in this energy range. The capability of producing non-linear background features also proved extremely useful when applied to these photopeaks located on compton edges. When the synthesized curve was manipulated into a form identical to the experimental data, individual components and their relative areas were determined by displaying each individual peak on its respective generator and recording the area from an integrator meter normalized to 100% for each envelope of multiple peaks. Numerical areas of these peak systems were later obtained by summing appropriate regions by hand.

In areas where more than six unresolved peaks were found in one conglomerate, the curve resolver was used exclusively. Also in regions where the background could not be approximated by a linear fit, which is the sole option in JAGSPOT, the curve resolver provided more realistic results. In these cases, the peak intensities so derived were found to be more accurate than the JAGSPOT determinations.

The energies of the unknown gamma rays from the nucleus under investigation were obtained by the "mixed source technique" in which the unknown spectrum was collected along with gamma rays whose energies were well known. Positions of all the prominent peaks were determined using JAGSPOT. Upon supplying the appropriate standard energies, the program was designed to construct a calibration curve of energy versus peak position. In fact, a cubic was generally found to be sufficient to reproduce the non-linearity of the ND161 ADC and a quadratic was adequate for the ND3300 analyzing system. The program then computed the energies of prominent unknown peaks together with probable errors. These values were then applied as internal standards to the ^{89}Kr singles spectrum which had been recorded under the same conditions as the energy calibration runs. In this manner, the energies of the remaining and weaker gamma rays were determined.

Above 3.2 MeV, where standard gamma energies are rare, energy calibration was obtained by using the contamination lines of ^{90}Rb as internal standards. Mason and Johns (1970) and Talbert, et. al. (1969) have made careful study of the decay of ^{90}Kr. They obtained their energy calibration above 3 MeV, from a comparison of the double escape peaks of high energy gamma rays with the full energy peaks of the calibration lines; that is, the separation between a full energy and double escape peak is always 1.022 MeV. Since Mason was using small Ge(Li) detectors, the double escape peaks in his spectra were much more prominent than those in the present work. The agreement in energy between Mason's and Talberts' work is excellent.

The relative intensities of the various gamma rays were determined using the relationship between source line intensity and the area of the full energy peak:

$$N_i = N_o \, (\varepsilon\omega)_i \, I_i$$

where N_o is the source strength, N_i is the area of the photopeak associated with the i th gamma ray, I_i is its relative intensity, and $(\varepsilon\omega)_i$ is the efficiency of the detector at the energy of the i th gamma ray. Since the source strength , N_o, was unknown in these experiments,

TABLE 2.2

Sources Employed for Efficiency Determinations

Detector (by volume)	Geometry	Vienna Sources	NaI Sources	Relative Sources
0.9 cc	singles	Co57	Ir192	
		Hg203	Tb160	
		Na22	Eu152	
		Cs137	Ta182	
		y88		
		Mn54		
50 cc	singles	y88	Bi207	
		Co60	Cl38	Co56
12 cc	coincidence	Am241	Ir192	
		Hg203		
		Co57		
		Na22		
		Cs137		

Table 2.2 cont.

Detector (by volume)	Geometry	Vienna Sources	NaI Sources	Relative Sources
		Mn54		
		y88		
50 cc	coincidence	Na22	Eu152	Co56
		Cs137	Bi207	
		Mn54	Ir192	
		y88		
		Co60		

only relative gamma ray intensities could be extracted.

The variation of $(\varepsilon\omega)$ with energy was obtained by analyzing spectra from sources in which the intensities, I_i, were well known. These intensity measurements were made using, in this case, two reproducible geometries (coincidence and singles) each employing two detectors as described in detail in the next chapter. One set of measurements served as the intensity calibration for the singles experiments. The other allowed calculations on coincidence probabilities to be performed for the time correlation study. These efficiencies are reproduced in figures 2.8, 2.9, 2.10 and 2.11, while table 2.2 provides a listing of gamma sources used in the calibrations. Most of these curves were produced using a set of IAEA calibrated gamma samples in which the source strength for each had accurately been determined. To supplement these measurements uncalibrated sources were employed whose source strengths were obtained using a NaI(Tl) detector and the tabulated efficiencies and photofractions of Heath (1964). For extrapolation into the higher energy regions used in the 50 cc detector runs, a ^{56}Co source was used. Here a relative, separate curve was obtained and then overlapped on the main curve to obtain the composite curves shown in figures 2.9 and 2.11. Intensities for this source have been recently reported in a paper by Camp and Meredith (1971).

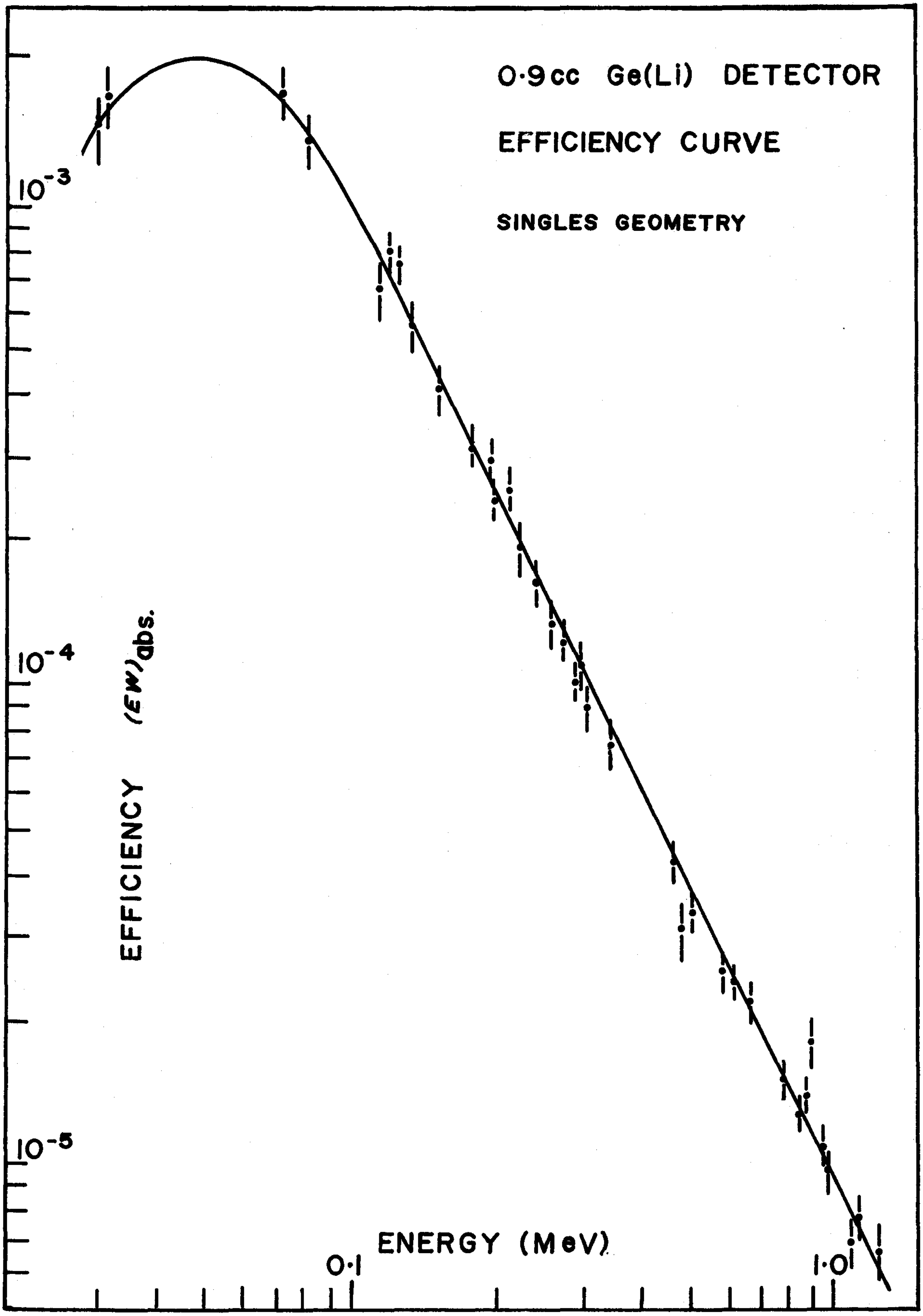

Figure 2.8 0.9 cc detector efficiency for singles geometry.

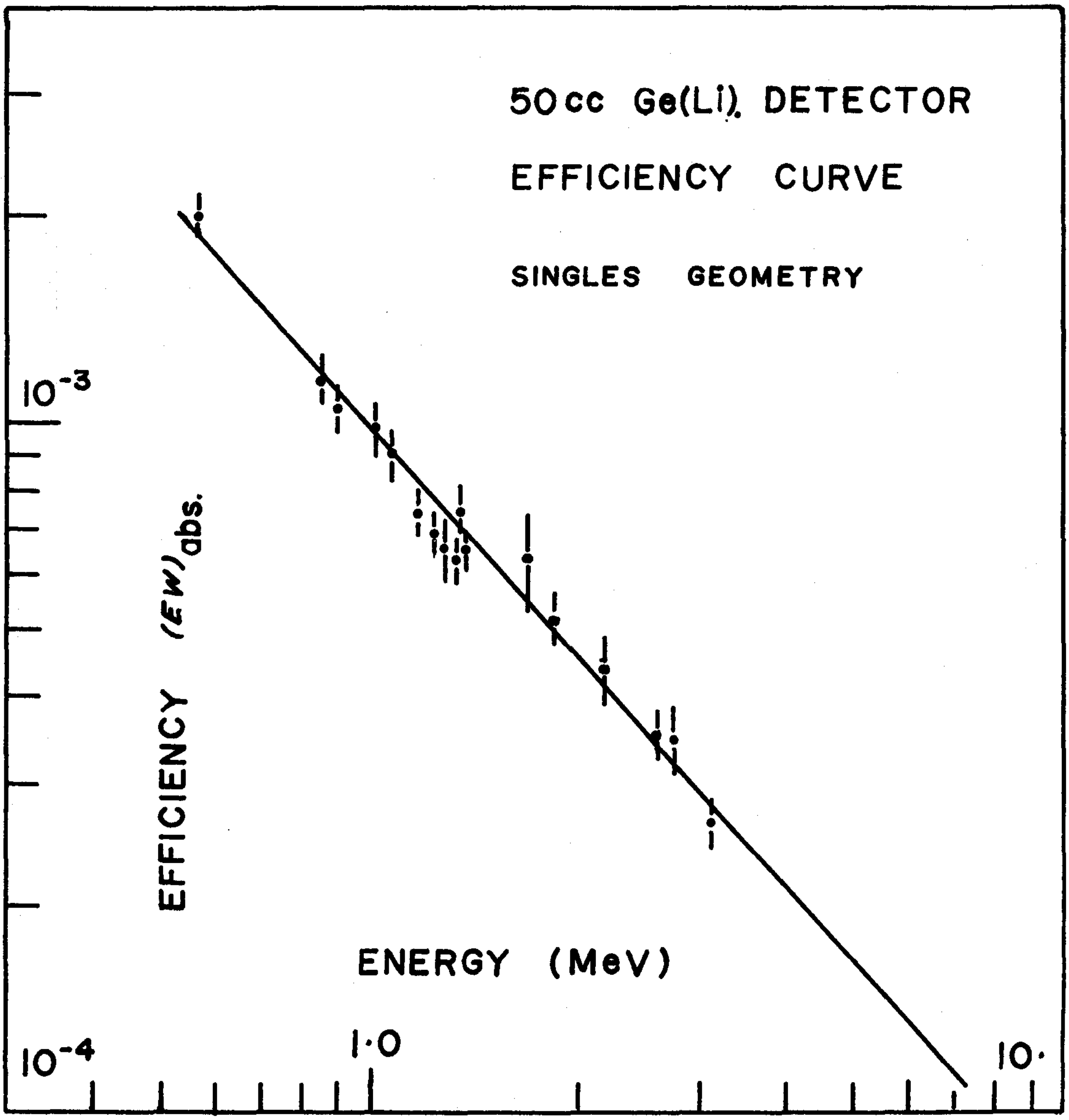

Figure 2.9 50 cc detector efficiency for singles geometry.

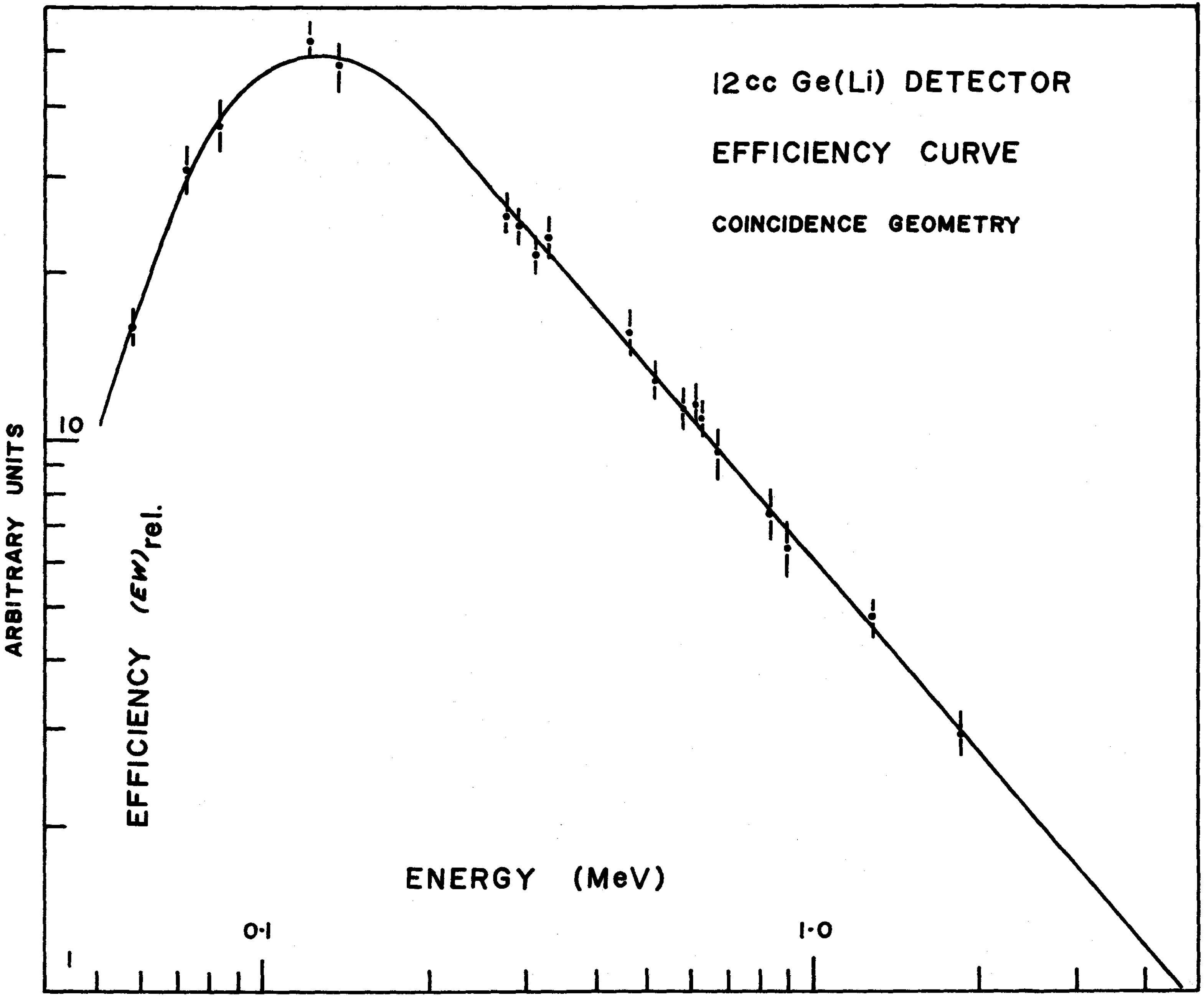

Figure 2.10 12 cc detector efficiency for coincidence geometry.

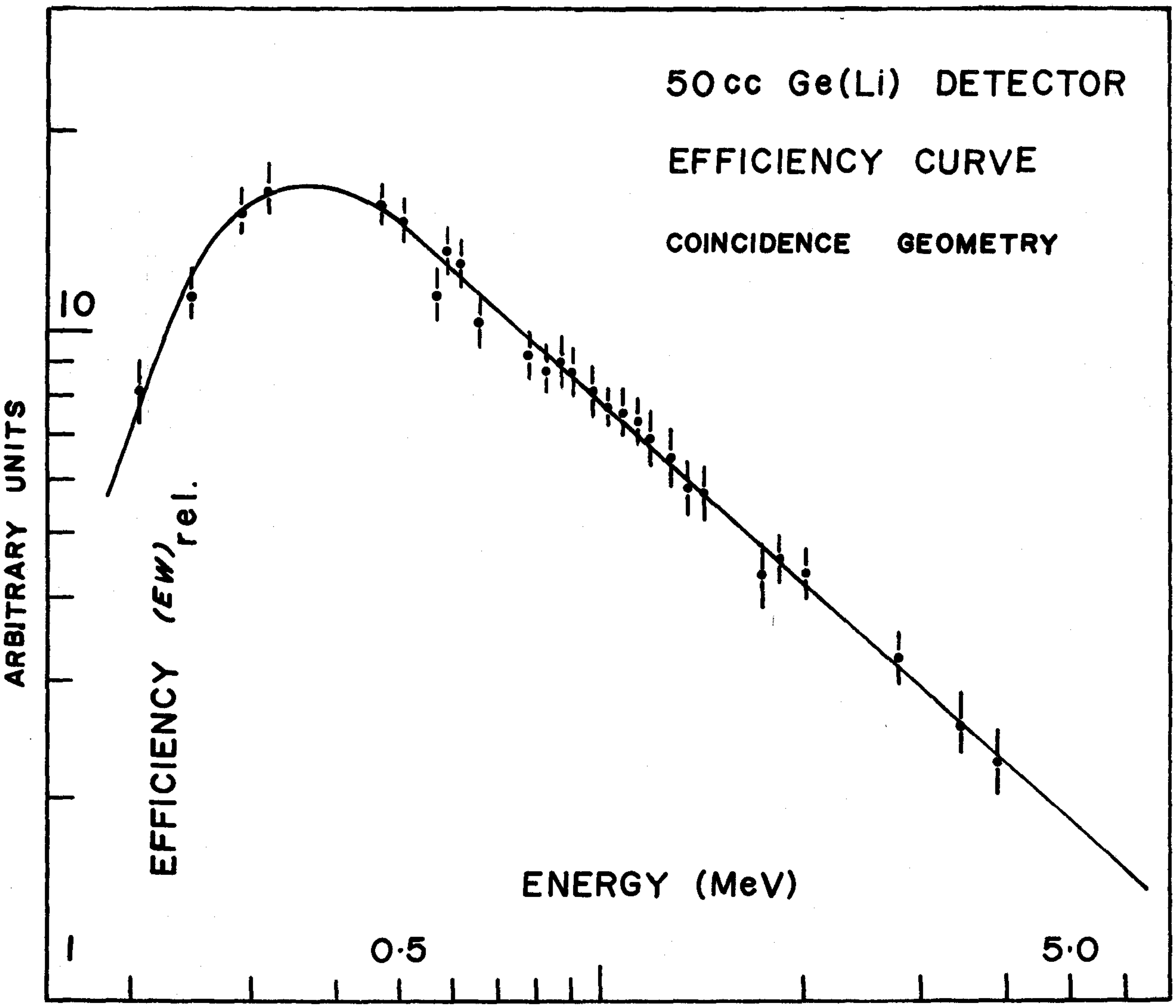

Figure 2.11 50 cc detector efficiency for coincidence geometry.

2.9 Two Parameter γ-γ Experiment

A gamma-gamma coincidence experiment was performed using a 12 cm^3 trapezoidal Ge(Li) detector and a 50 cm^3 true coaxial Ge(Li) detector with the experimental arrangement shown in figure 2.12. The 12 cm^3 detector was allowed to detect only those gamma rays below 1 MeV in energy while the 50 cm^3 detector was sensitive to photons above 200 keV. In essence, the coincidence circuit selected pairs of events which occurred within the resolving time of the circuit (~60 nsec) and initiated an analysis of their respective pulse heights.

The heart of the timing apparatus was the time-to-amplitude converter or TAC which provided an output pulse whose amplitude was proportional to the time difference between the two input pulses, termed start and stop pulses. These signals were supplied by two special units developed for high resolution Ge(Li) timing applications. Their purpose was to supply fast timing markers that denoted the occurrence of a nuclear event with a minimum of "walk", (Walk is the variation in the timing mark created by different signal rise times characteristic of Ge(Li) detectors (Ewan, Graham, and MacKenzie (1966).) The first device, coupled to the 50 cm^3 detector, was an extraploated zero strobe (Canberra Industries Model 1426). This unit compensates

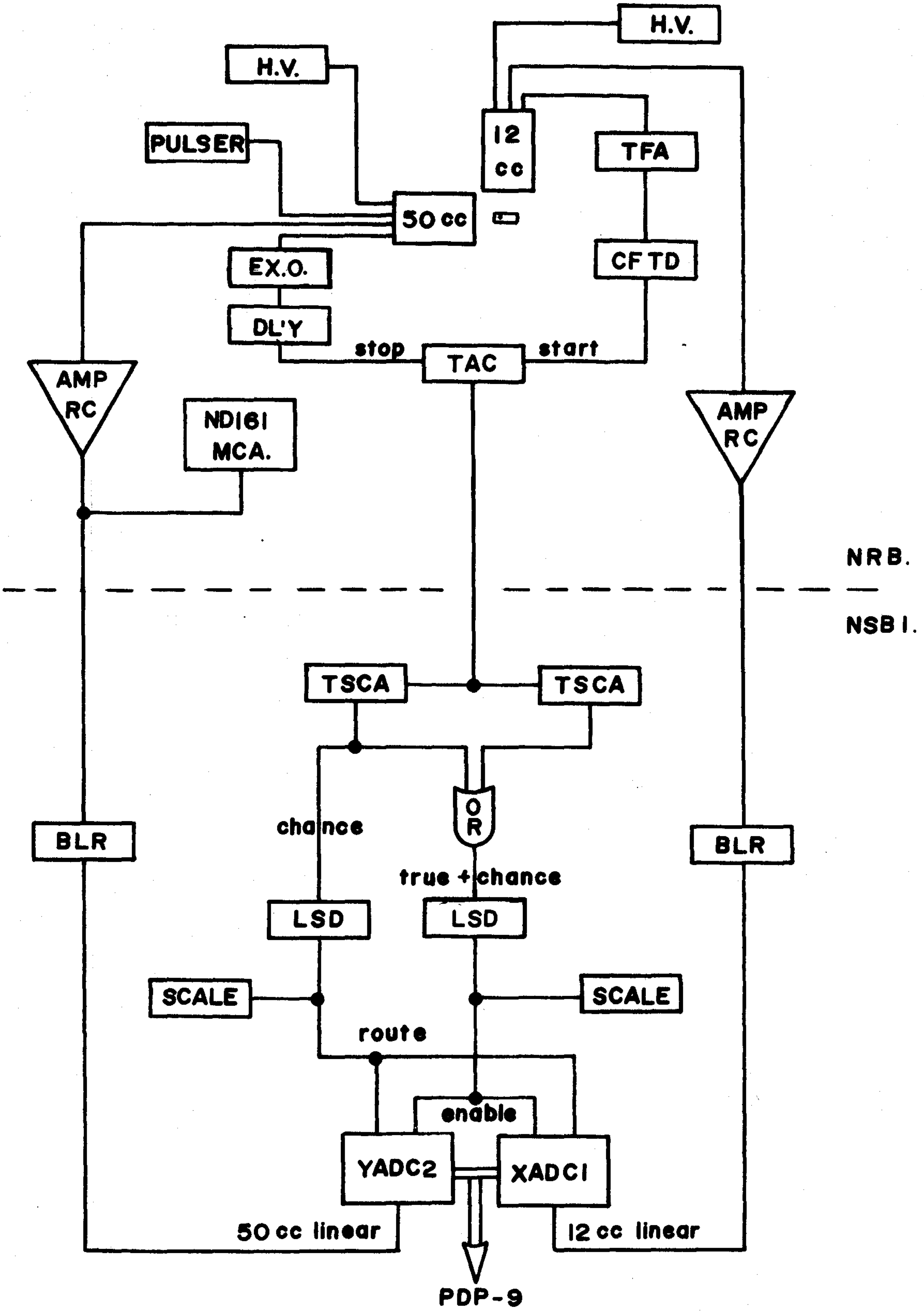

Figure 2.12 Electronic configuration associated with two-parameter coincidence experiment.

for timing walk by an amplitude compensation method. The second device is composed of two units: an Ortec Model 454 timing filter amplifier, TFA, and an Ortec 453 constant fraction timing discriminator, CFTD. As with the extrapolated zero strobe, the walk is again reduced, but this time by shaping the pulse into a bipolar configuration where the zero cross-over point is used as the generation time of the marker (Ortec (1970)). In order to equalize transit times of these modules to the TAC, a nanosecond delay unit was required following the extraploated zero device. For events which are associated with gamma cascades, through non-isomeric levels, the start-stop time difference is just that due to the different time delays of the circiutry associated with each detector. In this case, the 12 cm^3 detector arm served as the start pulse while the 50 cm^3 detector arm provided the stop pulse. Hence, all TAC output pulses from coincidence events have the same height. Superimposed upon this result is a uniformly time distributed spectrum due to chance coincidences. That is, the TAC output is also generated by unrelated events which occur randomly in each detector but which generate consecutive start and stop signals during the operating period of the converter. The output pulse height spectrum from the TAC as collected by a 512 channel (ND Model 121) multichannel analyzer is shown in figure 2.13. The rather broad unsymmetric peak can be attributed to the poor timing characteristics of trapezoidal Ge(Li) detectors (Graham, MacKenzie, and Ewan (1966)).

In order to evaluate the chance contribution, two timing single channel analyzers (Canberra Industries Model 1436 TSCA) were used to set windows on the TAC spectrum. The "true plus chance" window included essentially all of the time peak to ensure a constant coincidence efficiency, while another window of precisely the same width was set off the peak to monitor "chance" events as illustrated in figure 2.13. The logic signals from either unit were allowed to trigger an enable pulse via the use of a logical OR device and a logic shaper and delay box while a separate tap from the chance TSCA created a chance routing pulse. The enable pulse opened a linear gate in both ADC's to allow the linear pulse of these events to be analyzed. Variation of the delays of both LSD devices ensured that the enable and chance pulses together with the linear pulses arrived at the appropriate times for the above analysis to take place. Provision in the ADC's for external routing allowed each addressed output from the ADC's to be tagged, if the chance condition was met, for later decoding during computer analysis. Both chance and true plus chance events were locally monitored by scalers so as to maintain a constant check on any window drifts which might have occurred.

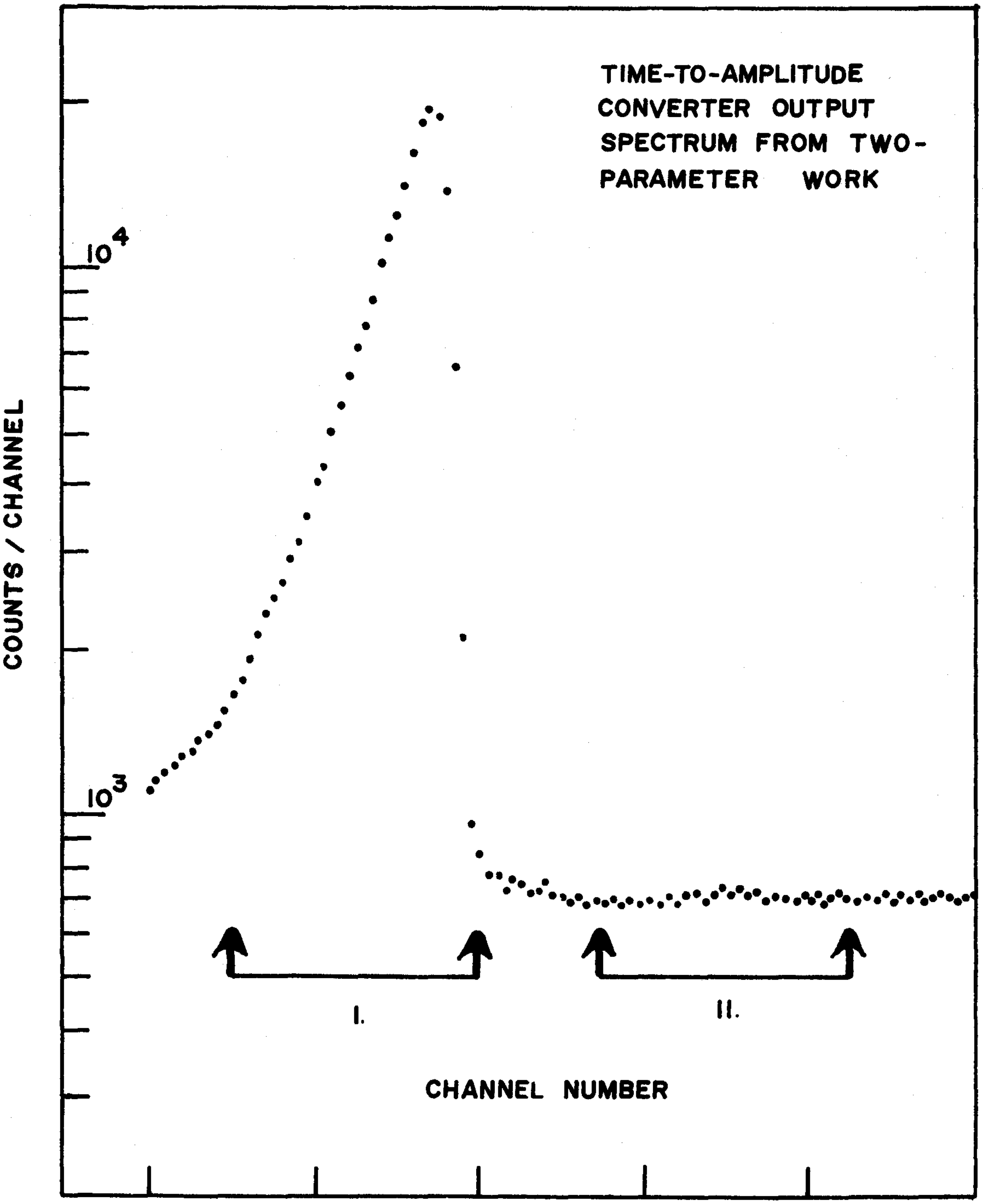

Figure 2.13 Coincidence enable region for
I. True and chance events and
II. Chance events only

Low noise amplifiers (Tennelec Model TC 203BLR) were used to shape the linear signals from the detectors. The delayed outputs were used so as to properly align in time the arrival of the timing and linear pulses. After propagation through the amplifiers, the pulses were fed through 500 feet of RG 62/u (100Ω) coaxial cable, as were the TAC output pulses, to units located in the accelerator laboratory (NSBl.). To aid in maintaining optimum resolution, count rate effects were reduced by the use of two baseline restorers (Tennelec Model TC610) positioned immediately before the signal input to the ADC's.

In addition to the units above, figure 2.12 also shows a precision pulse generator (Ortec Model 419) and a pulse height analyzing system (ND161) coupled to the 50 cm^3 detector side of the coincidence spectrometer. During the coincidence experiment these devices were employed to create a stabilized singles spectrum of ^{89}Kr in the high energy region with a large accumulation of events. However, the rather high source strengths required to generate a reasonable coincidence counting rate, gave rise to large analyzer dead time losses and a loss of energy resolution.

During operation of the coincidence system, the address outputs from the two 12-bit ADC's when taken as a pair, formed the coordinates of a coincidence event in a two dimensional matrix, whose axes represented the energy detected by each detector. These address pairs were placed sequentially in memory locations and collected in blocks of 1000 events before transcription onto magnetic tape. Control over this procedure was maintained by a PDP-9 computer integrated with the 8K memory of a Nuclear Data 3300 analyzing system and associated tape transports. A CDC 6400 computer later processed these address recorded data to tally, in core, the total number of events that occured at each coordinate of the matrix for both "true plus chance" and "chance" events.

In order to extract the coincidence information from the matrix, the following procedure was used: The total sums of "true plus chance" and "chance only" events were first projected onto both axes at reduced conversion gains. (For this experiment, a 1024 conversion gain provided a sufficient number of channels over peaks collected in the 12 cm^3 detector XADC, while a 2048 conversion gain covered the 50 cm^3 detector YADC spectra adequately.) Subtraction of these two components yielded chance corrected projections for each axes which were then used to select "gates" along one axis. In this case, the gates were set on the high resolution side involving the XADC. Each gate was obtained by selecting several adjacent channels of the projection for both peak regions and background regions making sure that the number of channels involved in each were equal. (Usually, the background channels were chosen half below and half above the peak region.) The computer was then instructed to search the original data tapes in order to sum the spectra in coincidence with both these regions along the YADC direction. The difference between the resultant spectra yielded a coincidence spectrum corrected for the underlying compton distribution from higher energy gamma rays. Simultaneously, the computer produced similar "chance only" coincidence spectra using the same gating channels. Subtraction of the "chance" and "true plus chance" coincidence spectra then provided the final spectrum representing all events in true coincidence with the photopeak(s) included in the gate. A peak found in such a spectrum indicated that the associated gamma ray was in cascade with the gamma ray whose energy (photopeak) was bracketed by the gate. The area of each peak was analyzed by hand to obtain the number of coincidence events, N_{ij}, involving the photopeaks of the pair of gamma rays in the cascade. The probability C_{ij}, of γ_i being in coincidence with γ_j is given by the following relation.

$$N_{ij} = N_o \, F_i \, (\varepsilon\omega)_i^A \, (\varepsilon\omega)_j^B \, C_{ij}$$

which yields

$$(C_{ij})_{\text{expt'l}} = N_{ij} / [N_o f_i (\varepsilon\omega)_i^A (\varepsilon\omega)_j^B]$$

where $(\varepsilon\omega)_i^A$ and $(\varepsilon\omega)_j^B$ are the photopeak detection efficiencies of detectors A and B for γ_i and γ_j respectively, F_i is the fraction of the photopeak of the i th gamma ray included in the gate, and N_o, termed the source strength, is the total number of decays occurring during the experiment. It should be noted that the above equation assumes the coincidence efficiency of the circiut to be 100%, a result that is justified from an examination of figure 2.13. The value of N_o was not directly measured but was deduced from the data for a number of gamma cascades whose position in the decay scheme was certain.

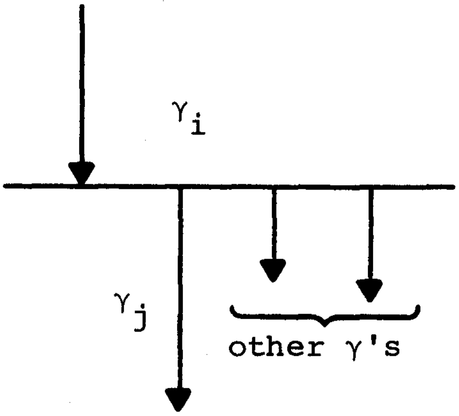

The importance of a coincidence probability to the decay scheme can be illustrated by an inspection of the accompanying sketch. This shows a level fed by a gamma ray, γ_i, and deexcited by a number of transitions, one of which is γ_j. In this case the predicted probability is

$$(C_{ij})_{\text{expected}} = I_i \cdot \frac{I_j}{\underset{\text{outgoing}}{\Sigma I}}$$

where I_i is the intensity of the incoming gamma ray and $I_j/\Sigma I$ is the fraction of the outgoing intensity which proceeds through gamma ray j. Similar calculations can be made for more complex structures. If the proposed decay scheme is correct, the $(C_{ij})_{\text{expected}}$ should agree, within experimental error, with that derived from the empirical data.

Although all spurious peaks due to chance events were removed in the analysis, the possibility of "sum peaks" appearing in the spectrum still exists. Associated with triple cascades, these occur when two of the gamma rays are detected in one detector and the third is detected in the other to form a coincident pair. The probability, C_{ijk} of this happening is given by

$$N_{ijk} = N_o(\varepsilon\omega)_i^A \, (\varepsilon\omega)_j^B \, (\varepsilon\omega)_k^B \, C_{ijk}$$

which is a factor of $(\varepsilon\omega)^B$ smaller than any genuine γ-γ coincidence. Several weak "sum peaks" have been identified in the present work corresponding to strong cascades which were found to exist in the decay of ^{89}Kr.

CHAPTER 3

The Decay of Krypton 89

Introduction

Because the krypton and xenon fission products are chemically inert, they are readily separated from other products due to fission. Thus, these elements came under close scrutiny early in isotope studies. In 1951, Dillard et. al. reported the first half lives of these fission products. Soon after, Kofoed-Hansen and Nielson, during that same year, using a mass separator, determined beta end points as well as half lives of krypton isotopes of masses 89, 90, and 91. The first decay scheme for ^{89}Kr, involving six energy levels, was proposed by Prakash in 1960. A year later, using gas sweeping techniques, Wahlgren and Meinke (1961) assigned 18 gamma rays to the decay of ^{89}Kr. Simultaneously, Ockenden and Tomlinson (1961) reported 17 gamma rays whose energies and intensities were essentially in agreement with those of Wahlgren. The first comprehensive study of levels in ^{89}Rb was accomplished by Kitching and Johns (1967) of this laboratory. Using small volume Ge(Li) detectors for singles measurements and scintillation counters for γ-γ and β-γ coincidence measurements, they were able to assign 82 gamma rays to the decay of ^{89}Kr. In their work, levels above 4 MeV were mostly tentative and weak lines throughout the work were reported but not placed. It was decided to repeat his measurements with the hope of obtaining more precise energies, intensities, and coincidence probabilities which could be used to place the decay scheme on a firmer basis. The results of the investigation contained herein, have identified 160 gamma rays as emanating from the decay of ^{89}Kr nucleus and have proposed a decay scheme incorporating 120 of these transitions.

A. Experimental Results

Since source production by the method of gas sweeping and chromatography leaves substantial amounts of both shorter and longer lived contaminants as compared to ^{89}Kr, several gamma spectra were obtained from the source material as a function of time. These spectra were used as an aid to assignment of ^{89}Kr gamma rays in the following manner. One run, taken immediately after source production, was compared to one collected nearly twenty minutes later. In this latter spectrum no lines from ^{89}Kr were present so that peaks from long lived activities could be identified. In fact, most of the lines observed in the residual activity could be attributed to the decay of ^{87}Kr, ^{88}Kr, ^{88}Rb and ^{89}Rb (see references Lycklama, Archer, and Kennett (1969) and Kitching and Johns

(1966)). Still, differentiation between transitions due to contaminants such as ^{90}Kr and ^{90}Rb remained a problem. Since a recent study by Mason and Johns (1970) revealed most of the decay properties of ^{90}Kr and ^{90}Rb, their tables were used to eliminate the contaminant lines due to these sources.

Because of the large energy range spanned by the gamma radiations associated with the deexcitation of energy levels in ^{89}Rb, various Ge(Li) detectors used at different gain settings were employed to yield those "singles" spectra listed in table 3.1. For three of these singles runs, energy calibration spectra were also obtained using the aforementioned mixed source technique. The energy calibration lines were provided by the sources enumerated in table 3.2. In order to facilitate the collection of singles data, the 0.9 cm^3 (0-1 MeV) run and the 50 cm^3 (1-3 MeV) run were collected simultaneously using the geometrical configuration shown in figure 3.1 (a). The pulses from the 0.9 cm^3 detector were analyzed with the ND161 system while those from the 50 cm^3 detector were obtained with an ND3300 analyzer. Both units were operated in the singles mode as illustrated in figure 2.7.

In addition to these runs, a separate spectrum was recorded with the 0.9 cm^3 detector to search for very low energy transitions, that is, near 20 keV. This data,

TABLE 3.1

^{89}Kr Singles Runs

Detector (by volume, cm^3)	Energy	Number of ^{89}Kr Sources used	Source to Detector Distance (cms)	Absorbers *
0.9	0-300 keV	25	~10	β
0.9	0-1 MeV	43	~ 6	β
12	0-4 MeV	72	~10	β
50	1-3 MeV	18	~ 7	β
50	0-5 MeV	114	~ 7	$\beta + \gamma$

* Beta absorber is 2.5 cm of lucite

Gamma absorber is 4.5 mm of Pb, 0.25 mm of Cu, and 0.25 mm of Cd.

TABLE 3.2

Energy Calibration Runs

Detector (by volume)	Energy Range	Energy Standards*
0.9 cc	0-300 keV	Am241
		Hg203
		Co57
		Cs137
0.9 cc	0-1 MeV	Am241
		Hg203
		Bi207[a]
		Mn54
		Y88
		Cs137
		Co60
		Ir192
50 cc	1-3 MeV	Co56[b]
		Co60
		Y88
		Na22
		Na24

* Energies as given by Marion (1968) with exceptions as noted.

a) Bernthal (1969).

b) Camp and Meredith (1971).

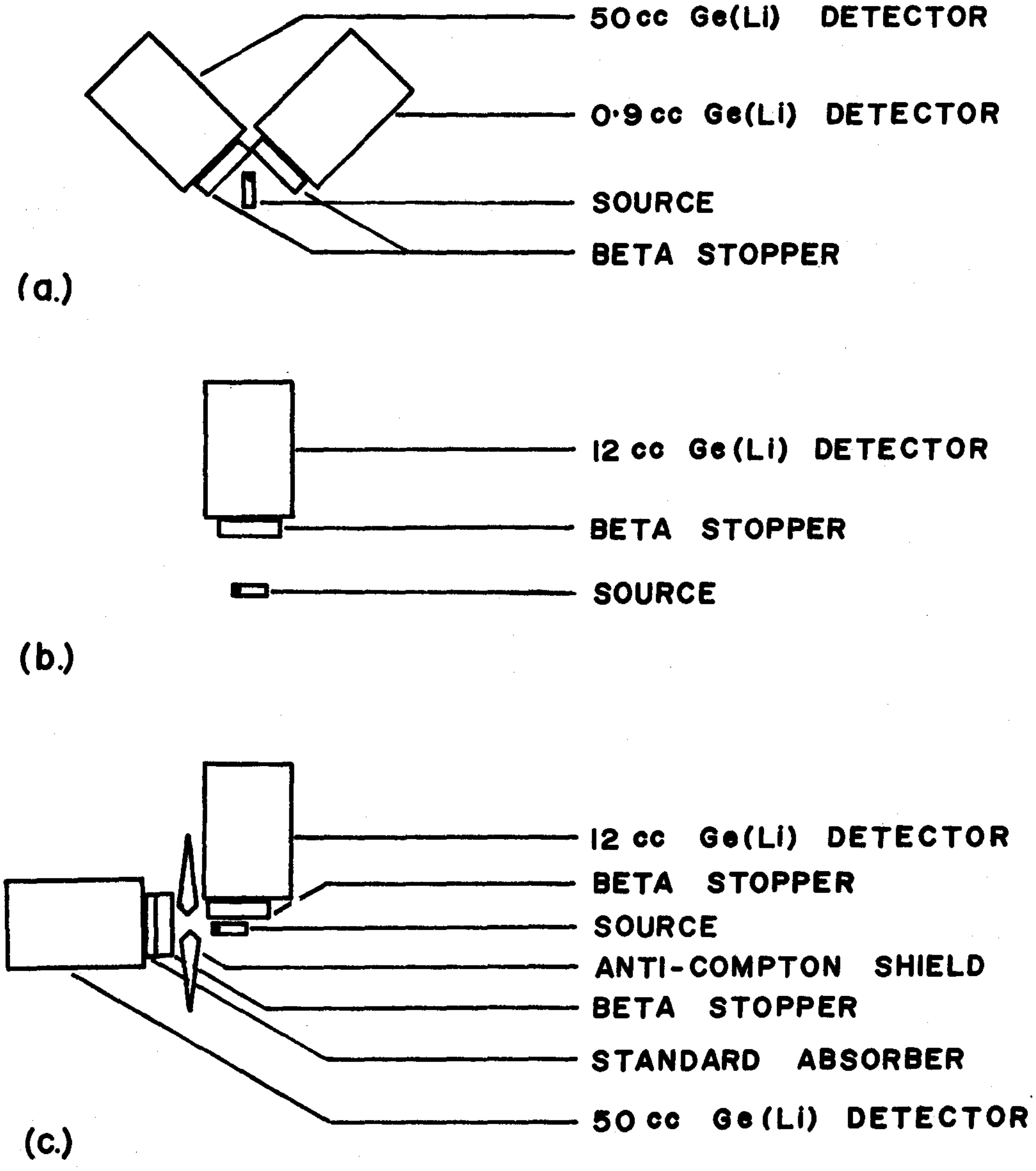

Figure 3.1 Geometrical configurations associated with
(a) 0.9 cm^3 and 50 cm^3 singles run,
(b) 12 cm^3 singles run, and
(c) 12 cm^3 x 50 cm^3 coincidence run.

however, did not reveal any features below 93 keV and so will not be presented. The 0-4 MeV spectrum from the 12 cm^3 detector run will not be illustrated since it shows no new features when compared to the same regions of spectra collected by the 0.9 cm^3 and 50 cm^3 detectors. Also, data accumulated for the contaminant decay time study (mentioned previously) and the half-life measurements (to be discussed below) have been omitted. These runs were obtained with a geometry similar to that shown in figure 3.1 (b).

For the 50 cm^3 detector, the ratio of the single escape peak to photopeak (SEP/PP) and double escape peak to photopeak (DEP/PP) were determined as a function of energy, mainly from the lines of the ^{56}Co spectrum. These curves, shown in figure 3.2, proved an important aid in determining the origin of weak lines.

For coincidence measurements, the 12 cm^3 and 50 cm^3 detectors were placed at 90° to each other in a manner shown in figure 3.1 (c). In front of each was positioned a lucite beta absorber of 2.5 cm thickness. A graded absorber composed of 4.5 mm. of lead, 0.25 mm. of copper, and 0.25 mm. of cadmium, designed to attenuate low energy gamma rays and the lead x-rays, was used with the 50 cm^3 detector. In order to reduce coincidence events created

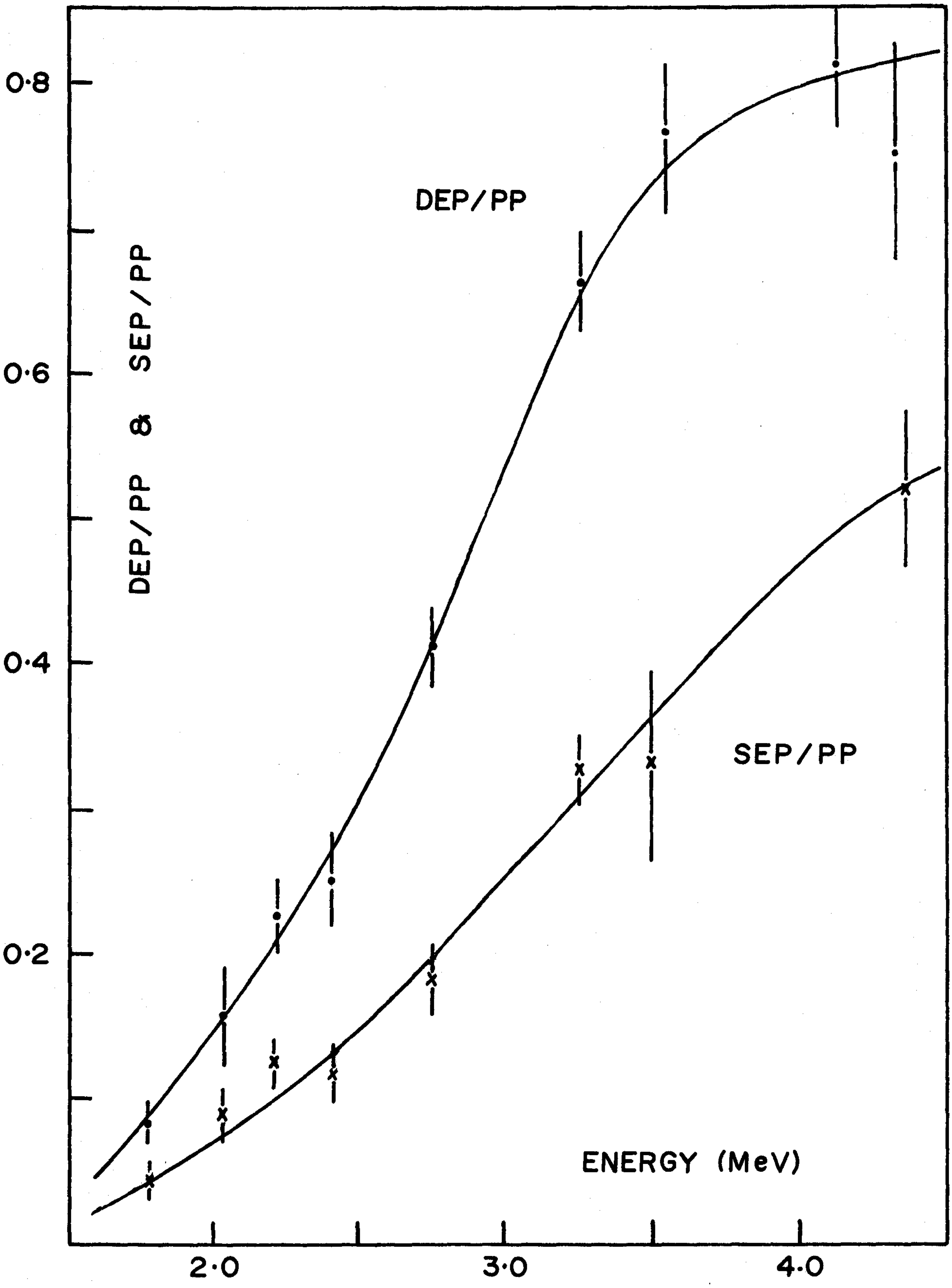

Figure 3.2 The ratio of double escape peak (DEP) and single escape (SEP) to full energy peak (PP) as a function of energy for the 50 cm^3 detector.

when a compton scattered photon, produced in one crystal, is detected in the other, an anti-compton shield was used to block the "line of sight" between the detectors. This shield consisted of a 2 cm sheet of lead wrapped in 0.25 mm. of copper and 0.25 mm. of cadmium pierced by a 1.2 cm diameter hole (Figure 3.1(c)).

3.1 Half Life Measurement

As a check on the identification of the decay process study, the half-life of ^{89}Kr was roughly determined as follows. A series of gamma spectra, each collected at 1.5 minute intervals and of 1 minute duration traced the decay for about four half-lives. The intensities of the 221, 498, and 577-586 keV lines were plotted, with suitable corrections for the dead time of the analyzer, as a function of elapsed time. These results are displayed in figure 3.3 on which a least squares fit for the decay of each gamma ray was performed. The mean half life obtained is 3.4±0.2 minutes. This is in fair agreement with the published value of 3.18±0.02 minutes. (Carlson, *et*. *al*. (1969)).

3.2 Direct Gamma Ray Measurements

Direct gamma spectra of photon emanations following the decay of ^{89}Kr are shown in figures 3.4 through 3.9. The energies and intensities deduced from such spectra are tabulated in tables 3.3 and 3.4. Table 3.3 includes the

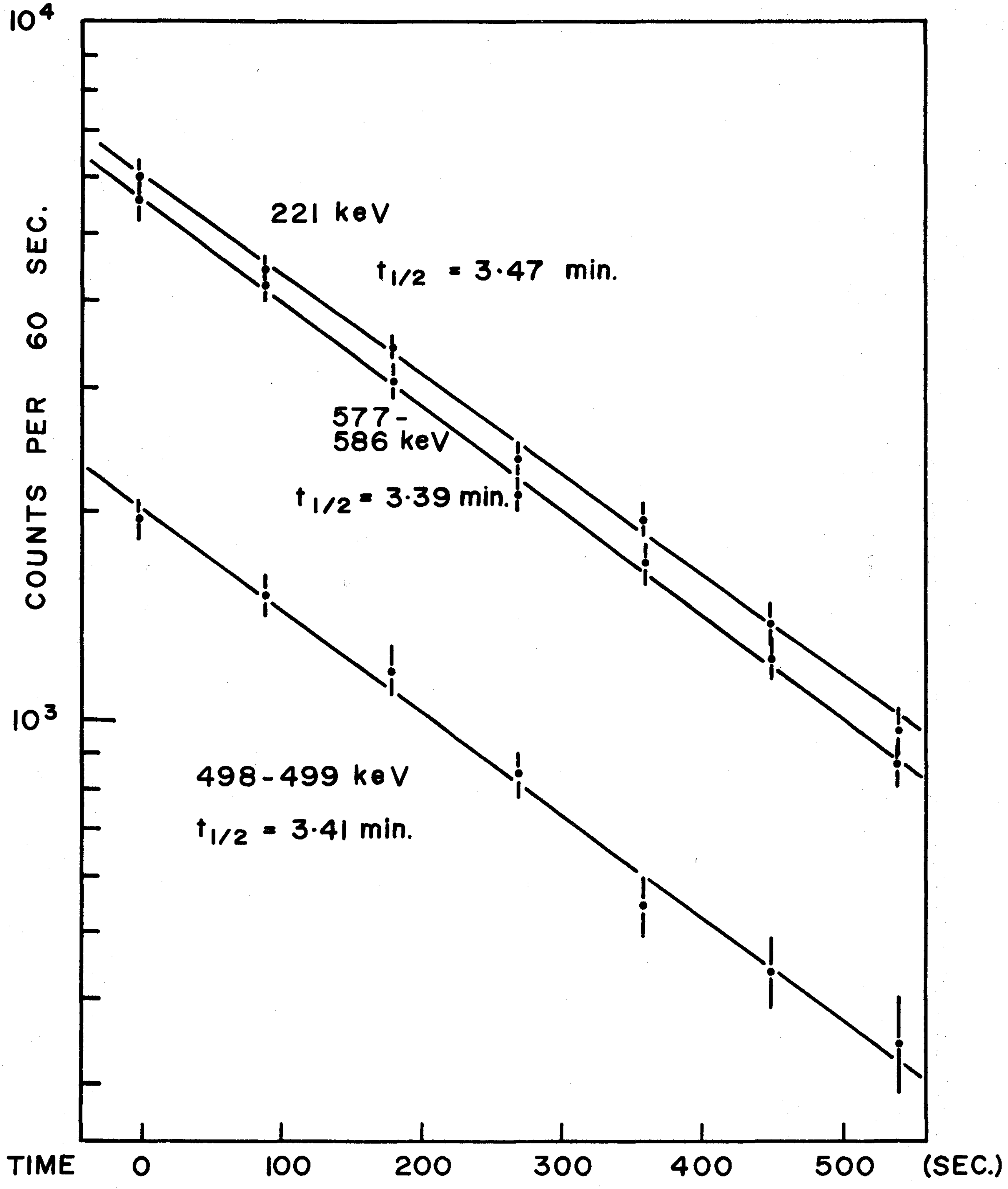

Figure 3.3 Half Life Measurement For The Decay of ^{89}Kr.

^{89}Kr lines seen in this work together with the transitions allocated to ^{89}Kr by Kitching and Johns (1967). Table 3.4(a) lists all the contaminant line energies with their identification and table 3.4(b) the single and double escape peak energies. A discussion of the figures follows.

In order not to unduly complicate the drawings, the contaminant, single, and double escape peaks have been indicated with C,S, and D respectively. Also, marginal peaks have been shown in parenthesis on the figures and not listed in the table.

Gamma rays of ^{89}Kr up to 1.2 MeV are presented in figure 3.4(a) and 3.4(b). This spectrum is characterized by a number of close multiplets marked by letters (a), (b), (c), etc. These are shown in more detail in figure 3.5. The decomposition of the illustrated structures has been carried out by a Dupont 310 curve resolver in the manner previously described.

Section (a) of figure 3.5 shows ^{89}Kr peaks at 75, 76, 79 and 83 keV. (The presence of gold X-rays is due to the gold entrance window of the 0.9 cm^3 detector.) Although the 74.9 keV peak is coincident with the energy of the strongest (K_α) lead X-ray, it is believed to originate entirely from ^{89}Kr.

The region between 90 and 190 keV contains several contaminant lines including the 151.2 keV peak due to ^{85}Kr.

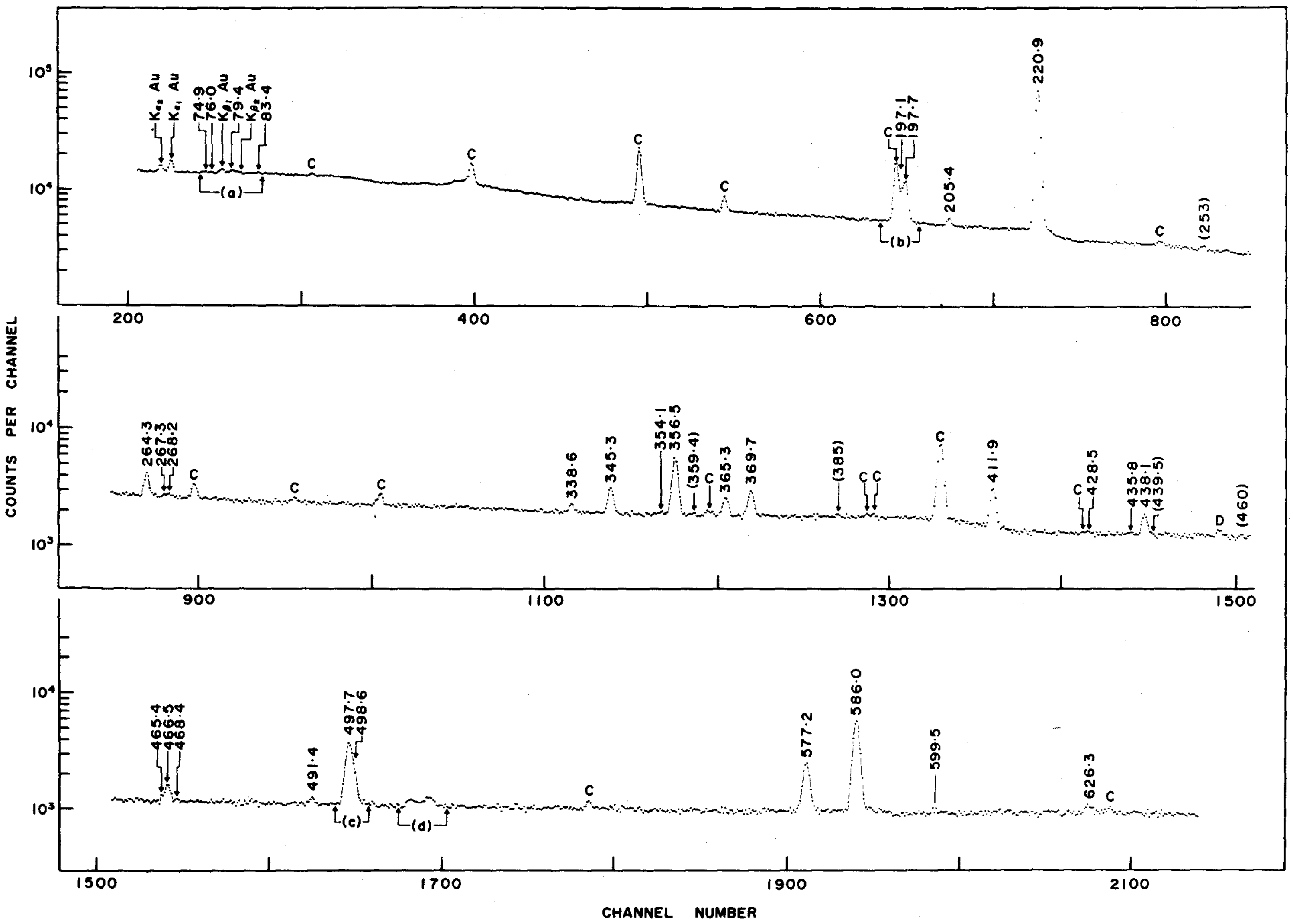

Figure 3.4(a) Singles spectrum of ^{89}Kr from 70-630 keV taken with the 0.9 cm^3 detector at a gain of 0.30 keV per channel.

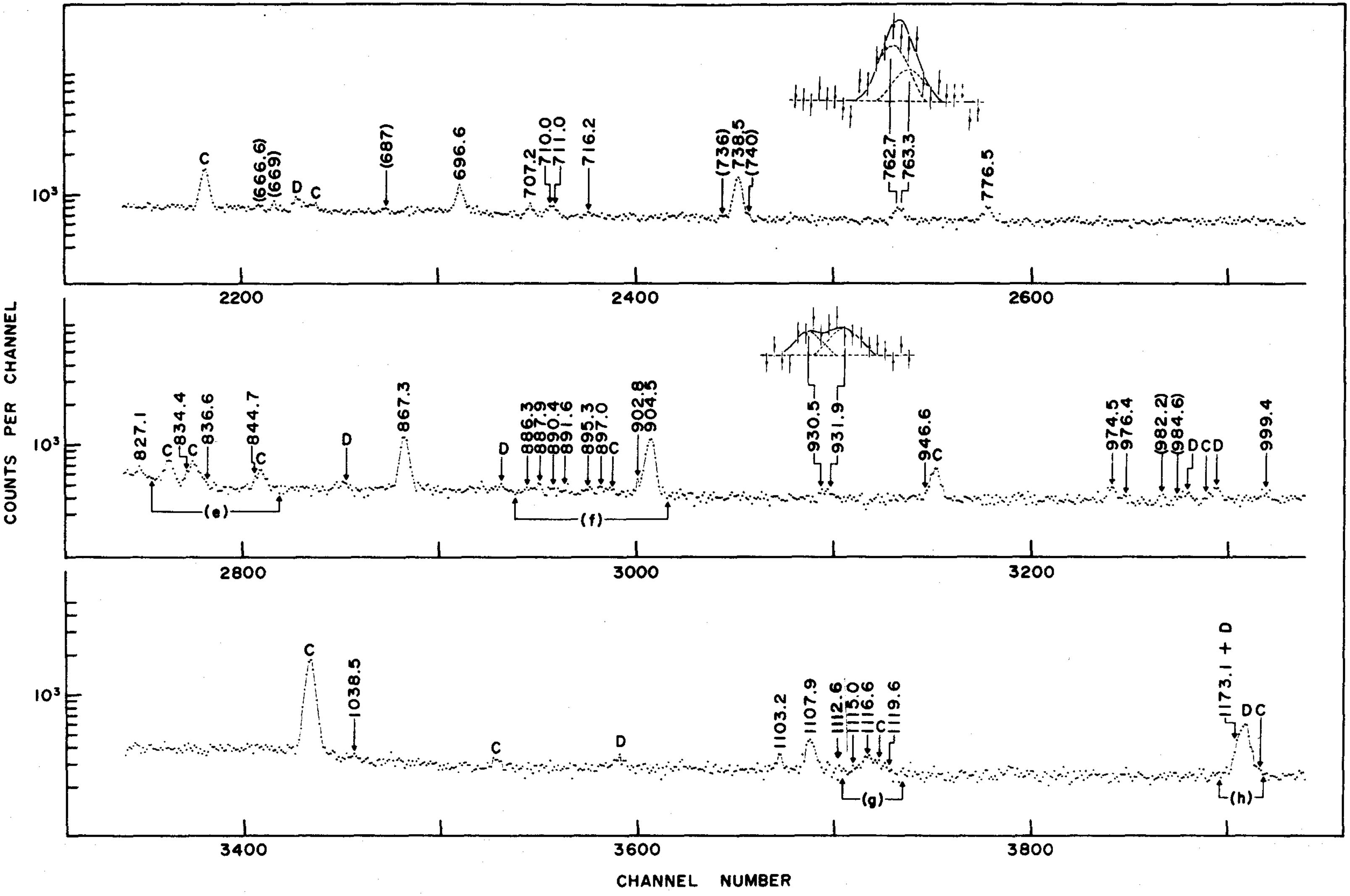

Figure 3.4(b) Singles spectrum of ^{89}Kr from 630 keV to 1.2 MeV taken with the 0.9 cm^3 detector at a gain of 0.30 keV per channel.

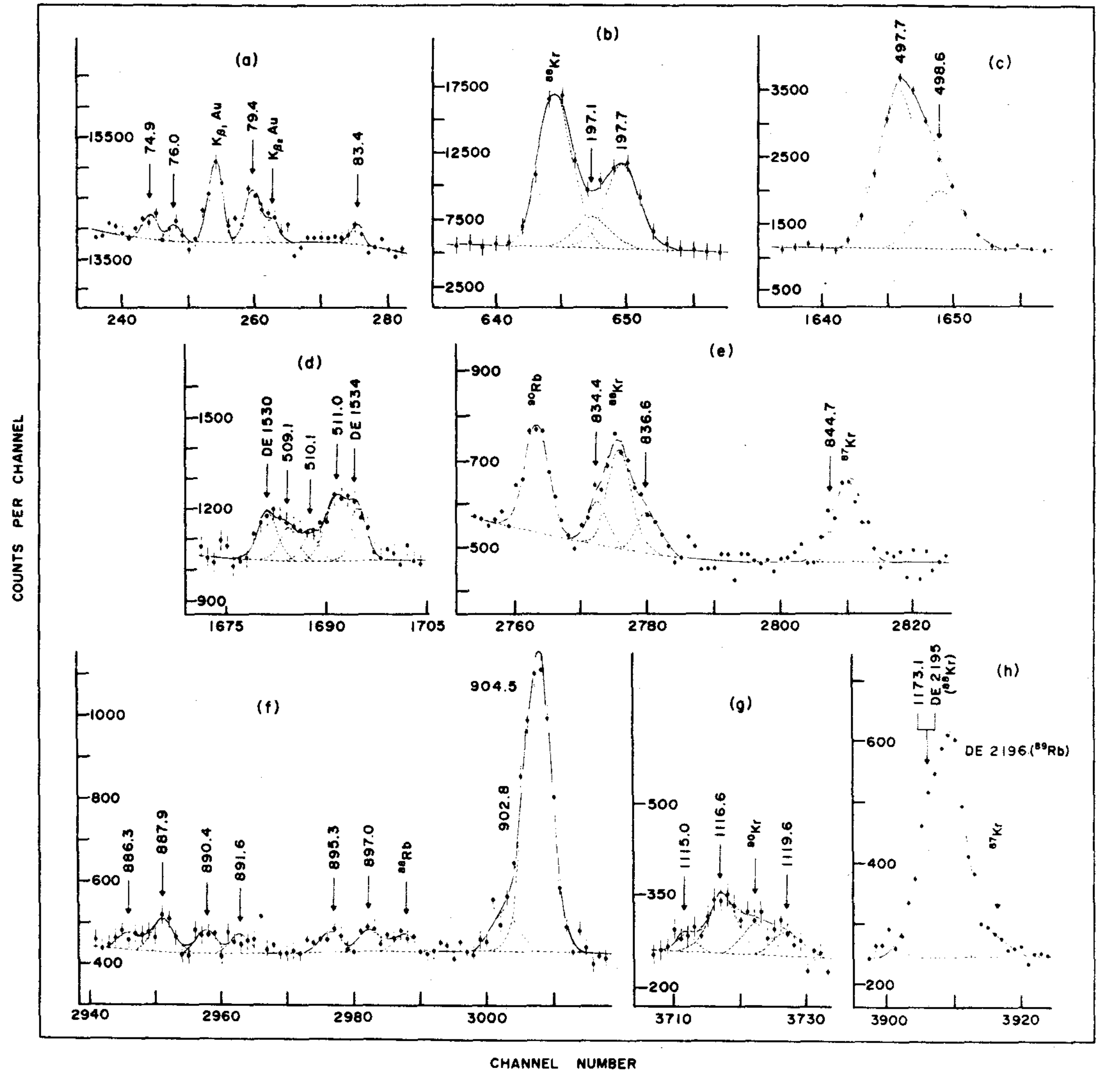

Figure 3.5 Expanded sections of the ^{89}Kr decay spectrum from 70 keV to 1.2 MeV.

Kitching *et*. *al*. had ascribed this line to the decay of ^{89}Kr. Since it appears in the present spectrum with the correct intensity relationships to the other strong ^{85}Kr line at 305 keV (Lederer, Hollander, and Perlman (1968)) and since these two lines are also present in the residual activity obtained during the decay runs, it is believed that this assignment is correct.

Section (b) reveals a triplet near 197 keV. The low energy component is one of the strongest lines in ^{88}Kr (Goodman *et*. *al*. (1970)) while the other two have been assigned to ^{89}Kr.

Twenty-five percent of the photopeak of section (h) is attributable to the 1173 keV peak from ^{89}Kr and the remainder to the double escape peak of the 2195 keV line in ^{88}Kr.

Thus from the present spectrum there is evidence for 46 new transitions observed in the decay of ^{89}Kr up to 1.2 MeV. The previously reported gamma rays of 396.0, 455.0, 527.0, 613.0, 744.0, 802.0, 860.0 and 1010 keV, listed in table 3.3 are not present.

The spectrum of ^{89}Kr from 1.1 to 3.0 MeV is shown in figure 3.6. Again, there are many partially resolved multiplets, the most complex of which are enlarged in figure 3.7. From table 3.3, these data reveal 34 lines which were either not detected or not resolved in Kitching's work. In addition, the present measurements are in serious

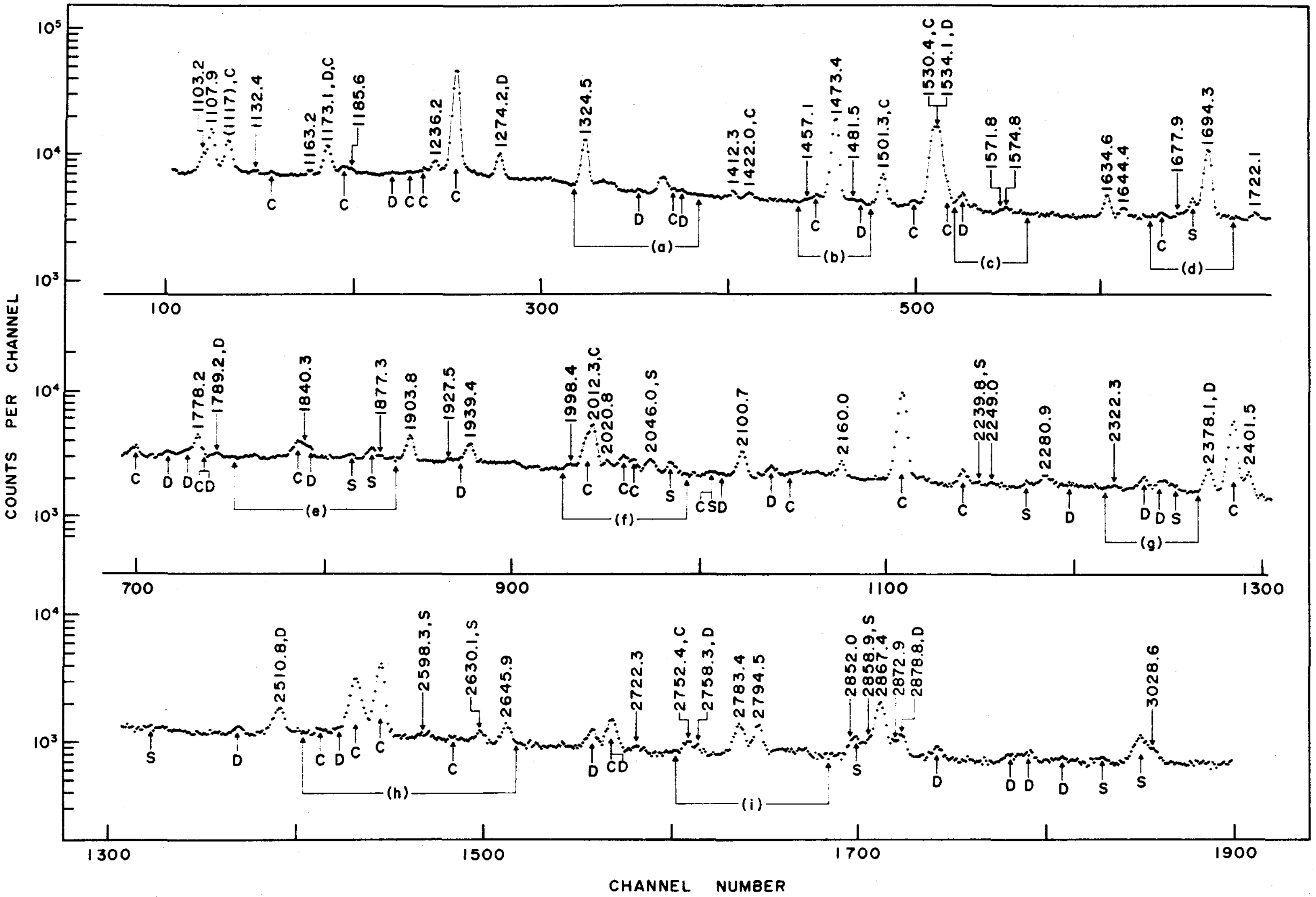

Figure 3.6 Singles spectrum of ^{89}Kr from 1.1-3.0 MeV taken with the 50 cm^3 detector at a gain of 1.1 keV per channel.

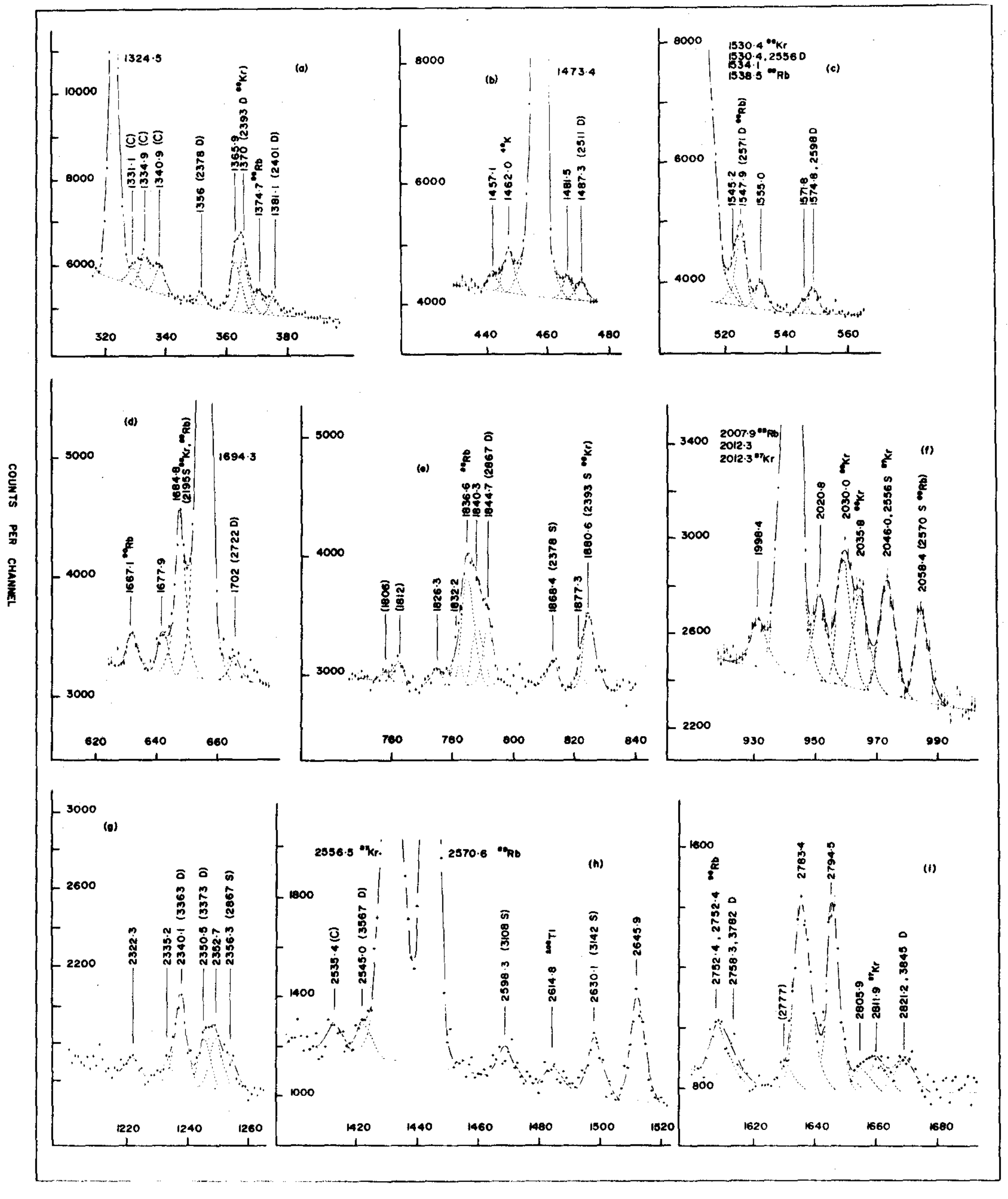

Figure 3.7 Expanded sections of the ^{89}Kr decay spectrum from 1.1-2.0 MeV.

disagreement with his intensities, which is, perhaps not surprising when one considers that his double escape peaks were relatively very much stronger than those observed in the current spectrum.

The present work shows no evidence for a 1298 keV line previously reported. A complex region near 1530 keV is a superposition of three gamma rays of energies 1530, 1534 and 1538 keV. It is estimated that 30% of the 1530 keV peak is attributable to ^{88}Kr decay while the remaining 70% arises from the decay of ^{89}Kr. Nearly 90% of the 1534 keV peak is ascribed to the same nucleus and the rest is due to the double escape of the 2556 keV gamma ray. A recent compilation (Ball, Johns and Way (1970)) has shown a 1667 keV line in ^{90}Rb which may account for the previous 1665 keV gamma ray assigned to ^{89}Kr by Kitching. The peak observed at 1760 keV is believed to be entirely due to the double escape peak of the 2783 keV transition in ^{89}Rb, while that at 2120 is a contaminant from ^{90}Rb. The 2281 keV peak, also observed by Kitching is thought to be a sum peak formed by the very strong 1032 + 1248 keV cascade in ^{89}Rb decay (Johns, et. al.(1970)). Similarly the 2598.3 keV peak is attributed to the sum peak arising from the 904 + 1694 keV cascade in ^{89}Kr. The 2618 keV peak observed by Kitching and Johns is believed to be due to ^{208}Tl (Marion (1968)) in room background. Finally, the 2945 keV peak observed by these workers can be assigned completely to the 3967 double escape peak.

The high energy spectrum (3.1-5.3 MeV) is shown in figure 3.8. A few regions of this spectrum which require detailed examination are presented in figure 3.9. A comparison with the work of Kitching and Johns (table 3.3) reveals that, although the strong peaks show reasonable agreement, there are rather large discrepancies in the weaker features. This is not unexpected since single and double escape peaks completely dominated his spectrum in this energy region.

In all, there are 6 new peaks assigned to the ^{89}Kr decay in this area, however, 16 lines, thought to originate in the ^{89}Kr decay by Kitching have not been substantiated here. The following peaks have been placed in the ^{90}Rb decay list: 3320(3318.9), 3384(3385), 4138(4136) and 4651(4646) where the unbracketed values are Kitching's and the bracketed ones have been observed in this work. Also, the 3510 keV peak of Kitching and Johns is thought to be due to the 3509.8 keV photon associated with ^{87}Rb decay. The lines of 3320(3318.9 = 4341D), 3629(3626.1 = 41365), 3823(3828.5 = 4341D), and 4138(4136 = 46465) keV are escape peaks. The peaks reported at 3125, 3894, 4040, 4096, 4123, 4396, 4481, and 4690 keV in the previous work find no basis for existence in the current study.

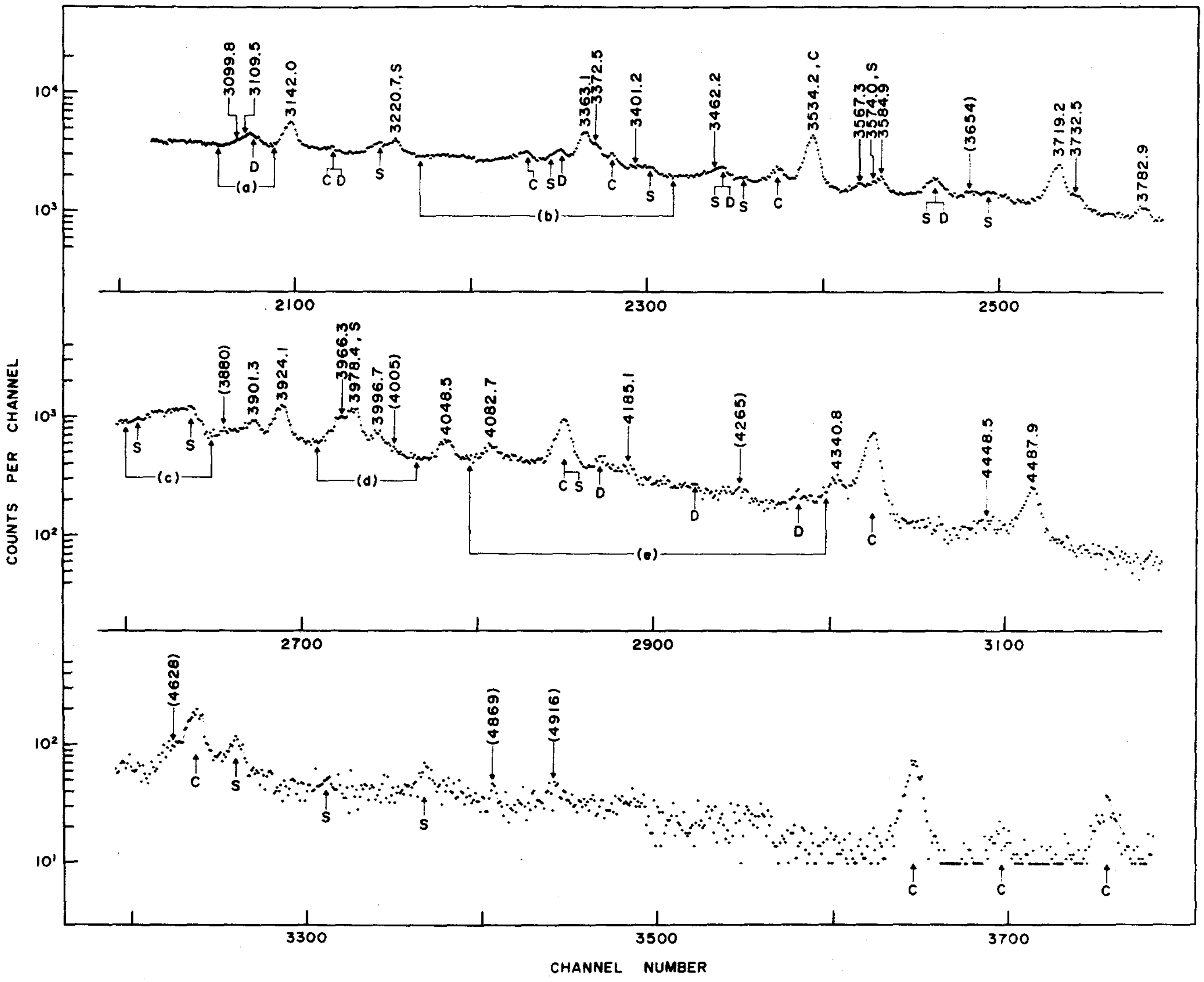

Figure 3.8 Singles spectrum of ^{89}Kr from 3.0-5.3 MeV taken with the 50 cm^3 detector at a gain of 1.3 keV per channel.

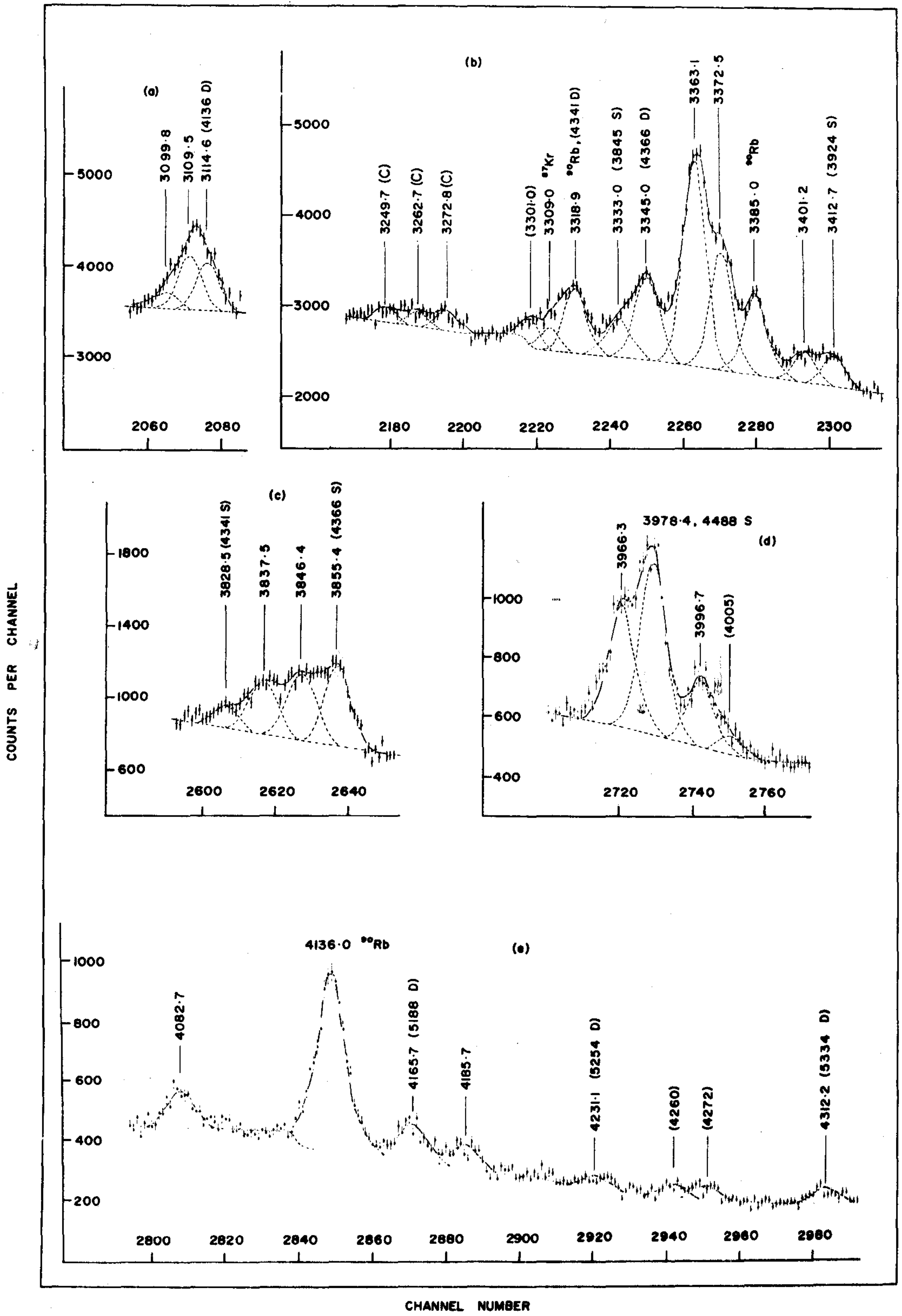

Figure 3.9 Expanded sections of the ^{89}Kr decay spectrum from 3.0–5.3 MeV.

In the overall view, a large number of new transitions have been observed in the present investigation and there is a significant improvement in the precision of the measured energies. The intensities of prominent, completely resolved lines, are believed to be correct to within 10%. For very weak or unresolved multiplets, the errors may range up to ~50%. It should be pointed out that a visual comparison of the present spectra and those of Kitching and Johns reveals obvious differences. These are in large part due to differences in irradiation and cooling periods used during source preparation. The current spectra show a higher content of long lived activities such as ^{87}Kr, ^{88}Kr, etc, and lower contributions from isotopes such as ^{90}Kr and ^{90}Rb. Also, escape peaks are much less intense in the present work.

TABLE 3.3

Gamma Ray Transitions in ^{89}Kr Decay (Previous and Present Work)

Present Work		Kitching and Johns(1967)		Present Work		Kitching and Johns(1967)	
E_γ (keV)	I_γ	E_γ (keV)	I_γ	E_γ (keV)	I_γ	E_γ (keV)	I_γ
74.9±0.5	0.06±0.02			268.2±0.5	0.48±0.12		
76.0±0.6	0.04±0.02			338.6±0.4	1.4 ±0.2		
79.4±0.5	0.14±0.02			345.3±0.2	5.4 ±0.7	345.3±0.3	8.0±1.2
83.4±0.6	0.06±0.02	85.6±0.4	2.0±0.4	354.1±0.4	0.67±0.15		
		93.6±0.4	1.6±0.4	356.5±0.2	17.8 ±1.8	356.3±0.3	26.0±2.8
		150.8±0.5	4.0±0.4	365.3±0.2	3.8 ±0.5		
197.1±0.3	2.5 ±0.5			369.7±0.2	5.8 ±0.8	368.8±0.9	8.0±1.0
197.7±0.3	7.5 ±1.5					396.0±1.0	6.0±1.2
205.4±0.5	0.80±0.20			411.9±0.2	10.9 ±1.1	411.4±0.6	6.0±1.2
220.9±0.2	100	220.6±0.3	100 ±8	428.5±0.4	0.54±0.13		
264.3±0.4	3.3 ±0.6	264.2±0.5	3.6±0.4	435.8±0.6	0.48±0.12	434.5±0.8	2.0±0.4
267.2±0.5	0.21±0.05			438.1±0.4	4.4 ±0.6	439.3±0.8	4.8±0.8

Table 3.3 Continued

Present Work		Kitching and Johns (1967)		Present Work		Kitching and Johns (1967)	
E_γ (keV)	I_γ	E_γ (keV)	I_γ	E_γ (keV)	I_γ	E_γ (keV)	I_γ
		455.0±0.8	4.8±0.8			613.0±1.5	2.0±0.8
465.4±0.5	1.2 ±0.2			626.3±0.3	3.2±0.5	627.0±1.5	6.0±1.2
466.5±0.4	3.7 ±0.6			696.6±0.5	8.4±1.0	695.0±1.5	8.0±0.8
468.4±0.6	0.48±0.12			707.2±0.5	3.5±0.5	708.0±1.5	2.8±0.4
491.4±0.5	1.0 ±0.2			710.0±0.5	2.5±0.5		
497.7±0.2	22.7 ±2.3	497.8±0.3	44 ±4	711.0±0.5	2.7±0.5		
498.6±0.2	8.0 ±1.0			716.2±0.5	1.3±0.3		
509.1±0.5	0.76±0.20			738.5±0.2	18.9±2.0	737.6±0.8	16 ±4
510.1±0.5	0.60±0.20					744 ±1	1.2±0.4
		527.0±0.5	2.0±0.8	762.7±0.5	3.8±0.5	760 ±1	2.0±0.4
577.2±0.2	21.8 ±2.2	577.2±0.3	32 ±4	763.3±0.5	2.3±0.5		
586.0±0.2	69 ±7	586 4±0.3	84 ±8	776.5±0.5	5.9±0.7	777 ±1	2.4±0.4
599.5±0.4	1.4 ±0.2					802 ±2	2.0±1.2

Table 3.3 Continued

Present Work		Kitching and Johns (1967)		Present Work		Kitching and Johns (1967)	
E_γ (keV)	I_γ	E_γ (keV)	I_γ	E_γ (keV)	I_γ	E_γ (keV)	I_γ
827.1± 0,5	3.0±0.6	823 ±5	8 ±4	930.5±0.6	2.3±0.5		
834.4± 0.6	3.6±0.7			931.9±0.6	2.8±0.5		
836.6± 0.6	3.5±0.6			946.6±0.6	2.3±0.5		
844.7± 0.6	2.6±0.5			974.5±0.6	6.4±1.0	971 ± 3	1.6±0.4
		860 ±15	2.8±0.4	976.4±0.6	2.4±0.4		
867.3± 0.2	26.7±2.7	867.5±0.5	24 ±3.6			987 ± 3	2.0±0.4
886.3± 1.0	1.0±0.5			999.4±0.7	3.4±0.6		
887.9± 0.6	3.2±0.6					1010 ±30	4 ±2.0
890.4± 1.0	1.5±0.5			1038.5±0.8	1.6±0.4	1077 ± 1	3.6±0.4
891.6± 1.0	1.0±0.5			1103.2±0.6	3.8±0.6	1105.3± 0.6	21.6±2.8
895.3± 1.0	1.5±0.5			1107.9±0.5	13.3±1.5		
897.0± 0.6	2.4±0.5			1112.6±0.8	1.7±0.4		
902.8± 0.6	4.0±0.7			1115.0±0.8	0.8±0.3		
904.5± 0.2	33 ±3	903.5±0.7	29.2±4.0	1116.6±0.5	5.1±0.7	1116.5± 1.0	10 ±2

Table 3.3 Continued

Present Work		Kitching and Johns (1967)		Present Work		Kitching and Johns (1967)	
E_γ (keV)	I_γ	E_γ (keV)	I_γ	E_γ (keV)	I_γ	E_γ (keV)	I_γ
1119.6±0.7	1.9 ±0.5			1473.4±0.4	38.6 ±3.0	1472.1± 0.6	38 ±6
1132.4±1.0	0.5 ±0.2			1481.5±0.8	0.69±0.2		
1163.2±1.0	0.66±0.2			1501.3±0.5	7.5 ±0.8	1500 ± 2	3.2±0.8
1173.1±0.6	3.8 ±0.5	1173 ±1	4 ±0.8	1530.4±1.0	20 ±3		
1185.6±0.8	0.91±0.3			1534.1±0.5	25 ±3	1533.4± 1.0	44 ±8
1236.2±0.7	2.7 ±0.4			1545.2±1.5	0.5 ±0.2		
				1555.0±0.8	0.6 ±0.2		
1274.2±0.5	7.1 ±0.8	1273 ±2	1.2±0.24	1571.8±1.0	0.34±0.10		
		1298 ±2	2.0±0.4	1574.8±0.8	0.85±0.15		
1324.5±0.5	15.4 ±1.5	1324 ±2	6.4±1.6	1634.6±0.7	4.6 ±0.7	1636 ± 2	4.0±1.2
1365.9±1.5	0.7 ±0.2			1644.4±0.8	1.8 ±0.3		
1412.3±0.8	1.27±0.3					1655 ± 2	2.8±0.8
1422.0±0.8	1.30±0.3			1677.9±1.0	0.40±0.10	1670 ±30	4.0±2.0
1457.1±1.0	0.41±0.12						

Table 3.3 Continued

Present Work		Kitching and Johns (1967)		Present Work		Kitching and Johns (1967)	
E_γ (keV)	I_γ	E_γ (keV)	I_γ	E_γ (keV)	I_γ	E_γ (keV)	I_γ
1694.3±0.5	26.1 ±2.6	1691.6±0.6	18.8±3.2	2020.8±1.0	1.6 ±0.3	2020 ± 2	6.8±1.2
1722.1±0.8	1.3 ±0.2			2046.0±1.0	1.0 ±0.3		
		1760 ±2	12 ±2.4	2100.7±0.7	5.6 ±0.7		
1778.2±0.8	4.8 ±0.6	1755 ±2	11.2±2.4			2120 ± 2	4.0±1.2
1789.2±1.0	0.65±0.20			2160.0±0.8	3.1 ±0.6		
1826.3±0.8	0.43±0.14			2239.8±1.5	0.26±0.15		
1832.2±1.5	1.0 ±0.2			2249.0±1.0	0.42±0.15		
1840.3±0.8	2.8 ±0.4	1843 ±1	4.4±1.6	(Suspected sum peak)		2281 ± 2	8 ±1.6
1877.3±1.0	0.42±0.14			2322.3±1.0	0.64±0.2		
1903.8±0.6	5.6 ±0.6	1902 ±1	4.8±0.8	2335.2±2.0	0.5 ±0.3		
1927.5±1.0	0.55±0.7			2352.7±1.5	1.4 ±0.4		
1939.4±0.8	4.5 ±0.6	1939 ±3	4.8±0.8	2378.1±0.8	4.5 ±0.6	2380 ± 3	1.6±0.4
1998.4±1.0	0.88±0.30			2401.5±0.8	4.6 ±0.6		
2012.3±1.0	9 ±2	2011 ±2	10.4±2.0	2510.8±2.0	1.2 ±0.5		

Table 3.3 Continued

Present Work		Kitching and Johns(1967)		Present Work		Kitching and Johns(1967)	
E_γ (keV)	I_γ	E_γ (keV)	I_γ	E_γ (keV)	I_γ	E_γ (keV)	I_γ
		2618 ±2	5.6±1.2	2878.8±1.0	3.0 ±0.6		
2630.1±1.5	0.69±0.23					2946 ± 3	1.2 ±0.4
2645.9±1.0	2.6 ±0.4	2644 ±3	3.2±0.4	3028.6±1.5	2.2 ±0.4		
2722.3±1.5	0.58±0.2			3099.8±1.5	0.6 ±0.2		
2752.4±1.0	0.9 ±0.3	2753 ±2	2.8±0.8	3109.5±1.0	1.7 ±0.3	3108 ± 2	0.8 ±0.16
2758.3±1.0	0.55±0.2	2762 ±1	2.0±0.8			3125 ± 2	0.64±0.12
2783.4±0.8	4.7 ±0.6			3142.0±1.0	6.2 ±0.8	3143 ± 2	3.6 ±0.8
2794.5±1.0	4.4 ±0.6	2790 ±2	5.6±1.6	3220.7±1.5	1.8 ±0.5		
2805.9±1.0	0.55±0.2					3320 ± 2	1.00±0.2
2821.2±1.5	0.28±0.14			3363.1±1.0	6.2 ±0.8	3363 ± 2	4.8 ±0.8
2852.0±1.5	1.1 ±0.3			3372.5±1.0	3.6 ±0.6		
2858.9±1.5	0.27±0.14					3384 ± 2	1.0 ±0.2
2867.4±0.8	11.0 ±1.5	2865.7±2.0	11.2±2.4	3401.2±1.5	0.66±0.2		
2872.9±1.0	1.3 ±0.5						

Table 3.3 Continued

Present Work		Kitching and Johns (1967)		Present Work		Kitching and Johns (1967)	
E_γ (keV)	I_γ	E_γ (keV)	I_γ	E_γ (keV)	I_γ	E_γ (keV)	I_γ
3462.2±1.5	0.68±0.2	3480 ± 30	0.8 ±0.4			3894 ± 2	0.56±0.12
		3510 ± 2	1.2 ±0.24	3901.3±1.5	0.98±0.3	3904 ± 3	0.56±0.12
3534.2±0.8	8.2 ±1.0	3534 ± 1	6.16 ±1.2	3924.1±1.0	2.9 ±1.0	3924 ± 2	1.2 ±0.2
3567.3±1.5	0.33±0.1	3568 ± 2	0.340±0.08	3966.3±1.0	1.2 ±0.3	3962 ± 2	0.6 ±0.2
3574.0±1.5	0.32±0.15			3978.4±1.5	2.3 ±0.6	3976 ± 2	1.2 ±0.4
3584.9±0.8	1.8 ±0.3	3582 ± 1	1.2 ±0.4	3996.7±1.5	0.96±0.3	3993 ± 2	0.4 ±0.12
		3629 ± 2	0.32 ±0.08	(4005.7±1.5)	(0.2 ±0.1)	4005 ± 2	0.28±0.08
(3654 ±1.5)	(0.2 ±0.1)	3653 ± 2	0.28 ±0.08			4040 ± 3	0.24±0.04
3719.2±0.6	5.9 ±0.8	3720 ± 1.5	3.2 ±0.04	4048.5±1.5	0.86±0.3	4048 ± 3	0.36±0.08
3732.5±1.0	1.5 ±0.3	3734 ± 2	0.8 ±0.4			4069 ± 5	0.16±0.04
3782.9±1.0	1.5 ±0.3			4082.7±1.5	0.62±0.2	4080 ± 2	0.52±0.12
		3823 ± 3	0.32 ±0.08			4098 ± 5	0.20±0.08
3837.5±1.5	0.50±0.15	3834 ± 3	0.32 ±0.08			4123 ± 5	0.20±0.08
3846.4±1.5	1.0 ±0.2	3843 ± 3	0.32 ±0.08			4138 ± 2	1.36±0.28

Table 3.3 Continued

Present Work		Kitching and Johns (1967)		Present Work		Kitching and Johns (1967)	
E_γ (keV)	I_γ	E_γ (keV)	I_γ	E_γ (keV)	I_γ	E_γ (keV)	I_γ
		4147 ± 5	0.20±0.04			4481 ± 3	0.032±0.008
4185.1±1.5	0.38±0.13	4185 ± 5	0.12±0.04	4487.9±1.0	1.1±0.3	4493 ± 3	0.24 ±0.04
4340.8±1.0	1.0 ±0.3	4343 ± 3	0.20±0.04			4651 ± 3	0.20 ±0.04
		4369 ± 3	1.16±0.24			4690 ± 3	0.024±0.008
4448.5±1.5	0.20±0.07						

TABLE 3.4 (a)

Contaminant Peaks as Identified in the Direct Gamma Ray Spectra

Peak Energy (keV)	Isotope of Origin	Peak Energy (keV)	Isotope of Origin	Peak Energy (keV)	Isotope of Origin
93.6	^{91}Rb	630	?	1141.8	^{88}Kr
123	^{90}Kr	657.8	^{89}Rb	1176.3	^{87}Kr
151.2	^{85}Kr	674	^{87}Kr	1181.7	^{88}Kr
166	^{88}Kr	831.5	^{90}Rb	1220.2	^{89}Rb
196	^{88}Kr	835.3	^{88}Kr	1229.6	^{89}Rb
243	^{90}Kr	845.6	^{87}Kr	1248.2	^{89}Rb
272.6	^{89}Rb	897.0	^{88}Rb	1331.1	?
289	^{89}Rb	947.7	^{89}Rb	1334.9	?
304.9	^{85}Kr	982.2	?	1340.9	?
362.4	^{88}Kr	984.6	?	1374.7	^{90}Rb
390	?	989.0	?	1422.0	^{90}Rb (partly)
402	^{87}Kr	1031.8	^{89}Rb	1462.0	^{40}K (partly)
427.5	^{89}Rb	1060.1	^{90}Rb	1501.3	?
539.9	^{90}Kr	1118.1	^{90}Kr	1518.9	^{88}Kr

Table 3.4 (a) Continued

Peak Energy (keV)	Isotope of Origin	Peak Energy (keV)	Isotope of Origin	Peak Energy (keV)	Isotope of Origin
1530.4	^{88}Kr(partly)	2392.7	^{88}Kr	3385.0	^{90}Rb
1538.5	^{89}Rb	2535.4	?	3509.8	^{89}Rb
1667.1	^{90}Rb	2556.5	^{87}Kr	3534.2	^{90}Rb(partly)
1740.9	^{87}Kr	2570.6	^{89}Rb	3889	^{90}Rb
1782.4	^{90}Kr(partly)	2614.8	^{208}Tl	4136.0	^{90}Rb(partly)
1836.6	^{88}Rb	2708.0	^{89}Rb	4366.0	^{90}Rb
2007.9	^{89}Rb	2752.4	^{90}Rb(partly)	4646.6	^{90}Rb
2012.3	^{87}Kr	2811.9	^{87}Kr	5187.8	^{90}Rb
2030.0	^{88}Kr	3161.5	?	5254.5	^{90}Rb
2035.8	^{88}Kr	3249.7	?	533.6	^{90}Rb
2082.1	?	3262.7	?		
2128.7	^{90}Rb	3272.8	?		
2195.9	^{89}Rb, ^{88}Kr	3309.8	^{87}Kr		
2231.9	^{88}Kr	3318.9	^{90}Rb(partly)		

TABLE 3.4 (b)

Single and Double Escape Peaks as Observed in the Direct Gamma Ray Spectra

Peak Energy (keV)	Peak Origin (keV)	Peak Energy (keV)	Peak Origin (keV)	Peak Energy (keV)	Peak Origin (keV)
452.0	1473D	1370.0	2393D	1880.6	2393S
508.0	1530D	1381.1	2401D	1933.6	2956D
512.0	1534D	1487.3	2511D	2046.0	2556S
672.0	1694D	1534.1	2556D	2058.4	2570S
858.4	1881D	1547.9	2570D	2087.5	2598S
882.0	1903D	1574.8	2598D	2087.5	3108D
986.2	2008D	1684.8	2195S	2118.4	3142D
990.4	2012D	1701.2	2722D	2239.8	2752S
1079.0	2101D	1760.6	2783D	2270.4	2783S
1173.1	2195D	1770.8	2794D	2294.7	3319D
1181.7	1694S	1784.4	2804D	2340.1	3363D
1210.6	2232D	1789.2	2811D	2350.5	3373D
1274.2	2295D	1844.7	2867D	2356.3	2867S
1356.0	2378D	1868.4	2378S	2378.1	3401D

Table 3.4 (b) continued

Peak Energy (keV)	Peak Origin (keV)	Peak Energy (keV)	Peak Origin (keV)	Peak Energy (keV)	Peak Origin (keV)
2434.7	2945S	2998.4	3510S	3828.5	4341S
2486.5	3510D	3021.4	3534S	3855.4	4366S
2510.8	3534D	3075.5	3585S	3978.4	4488S
2545.0	3567D	3114.6	4136D	4165.7	5188D
2598.3	3108S	3161.5	4185D	4136.0	4646S
2630.1	3142S	3207.6	3719S	4231.1	5254D
2696.3	3719D	3220.7	3732S	4312.2	5334D
2708.0	3732D	3318.9	4341D	4676.6	5188S
2758.3	3782D	3333.0	3845S	4740.4	5254S
2821.2	3845D	3345.0	4366D	4823.0	5334S
2852.0	3363S	3412.7	3924S		
2858.9	3373S	3468.3	3978S		
2878.8	3901D	3468.3	4488D		
2900.3	3924D	3484.0	3996S		
2944.7	3967D	3574.0	4082S		
2955.5	3978D	3626.1	4136S		
2974.1	3996D	3626.1	4646D		

3.3 γ-γ Coincidence Measurements

The two parameter gamma-gamma coincidence measurements were taken with the Ge(Li) detectors and experimental arrangement described at the beginning of this chapter. Over a period of a week, 13.5×10^6 coincidence events were recorded at an average (true and chance)/chance rate of 10:1. The chance events were removed from the coincidence matrix by the procedure already discussed. The resulting 1024 x 2048 channel array was analyzed by setting "gates" along the 1024 dimension and analyzing the corresponding 2048 channel spectra. Figure 3.10 shows the projection of the coincidence events on the 1024 channel axis obtained with a gain of 1.3 keV per channel. Figure 3.11 displays a similar projection of events on the other (2048) axis collected at a 2.7 keV per channel dispersion. In the former spectrum the region of channels included in any gate is indicated by the underscored U-bracket about the labelled peak energy. The sum of the events in these gated channels, less the sum of the events in an equal number of nearby but off-peak channels (not shown in figure 3.10) represents the true spectrum in coincidence with the gating transition. The coincidence spectra are presented in figures 3.12 together with relevant portions of the decay scheme. Energies, enclosed by brackets, indicate peaks that have not been included in the partial decay scheme of that gate. Since much of the coincidence data provides redundant information, only a selection of data

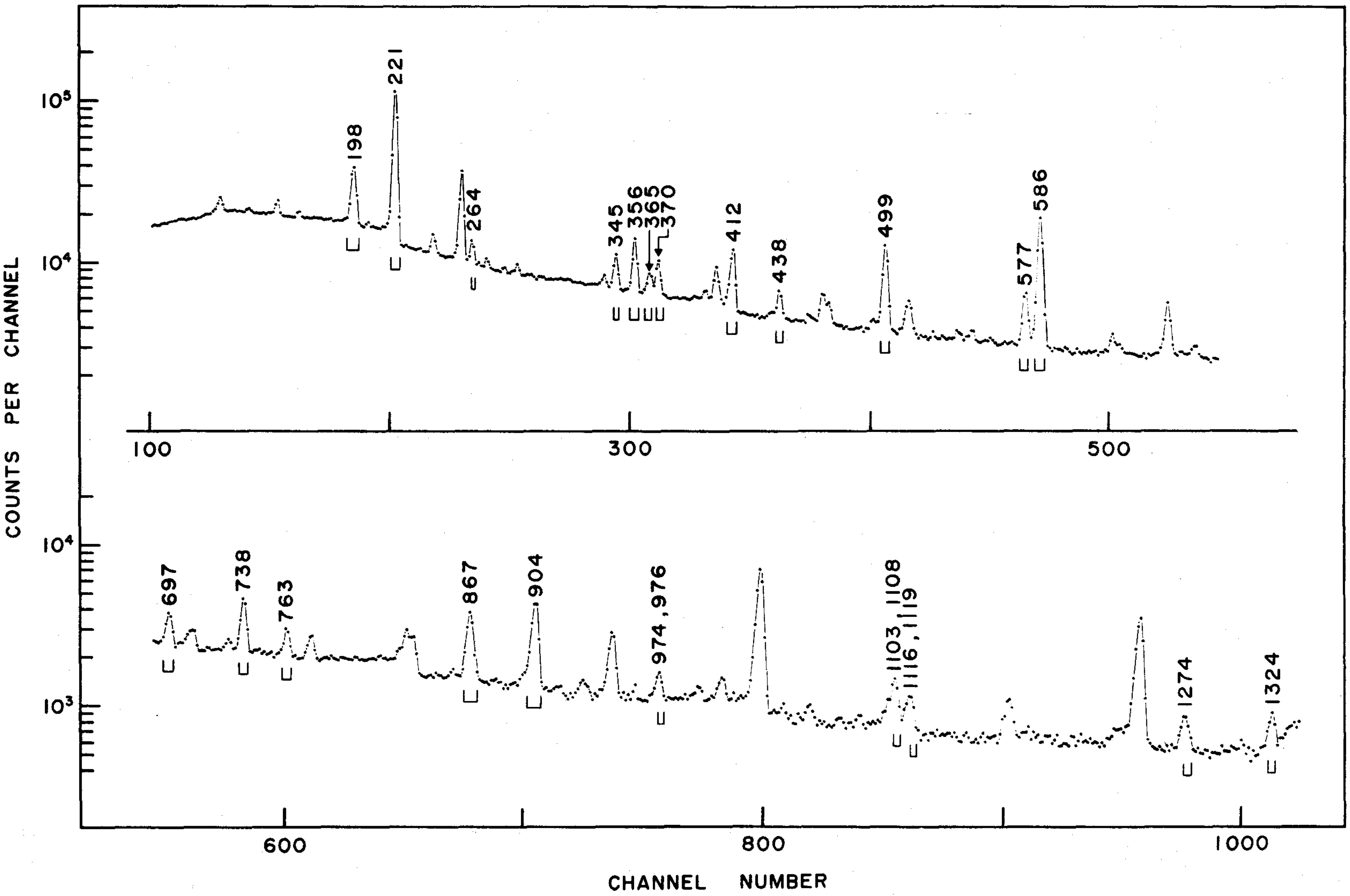

Figure 3.10 The spectrum of ^{89}Kr coincidence events projected onto the 1024 channel axis with gate selection as indicated.

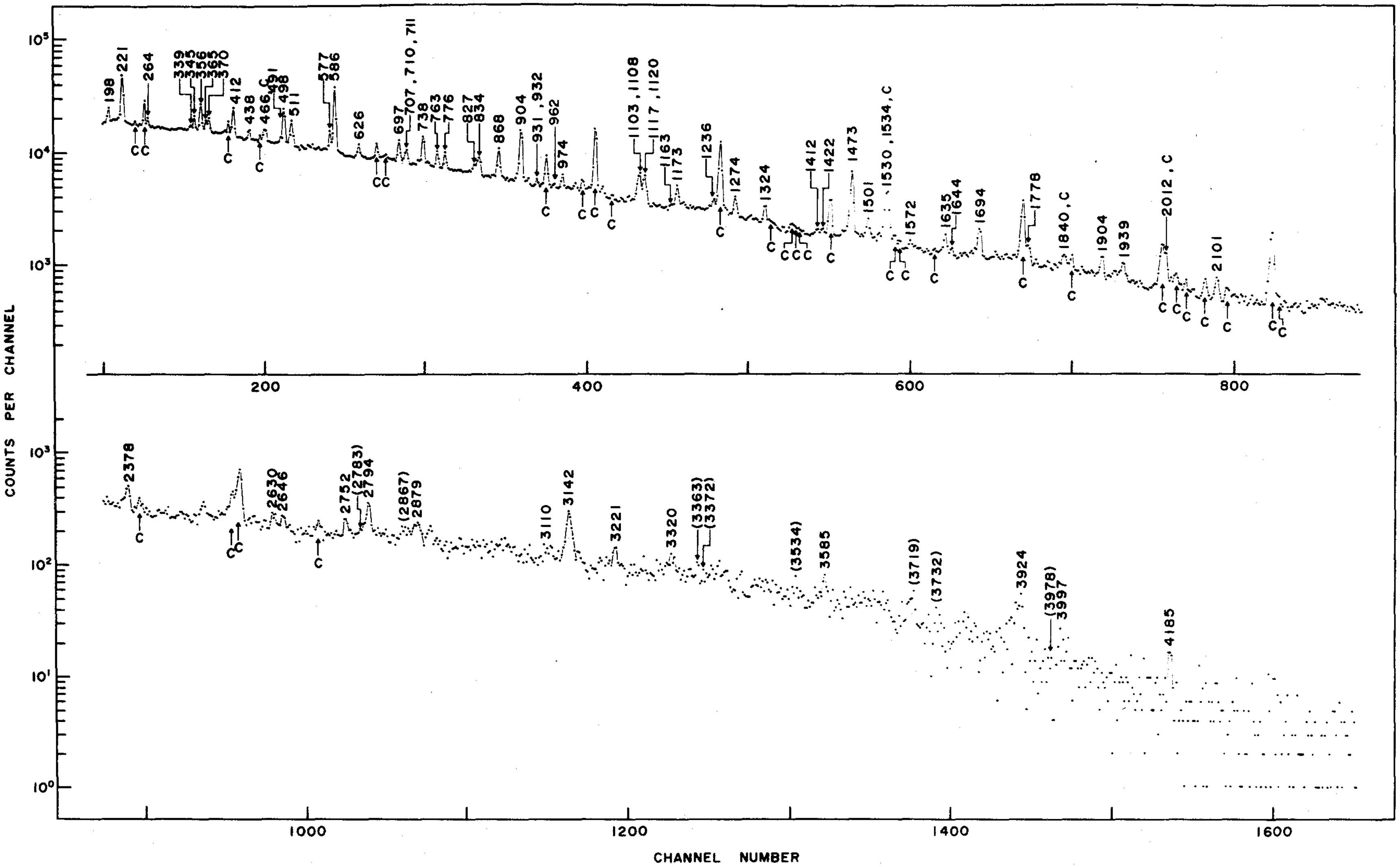

Figure 3.11 The spectrum of ^{89}Kr coincidence events projected onto the 2048 channel axis.

sufficient to justify the proposed decay scheme is presented in this thesis.

The coincidence results derived from all the gates have been analyzed to yield the coincidence probabilities of table 3.5. The first two columns in this table list the gamma ray pairs, γ_i and γ_j, for which a coincidence quotient was determined. Those entries under γ_j which are enclosed in round brackets indicate gamma rays that have not appeared in any of the Ge(Li) singles runs. The next column presents the experimental values of C_{ij}. Although specific errors (due mainly to statistical uncertainty in the peak area) have not been quoted, the following rule-of-thumb may be applied: for a C_{ij}; less than 0.5, an experimental error in the range from 30 to 40% is expected; for $0.5 \leq C_{ij} \leq 2.0$ errors are near 20%; if the C_{ij} exceeds 2.0, the uncertainties are generally calculated to be less than 10%. The fourth column tabulates the values of the expected C_{ij}'s on the basis of the proposed partial decay scheme.

The experimental values of C_{ij} are generally seen to agree with the expected C_{ij}'s to within ~10% for well defined peaks. However, larger discrepancies (up to 30%) between the experimental and predicted coincidence probabilities occasionally occur. The necessary absorbers and shields used for each detector in this coincidence experiment required rather large source-to-detector distances (~7 cm)

TABLE 3.5

γ-γ Coincidence Probabilities

γ_i	γ_j	C_{ij} experimental	C_{ij} expected
197.1 +197.7	221	3.13	2.63
	339	0.89	0.80
	365	0.40	0.24
	370	0.30	~0.1
	412	4.08	4.88
	491	0.48	-
	499	4.01	4.00
	586	4.58	4.64
	626	1.61	2.10
	707	0.20	~0.2
	776	2.08	2.63
	867	2.46	1.6
	904	1.06	1.5
	1173	1.10	0.25
	1534	2.14	1.6
221	198	3.16	2.63
	264	1.77	0.85
	356	18.7	17.8
	365	4.94	3.84
	412	0.78	0.57
	438	1.36	1.00
	466	1.90	1.80
	491	0.48	-
	499	4.14	4.00
	626	2.16	1.50
	697	2.30	2.30
	710	5.99	5.20
	738	0.95	0.99

Table 3.5 continued

γ_i	γ_j	C_{ij} experimental	C_{ij} expected	γ_i	γ_j	C_{ij} experimental	C_{ij} expected
	763	1.74	2.05		2794	1.25	1.98
	776	7.45	5.90		2879	1.74	1.35
	837	0.57	0.40		3110	0.75	1.70
	904	16.0	12.0		3142	1.79	2.78
	974	5.68	6.42		3837	~0.2	0.50
	1103,1108	5.70	4.53		3924	1.78	2.89
	1117,1119	4.08	3.30		3997	~1.0	~1.0
	1173	2.81	2.00		4185	~0.5	0.4
	1473	39.2	38.6	264	221	1.54	0.85
	1635	0.90	1.60		345	1.36	1.68
	1644	1.38	-		438	0.34	0.0
	1778	5.88	4.84		499	2.00	1.60
	1939	3.79	4.49		586	1.62	1.59
	2012	1.43	1.48		626	0.69	0.99
	2378	3.08	4.64		711	0.75	0.76
	2646	2.01	2.60		931	0.58	0.89

Table 3.5 continued

γ_i	γ_j	C_{ij} experimental	C_{ij} expected
	1501	0.20	0.0
	221	~0.1	0.30
345	264	1.56	1.68
	365	~0.1	0.30
	499	1.00	1.25
	586	6.20	5.11
	626	~0.24	~0.4
	763	2.64	1.90
	890	0.50	0.70
	904	0.91	1.0
356	221	22.2	17.8
+354	466	0.76	0.20
	763	0.95	0.36
	904	1.69	1.65
	1117	3.08	2.58
	(2285)	0.36	-
	2794	1.38	1.96
	2852	0.59	0.50
	3142	2.17	2.76
365	198	0.97	0.30
+(370)	221	5.30	+0.4+1.8+6.00
+(356)	345	0.15	0.25
	412	0.26	0.52
	738	0.94	1.00
	904	0.71	0.80
	1117	~0.1	0.24
370	221	~0.0	0.50
	498	1.31	0.42
	577	0.62	0.0
	586	3.08	2.67
	675	0.66	-
	697	0.42	0.0
	738	1.39	2.50
	826	0.23	0.42

Table 3.5 continued

γ_i	γ_j	C_{ij} experimental	C_{ij} expected
	904	2.24	1.60
	1103	0.62	~0.5
	1120	0.95	0.05
	1324	2.00	2.17
412	198	3.77	4.80
	221	~0.3	~0.6
	466	~0.4	~0.4
	365	~0.2	~0.5
	498	2.40	2.26
	586	12.4	10.9
	697	5.37	5.44
	904	2.39	2.24
	1163	1.2	~0.6
	1173	1.2	0.40
438	221	0.68	1.00
+436	466	1.57	1.10
	498	0.30	~0.10
	586	1.43	0.75
	738	1.04	0.60
	837	1.39	1.10
	(962)	1.18	-
	1473	1.02	0.4
	1939	0.93	1.2
498	198	3.13	4.00
+499	221	4.28	4.00
	264	1.57	1.60
	345	0.4	~0.5
	370	0.0	0.4
	412	1.41	2.27
	438	0.54	0.10
	586	1.80	2.63
	711	0.96	0.25
	776	0.91	1.32
	827	3.17	3.01

Table 3.5 continued

γ_i	γ_j	C_{ij} experimental	C_{ij} expected	γ_i	γ_j	C_{ij} experimental	C_{ij} expected
	837	0.86	0.26		2021	1.10	1.60
	904	3.60	3.0		3142	3.70	5.90
	974	1.68	2.98	586	198	4.16	4.63
	1274	0.85	0.52		264	1.83	1.59
	1501	6.93	7.50		339	2.07	1.40
	1534	0.87	0.0		345	4.72	5.11
	1635	0.66	0.33		370	2.35	2.53
	1694	0.91	0.0		412	10.4	10.9
	1904	5.41	5.64		438	1.09	0.75
	2101	3.99	5.60		499	3.13	2.62
	3221	1.48	1.80		(675)	1.33	-
	3732	0.37	-		697	4.72	5.18
	763	~0.7	~0.2		738	18.8	18.9
577	904	0.73	0.83		763	2.20	1.20
	1117	4.03	2.80		837	2.80	1.53
	1422	1.61	1.30		867	0.63	1.18

Table 3.5 continued

γ_i	γ_j	C_{ij} experimental	C_{ij} expected	γ_i	γ_j	C_{ij} experimental	C_{ij} expected
	904	8.17	7.20	738	264	1.71	0.0
	947	1.94	2.3		370	2.08	2.5
	(962)	0.6	~0.4		586	20.5	18.9
	1108	15.6	13.3		837	0.88	0.91
	1117	~0.0	0.24		1274	1.95	3.27
	1173	0.9	0.83	763	221	2.02	2.05
	1236	2.84	2.70		345	1.74	1.90
	1274	2.68	3.10		356	0.0	0.4
	1412,1422	3.0	1.27		577	1.26	~0.2
	2012	8.65	9.00		586	1.77	1.20
697	221	1.81	2.3		711	1.17	1.83
	412	5.00	5.44		904	1.78	1.81
	586	4.22	5.18		932	0.84	0.85
	776	0.74	2.3		197	1.00	1.60
	904	1.65	2.39	867	586	1.06	1.18
	1778	0.76	0.0		(962)	2.18	~2
	221	0.0	1.0		1534	29.4	25.0

Table 3.5 continued

γ_i	γ_j	C_{ij} experimental	C_{ij} expected	γ_i	γ_j	C_{ij} experimental	C_{ij} expected
	197	1.5	1.5	974	221	5.70	6.40
904	221	14.8	11.5		499	3.34	2.98
	345	0.7	1.0		626	1.74	1.19
	356	0.45	1.65		904	2.39	2.37
	365	0.0	0.8	1117	221	1.50	2.74
+902	370	1.43	1.60	+1120	356	2.90	2.58
+(898)	412	1.83	2.24	+(1113)	365	1.21	0.24
	499	3.27	~3.0	+(1115)	438	0.56	0.10
	577	0.89	0.83		577	3.91	2.80
	586	8.0	7.20		586	0.47	0.24
	697	1.47	2.39		904	1.76	2.40
	763	1.0	2.37		1324	0.47	0.10
	974	1.60	1.81	1324	370	1.34	2.17
	1103,1108	6.21	4.54		(675)	1.87	-
	1117,1119	2.14	2.35		837	1.00	1.31
	1473	11.0	11.43		904	1.32	0.66
	1694	5.0	7.73		1274	1.36	2.65

which are typically those used in angular correlation experiments. Therefore, significant differences between the expected and observed C_{ij} may be created for cascades where anisotropies are large. Since corrections for these effects can only be applied if the spins of the levels involved and the multipole mixing in the coincidence cascades are known, it was not possible to adjust the predicted C_{ij}'s for this effect.

198 gate

This gating transition is composed of the ^{89}Kr doublet of 197.1 and 197.7 keV as well as a 196 keV line from ^{88}Kr. The peaks due to ^{88}Kr are labelled in figure 3.12(a). Most of the 1173 keV peak arises from the double escape of a 2195 keV transition in ^{88}Kr. The ^{88}Kr lines which appear here and in subsequent spectra have intensities consistent with predictions from a recent study of H. Lycklama and T.J. Kennett (1970). The 867 and part of the 707 keV peaks arise from the 197.1 keV component in the gate. The remaining lines are connected with the 197.7 keV component. The two "peaks" to the right of the 511 keV peak have been generated by the subtraction process since a check of the unsubtracted data revealed no peaks at those positions.

221 gate

The spectrum associated with the 221 keV gate, presented in the lower part of figure 3.12(a), conveys most of the information on which the final decay scheme has been constructed. This spectrum can be interpreted by means of the partial decay scheme. The deduced values of C_{ij}'s are again reproduced in table 3.5. A number of the weak peaks in this spectrum appear only in coincidence work. Because these peaks are very weak, it has been decided not to use them to define new levels.

264 gate

In addition to the peaks expected from the partial decay scheme, there appear to be weak peaks at 438 and 1501 keV which have not been explained. They may be spurious peaks arising from background subtraction.

345 gate

The 345 keV transition in this gate is believed to deexcite the 931.5 keV level. There is also evidence for a level at 930.7 keV based on the fact that, with the exception of the 264 and 345 keV gamma rays, all of the transitions feeding or deexciting this pair of states are close doublets. Thus the 264 and 345 keV gates select certain components of these doublets. There is no direct coincidence evidence for the 930.7 keV state except for the fact that the C_{ij}'s associated with the 711 and 930 keV peaks in the 264 keV gate are too small to accomodate all the intensity of these two doublets. The remainder of the peaks observed in this gate have probabilities consistent with the partial decay scheme of figure 3.12(b).

356 gate

The gating transition involved here is actually composed of two lines: one at 354.1 keV and the other at 356.5 keV. These gamma rays have been assigned the positions indicated in the partial decay scheme. The coincidence probabilities agree within experimental errors, except for the 763 keV peak which is almost three times as intense as forecast (see table 3.5). There are a number of other difficulties of this sort involving the 931-932 keV states. The statistics in these results are too poor to enable one to resolve them.

365 gate

Although the gate includes 100% of the 365.3 keV peak, ~10% of the 356.5 keV peak, and ~60% of the 369.7 keV peak, the 365 keV component is the only one which can give rise to a significant number of coincidence events with the exception of the 221 keV transition. The very strong 1248-1031 keV cascade from ^{89}Sr is responsible for the weak 1248 and 1031 keV peaks in this and a number of other gates.

370 gate

The 577 and 1120 keV peaks in the 370 keV gated spectrum are not expected to appear if their assigned positions in the decay scheme are correct. Because the evidence for both of these peaks rests on one high point, they may both have been created by the subtraction process. The weak presence of the 831 keV transition from ^{90}Rb decay is not too surprising since this gamma ray has been observed as the most intense line in ^{90}Sr (Mason et al. 1970). The agreement between experimental and projected C_{ij} values for the remaining peaks is good.

412 gate

The observed and excepted coincidence probabilities compare favorably in this gate. In addition to the gating transition of 412 keV there is a contamination component in the form of a 408 keV peak from ^{138}Cs. This accounts for the 463 and 1436 keV ^{138}Cs peaks which appear with the expected intensity ratios (Carraz et al. (1971)).

438 gate

The above gate contains all of the 438.1 and ~25% of the 435.8 keV gamma ray peaks. The latter is too weak to produce measurable coincidences. The peaks observed are all consistent with the proposed decay scheme. The reality of the 962 keV peak is very doubtful and should not have appeared if its assignment given in the decay scheme is correct.

498 gate

The 498 gate includes two rather strong gamma rays of energies 498.6 and 497.7 keV. The agreement with the proposed decay scheme is excellent except for the 1534 and 1694 keV peaks. The former may arise from poor background subtraction since there is a strong ^{89}Rb line at this energy. The latter may also have been created by the subtraction process.

577 gate

This gate contains the 577 keV photopeak plus a small contribution (~2%) from the very strong 586 keV line. the 738 and 1108 keV peaks arise from the 586 keV component. The remaining peaks have the expected intensities.

586 gate

Involved here is the strong 586 keV transition which deexcites the 586 keV state and provides evidence for a large number of transitions to this level. The 1374 keV peak strongly suggests that this transition belongs in ^{89}Kr and defines a level at 1960 keV. However, no confirmation of this level either through coincidence evidence or by the placement by energy sums of other transitions involving the 1960 keV level can be made. Hence it has not been included in the final decay scheme. The peak at 1374 keV in the singles work is largely due to ^{90}Rb and there also seems to be a long lived component at this energy. The 1422 keV peak is also not explained. If it is real, it indicates that the 1422 keV line in table 3.5 is double.

697 gate

The 697 keV gate is clean and brings up all the transitions deexciting the 998 keV level. The 776/412 keV intensity ratio is a factor of two smaller than one would expect, but the statistics on the former peak are poor. If the peaks at 1148 and 1778 keV are real, they are evidence of a second gamma ray of energy ∿697 keV in the gate which must lie higher up in the decay scheme.

738 and 867 gates

The 738 and 867 keV gates show all the peaks as expected and require no further comment.

763 gate

With the exception of the 577 keV peak, there are no surprises in this spectrum. The 577 keV peak appears to be much too strong. It has not been possible to resolve this difficulty.

904 gate

In addition to the strong 904.5 keV transition, this gate contains the weak 902.8 and ~30% of the 897.0 keV peaks. The latter two transitions do not appear to have created any coincidences and have not been placed in the decay scheme.

974 gate

The 974 keV gamma ray deexcites the 1195 keV level and its coincidence spectrum provides evidence for a 974-221 keV cascade.

1117 gate

This wide gate includes four gamma rays at 1112.6, 1115.0, 1116.6 and 1119.6 keV. Most of the observed coincidences are due to the strong 1116.6 keV transition. The 1115 and 1120 keV photons are both weak and have been placed only through energy sums. The weak 1113 keV line has not been classified. The spectrum gives reasonable support to the partial decay scheme shown. The calculated C_{ij} values of table 3.5 are based on the 1117 keV transition above. The 365 keV peak is too strong and appears as if it might be complex.

1324 gate

This gate shows the gamma rays feeding the 1325 keV level. The very weak peak at 675 is not explained.

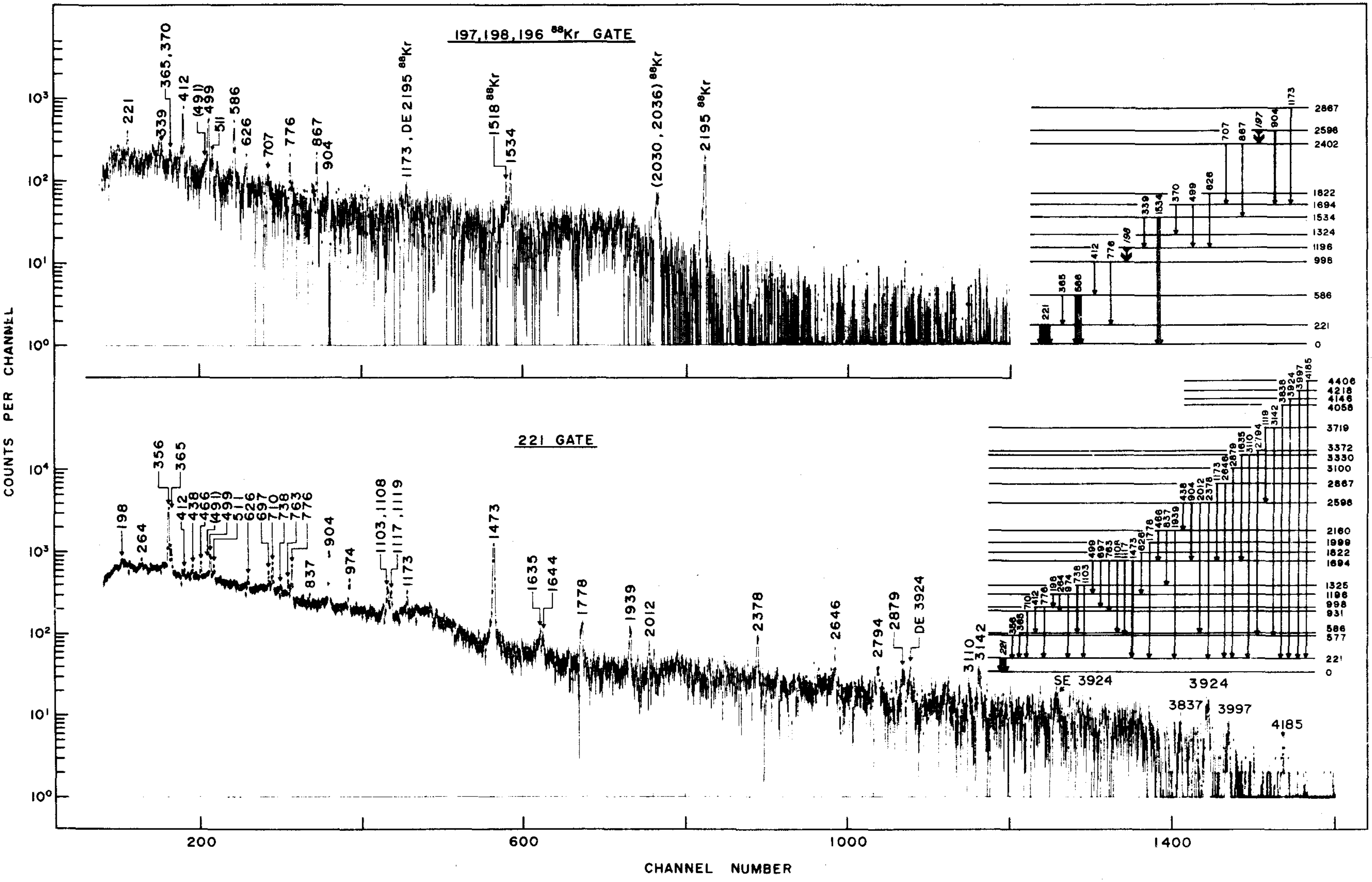

Figure 3.12(a) Coincidence data associated with the 1196-998, 2598-2402 keV levels and 221 keV level .

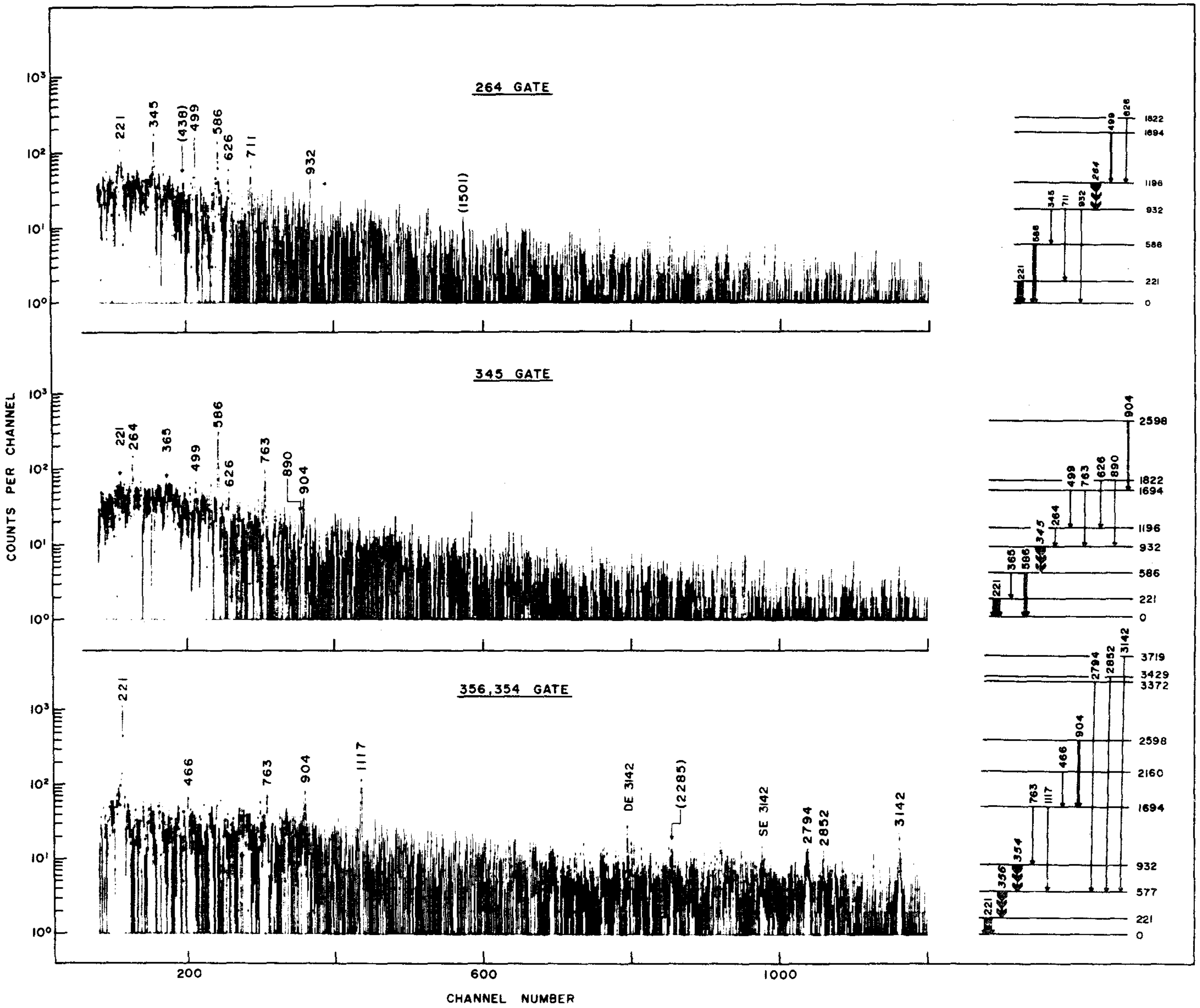

Figure 3.12(b) Coincidence data associated with the 1196-932, 932-586, and 932-577-221 keV levels.

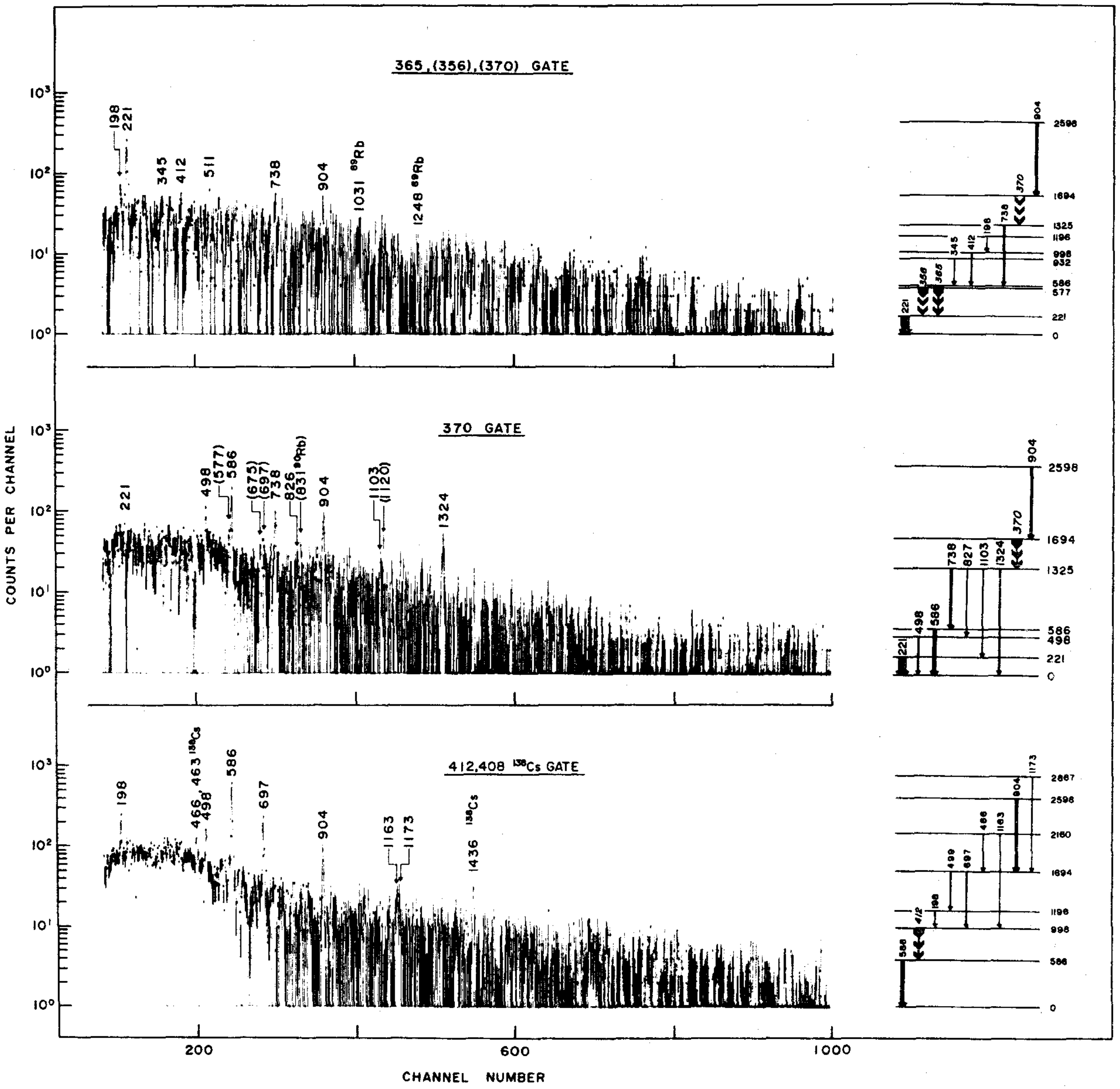

Figure 3.12(c) Coincidence data associated with the 586-221, 577-221, 1694-1325, and 998-586 keV levels.

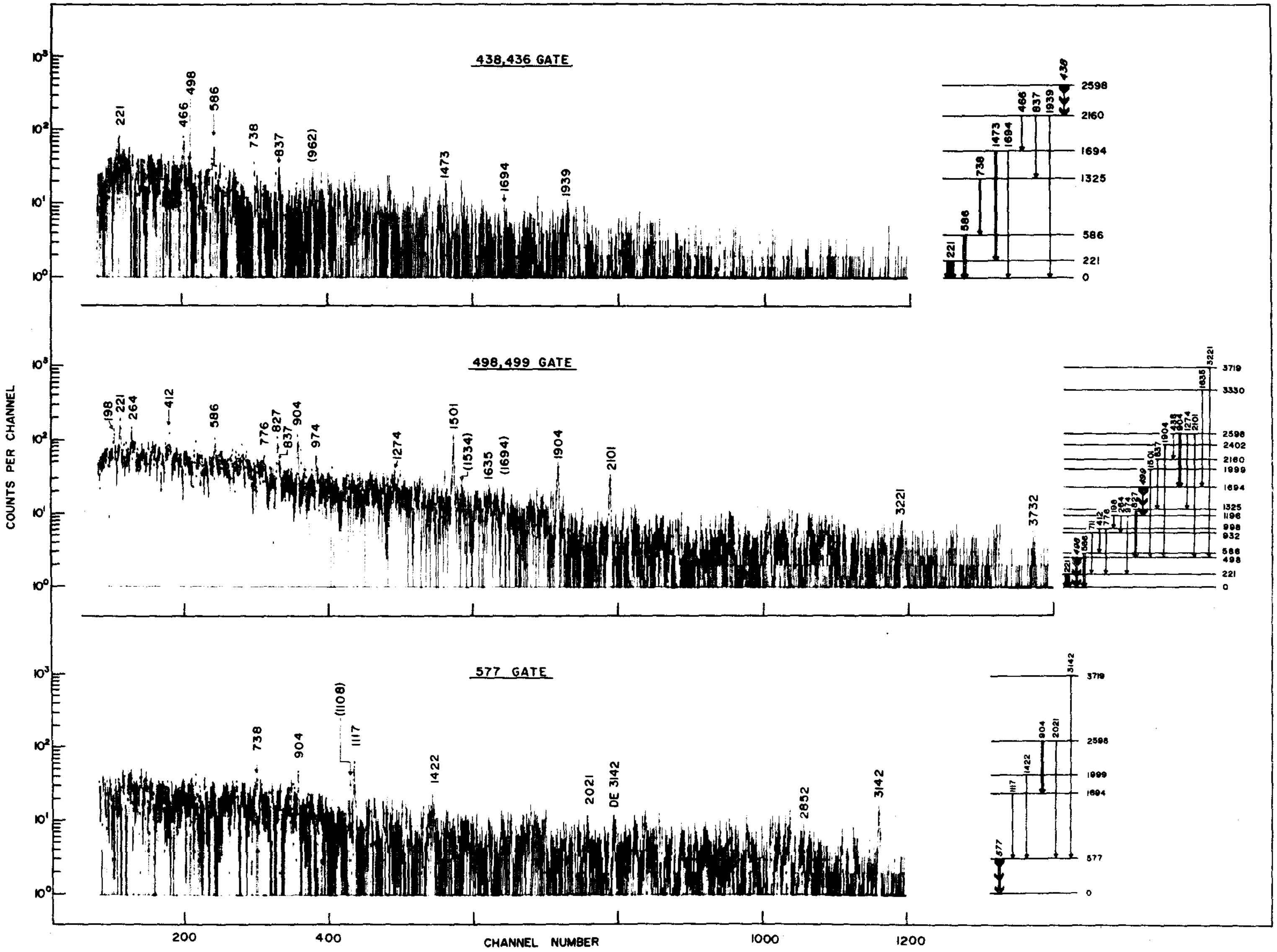

Figure 3.12(d) Coincidence data associated with the 2598-2160, 1694-1324, 498 and 577 keV levels.

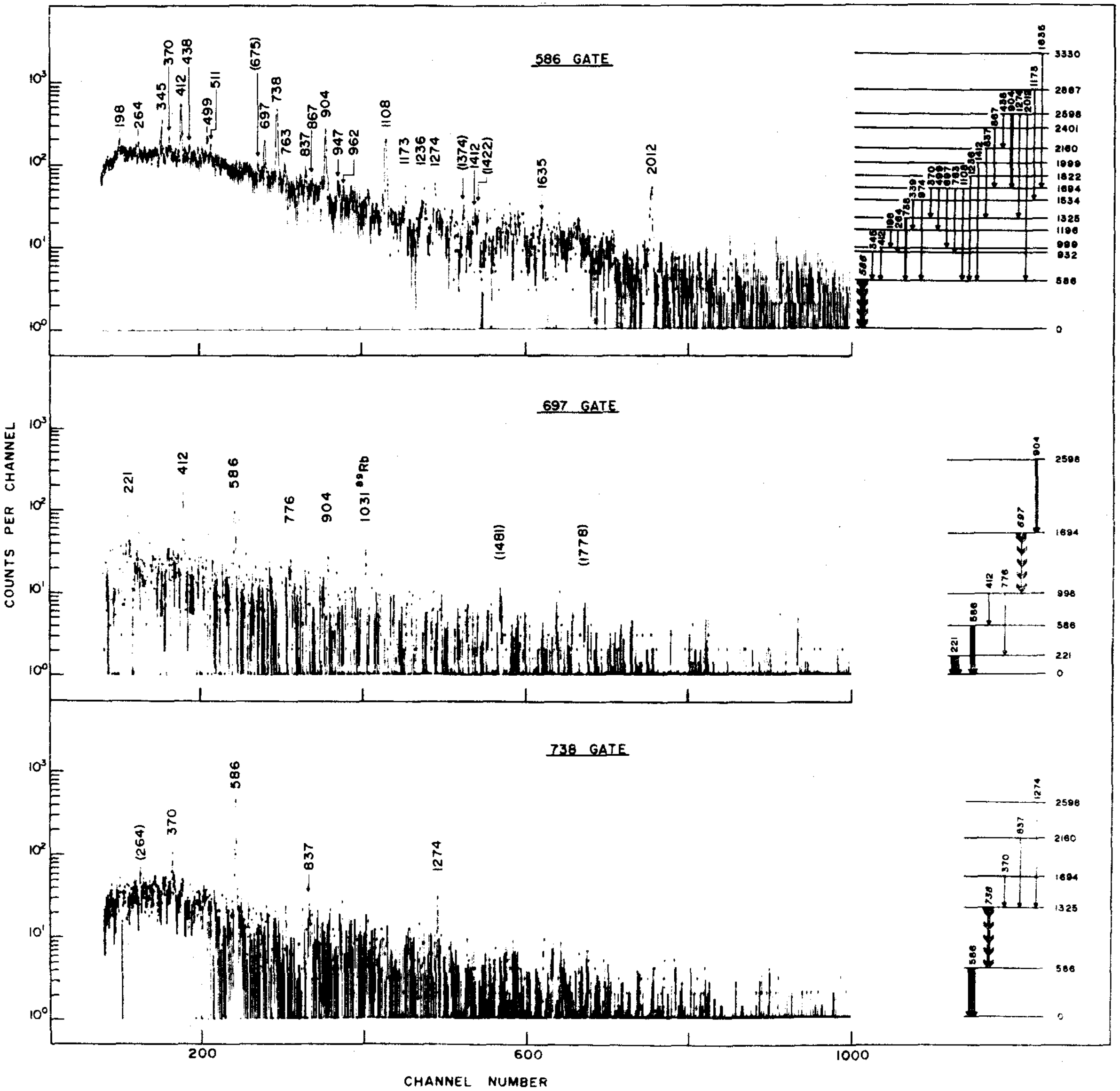

Figure 3.12(e) Coincidence data associated with the 586, 1694-998, and 1325-586 keV levels.

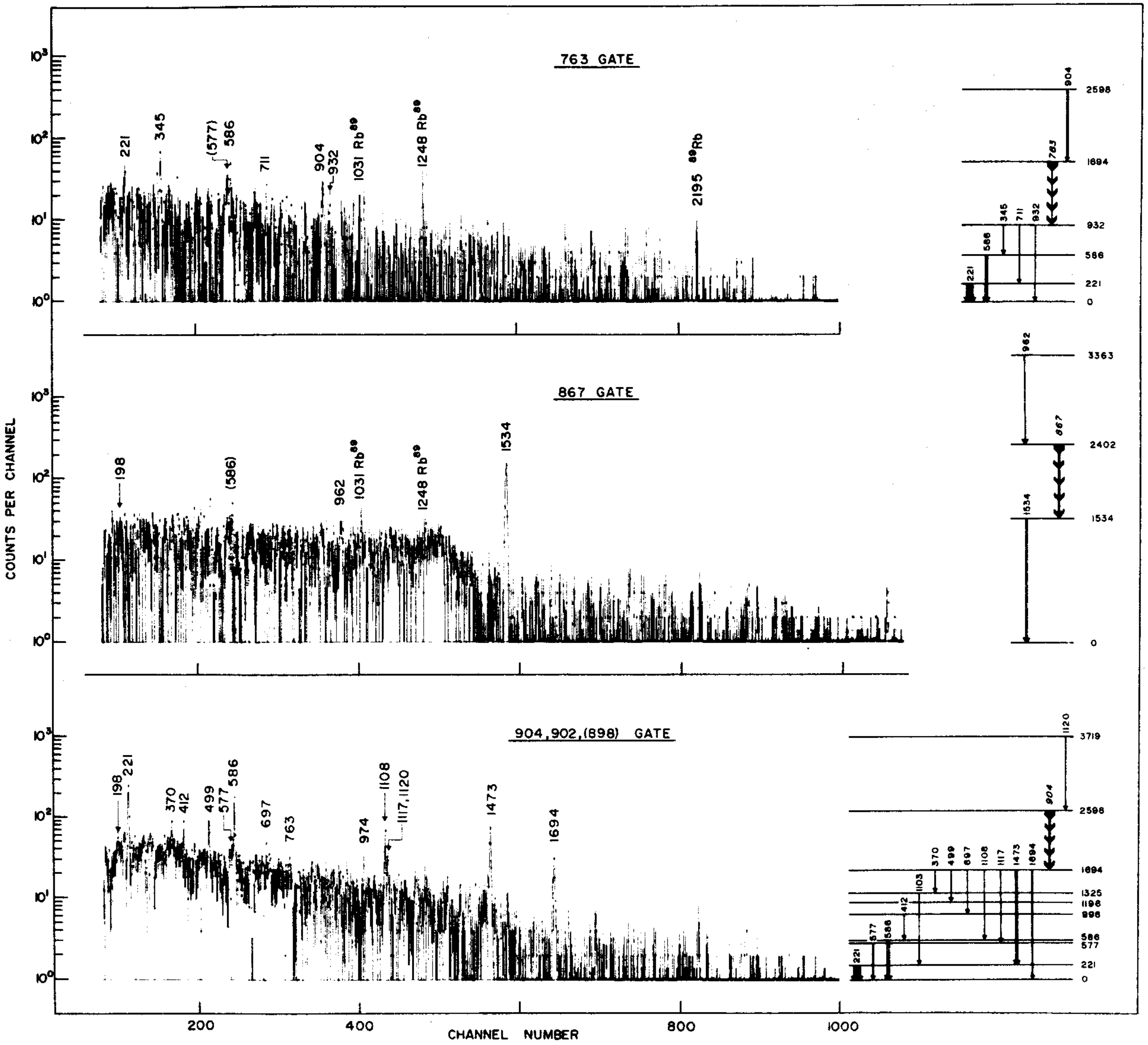

Figure 3.12(f) Coincidence data associated with the 1694-932, 2402-1534, and 2598-1694 keV levels.

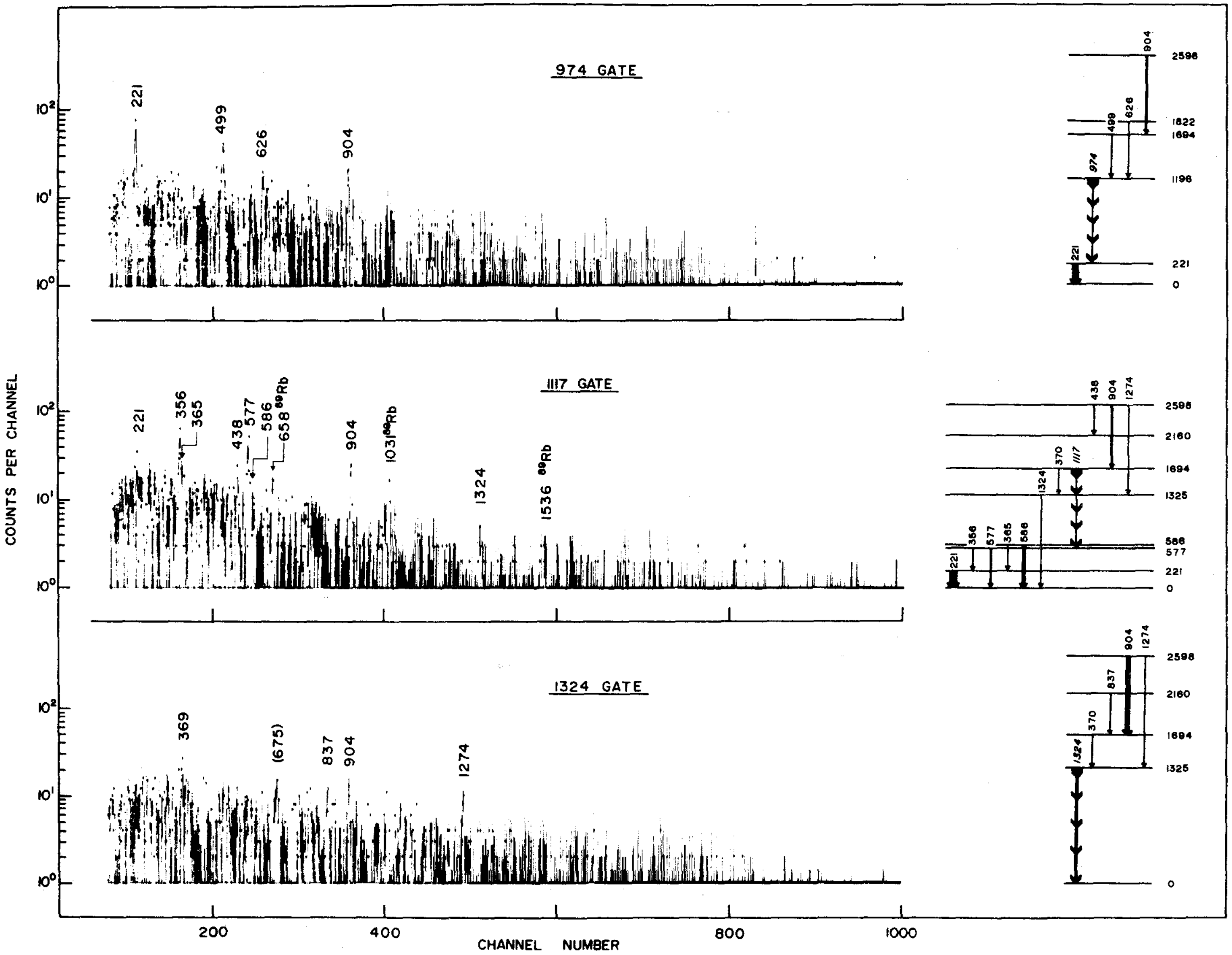

Figure 3.12(g) Coincidence data associated with the 1196-221, 1694-577, and 1325 keV levels.

3.4 The Level Structure of ^{89}Rb

The results of the experiments described in the previous sections are summarized in the decay scheme presented in figure 3.13(a) and (b), and tabulated in tables 3.6 through 3.8. The gamma intensities shown on this figure and listed in tables 3.3 and 3.7 are relative values normalized to 100 for the 221 keV line intensity. The strength of beta feeds has been deduced from the gamma ray intensity imbalance at each level shown in table 3.8 which also presents the beta decay intensities together with the associated log ft values. A comparison between these and the values obtained by Kitching *et al*. is also made.

In order to simplify the discussion of this complex decay scheme, each level will be treated in turn below.

The 221, 498, 577 and 586 keV levels

It is evident from figure 3.12(a), (d) and (e) that the coincidence spectra generated by gates at the above energies show a large number of high energy photons. This information, coupled with the fact that none of these four gamma rays is in coincidence with each other indicates that these levels are the first four excited states of ^{89}Rb. Moreover, these four gamma rays are among the most intense in the spectrum of ^{89}Kr. This is substantiated by the coincidence spectra of the 221, 356 and 365 gates of figure

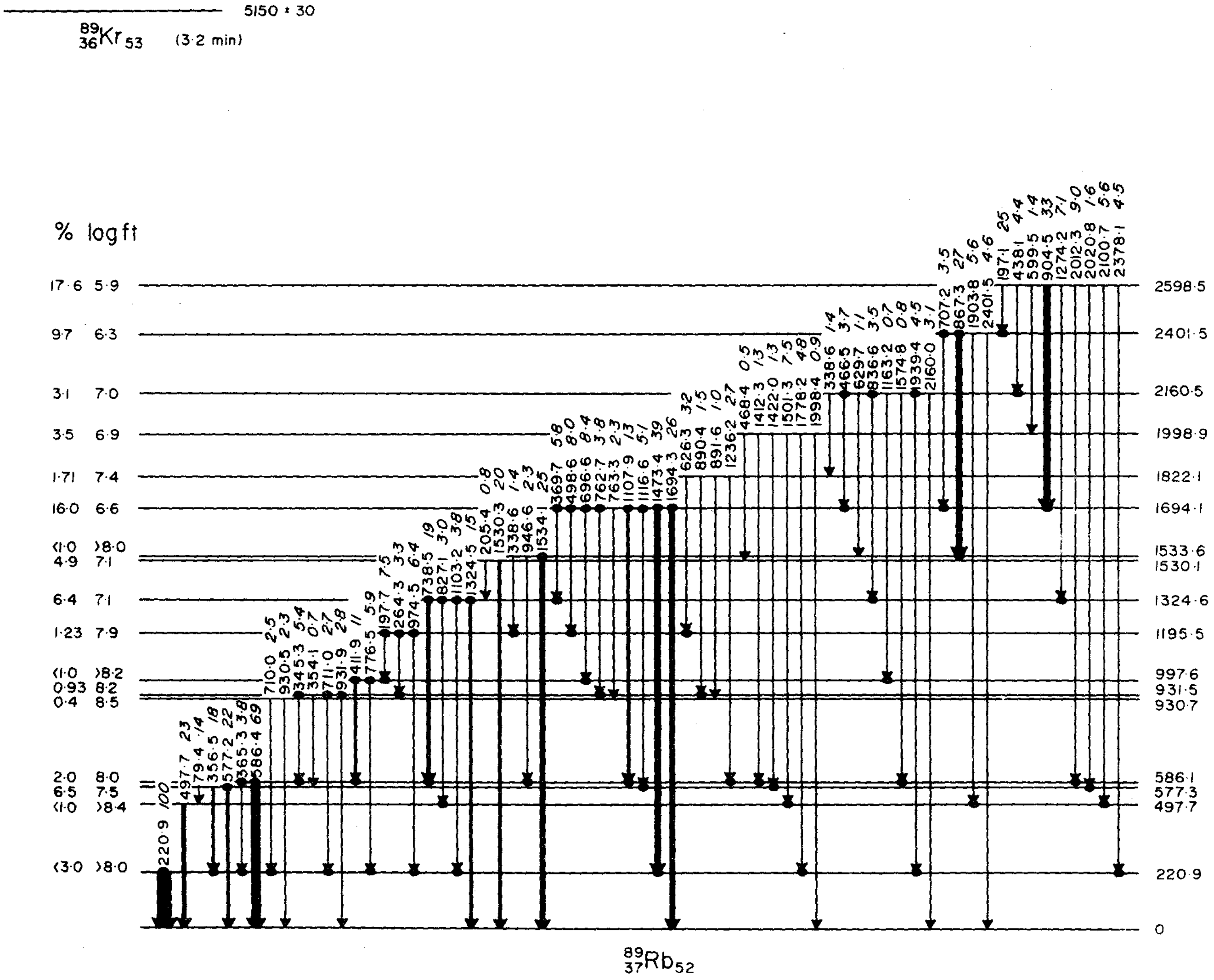

Figure 3.13(a) The low-lying level structure of ^{89}Rb.

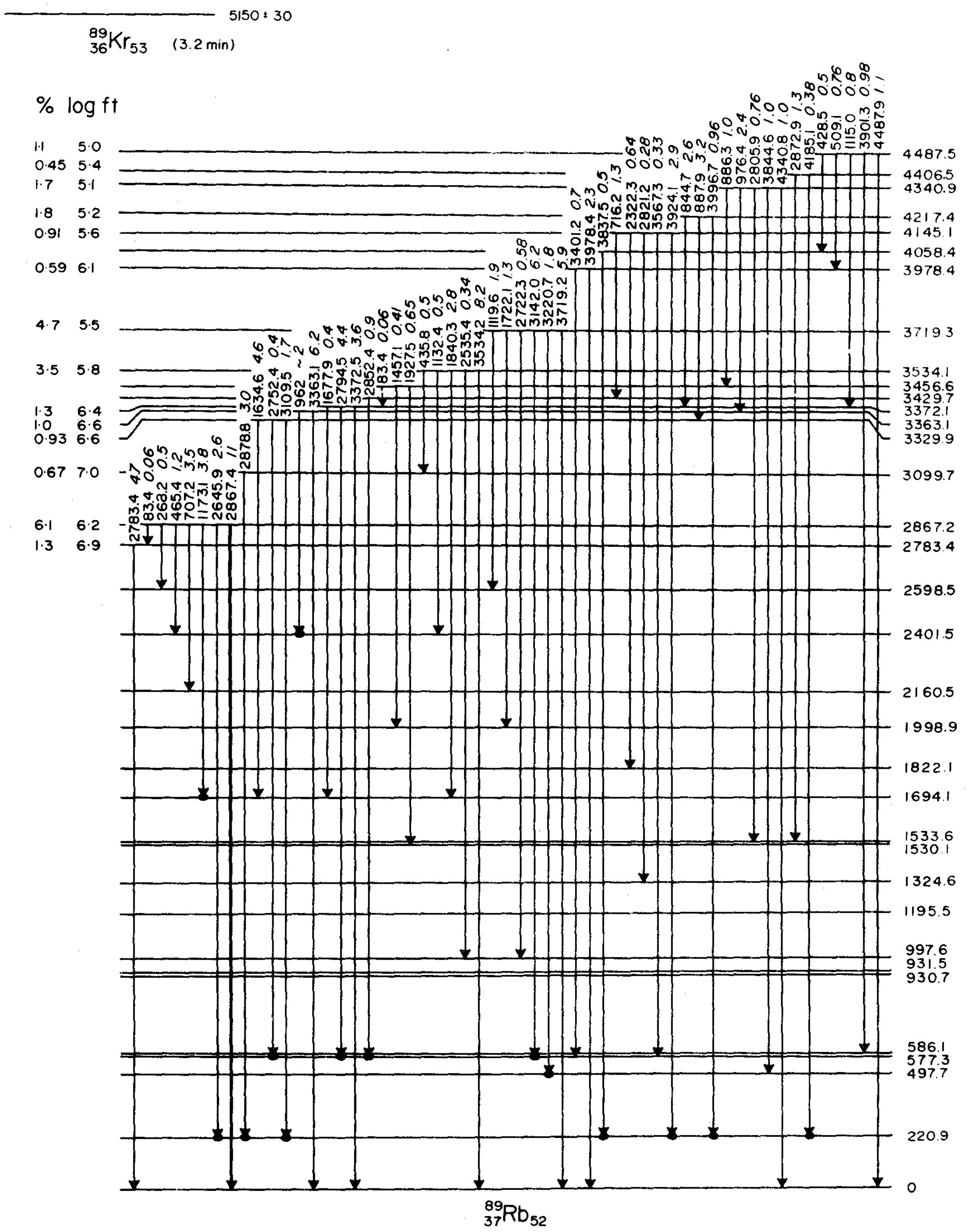

Figure 3.13(b) The high-lying level structure of ^{89}Rb.

3.12(a), (b) and (c). Since these form states that are well established they will be used to provide a secure base for the determination of higher-lying excited states.

The 931,932 keV levels

The level at 932 keV is proposed from the 711-221 and 345-586 keV cascades and their involvement in the 221, 345 and 586 keV gates. However, it is difficult to provide direct coincidence evidence for the 931 keV level since the 710 and 711 keV doublet cannot be resolved in the coincidence spectrum obtained with the gate at 221 keV. This level, together with the 932 keV level is supported by four doublets observed in the singles spectrum. They are, incoming--890-892, 762-763, and outgoing--931-932, 710-711 keV.

The 998 and 1196 keV levels

The presence of these levels is built on the following cascades. The 412-586 and 776-221 keV cascades are established from the information contained in the 221, 412, and 586 gates. Similarly, cascades of 198-412-586 and 974-221 keV have been observed mainly in the 198, 221, 412 and 586 gates. The experimental coincidence probabilities for all these cases are in good agreement with the expected values.

The 1325, 1534 and 1694 keV levels

These three levels are characterized by the following strong cascades: 738-586, 867-1534, 1473-221 keV respectively. A large number of other transitions deexciting the 1324 and 1694 keV levels are also seen in coincidence as shown by the closed circles in the decay scheme of figure 3.13(a). All three levels decay strongly to the ground state of ^{89}Rb. The β-γ coincidence data of Kitching and Johns point out significant direct beta feed to the level at 1324 keV.

The 1530 keV level

The previous work has indicated (from a gate set on their 1533 keV line) that substantial beta branching to a level at this energy occurs. In their singles gamma spectra, the 1530 and 1534 keV gamma rays were not resolved so that they assigned all the beta feed involved to the 1533 keV level. The gamma ray singles of this investigation (figure 3.4) clearly shows the presence of two strong lines at 1530 and 1534 keV. A portion of the intensity (~8%) of the 1530 keV line can be attributed to ^{88}Kr present as a contamination line in the source material. Almost 90% intensity of the 1534 keV line is assigned to the decay of ^{89}Kr. Since the γ-γ coincidence experiment, with a gate set on the 867 keV gamma ray, unambiguously defines an 867-1534 keV cascade, it may be concluded that the 1530 keV level is almost entirely populated directly by beta rays. Interestingly enough, the beta feed observed here is 4.9% for this level which agrees well with the value obtained by Kitching and Johns; however, there is no direct evidence for this level from the γ-γ coincidence datum although it does indicate that the strong 1530 keV transition does not feed any of the known levels up to 1694 keV and therefore, this transition must be presumed to feed the ground state.

The 1822 keV level

This level is involved in six gates and is strongly supported by the 1236-586, 626-198, and 626-974 keV cascades.

The 1999, 2160, 2401 and 2598 keV levels

This set of levels remains unchanged from the study by Kitching *et al*. Their presence has been confirmed in this work via the well-established cascades of 1501-498, 1939-221, 867-1534 and 904-1694 keV.

The 2783, 3534 and 3978 keV levels

Although gamma rays of these energies have been observed to have strong singles intensities, they are missing in the γ-γ coincidence spectra as evidenced by the coincidence projection spectrum of figure 3.11 where the intensities of these lines are marginal. This strongly suggests that these gamma rays are all ground state transitions. The 3534 and 3978 keV levels are also supported by weak line energy sums. The 2783 keV state must be regarded as tentative.

The 2867, 3363, 3372 and 3719 keV levels

The existence of these levels is based on gates set on the 867, 356 and 221 keV transitions. These gates reveal the 2646-221, 962-867, 2794-356 and 3142-356 keV cascades. In addition, there are a number of supporting energy sums as well as the fact that all of these levels are deexcited by fairly strong ground state transitions which show no γ-γ coincidences.

The 3100, 3330, 4058, 4145, 4218 and 4406 keV levels

These levels are defined by 2878, 3109, 3838, 3924, 3997 and 4185 keV coincidences in the 221 keV gate. Although there are other gamma rays deexciting these levels (their positions being based on energy sums), they are too weak to be observed in the coincidence spectra.

The 3429 keV level

This level is postulated on the basis of a 2852 keV peak in both the 577 and 356 keV gates, and one energy sum.

The 3456, 4341 and 4488 keV levels

Tentative suggestions as to the creation of these

TABLE 3.6

Adopted Level Energies from Gamma Ray Energy Sums

Feeding Transition	Level Involved	Sum	Adopted Level Energy (keV)
220.9	0	220.9	220.9±0.2
497.7	0	497.7	497.7±0.2
577.2	0	577.2	577.3±0.2
356.5	220.9	577.4	
79.4	497.7	577.1	
586.0	0	586.0	586.1±0.2
365.3	220.9	586.2	
930.5	0	930.5	930.7±0.4
710.0	220.9	930.9	
931.5	0	931.5	931.5±0.4
711.0	220.9	931.9	
354.1	577.3	931.4	
345.3	586.1	931.4	
776.5	220.9	997.4	997.6 0.3
411.9	586.1	998.0	
974.5	220.9	1195.4	1195.5±0.3
264.3	931.5	1195.8	
197.1	997.6	1195.3	
1324.5	0	1324.5	1324.6±0.4
1103.2	220.9	1324.1	
827.1	497.7	1324.8	
738.5	586.1	1324.6	
1530.0	0	1530.0	1530.1±0.2
205.4	1324.6	1530.0	
599.5	930.7	1530.2	
1534.1	0	1534.1	1533.6±0.2
946.6	586.1	1532.7	
338.6	1195.5	1534.1	

(continued next page)

Table 3.6 (continued)

Feeding Transition	Level Involved	Sum	Adopted Level Energy (keV)	Feeding Transition	Level Involved	Sum	Adopted Level Energy (keV)
1694.3	0	1694.3	1694.2±0.3	1998.4	0	1998.4	1998.9±0.5
1473.4	220.9	1694.3		1778.2	220.9	1999.1	
1116.6	577.3	1693.9		1501.3	497.7	1999.0	
1107.9	586.1	1694.0		1422.0	577.3	1999.3	
763.3	930.7	1694.0		1412.3	586.1	1998.4	
762.7	931.5	1694.2		486.4	1530.1	1998.5	
696.6	997.6	1694.2		2160.0	0	2160.0	2160.5±0.7
498.6	1195.5	1694.1		1939.4	220.9	2160.3	
369.7	1324.6	1694.3		1574.8	586.1	2160.9	
1236.2	586.1	1822.3	1822.1±0.3	1229.6	930.7	2160.3	
891.6	930.7	1822.3		1163.2	997.6	2160.8	
890.4	931.5	1821.9		836.6	1324.6	2161.2	
626.3	1195.5	1821.8		629.7	1530.1	2159.8	
				466.5	1694.2	2160.7	
				338.6	1822.1	2160.7	

(continued next page)

Table 3.6 (continued)

Feeding Transition	Level Involved	Sum	Adopted Level Energy (keV)	Feeding Transition	Level Involved	Sum	Adopted Level Energy (keV)
2401.5	0	2401.5	2401.5±0.2	2867.4	0	2867.4	2866.9±0.5
1903.8	497.7	2401.5		2280.9	586.1	2867.0	
867.3	1533.6	2400.9		1173.1	1694.2	2867.3	
707.2	1694.2	2401.4		465.4	2401.5	2866.9	
2598.3	0	2598.3	2598.5±0.6	268.2	2598.5	2866.7	
2378.1	220.9	2599.0		2878.8	220.9	3099.7	3099.7±0.8
2100.7	497.1	2598.4		3109.5	220.9	3330.4	3329.9±1.0
2020.8	577.1	2597.9		2752.4	577.3	3329.7	
2012.3	586.1	2598.4		1634.6	1694.2	3328.8	
1274.2	1324.6	2598.8		3363.1	0	3363.1	3363.1±0.5
904.5	1694.2	2598.7		962	2401.5	3363.5	
599.5	1998.9	2598.4		3372.5	0	3372.5	3372.1±0.4
438.1	2160.5	2598.6		2794.5	577.3	3371.8	
197.1	2401.5	2598.6		1677.9	1694.2	3372.1	
2783.4	0	2783.4	2783.4±0.7	2852.4	577.3	3429.7	3429.7±0.8

(continued next page)

Table 3.6 (continued)

Feeding Transition	Level Involved	Sum	Adopted Level Energy (keV)
1927.5	1530.1	3457.6	3456.6±1.0
1457.1	1998.9	3456.0	
3534.2	0	3534.2	3534.1±1.0
2535.4	997.6	3533.0	
1840.3	1694.2	3534.5	
1132.4	2401.5	3533.9	
435.8	3099.7	3535.5	
3719.2	0	3719.2	3719.3±1.3
3220.7	497.7	3718.4	
3142.0	577.3	3719.3	
2722.3	997.6	3719.9	
1722.1	1998.9	3721.0	
1119.6	2598.5	3718.1	
3978.4	0	3978.4	3978.4±018
3401.2	577.3	3978.5	
3837.5	220.9	4058.4	4058.4±1.0
3924.1	220.9	4145.0	4145.1±1.0
3567.3	577.3	4145.0	
2821.2	1324.6	4145.8	
2322.3	1822.1	4144.4	
427.5	3719.3	4146.8	
3996.7	220.9	4217.6	4217.4±1.0
887.9	3329.9	4217.8	
844.7	3372.1	4216.8	
4340.8	0	4340.8	4340.9±1.5
3844.6	997.7	4342.3	
2805.9	1533.6	4339.5	
976.4	3363.1	4339.5	
886.3	3456.6	4342.9	
4185.1	220.9	4406.0	4406.5±1.0
2872.9	1533.6	4406.5	

(continued next page)

Table 3.6 (continued)

Feeding Transition	Level Involved	Sum	Adopted Level Energy (keV)
4487.9	0	4487.9	4487.5±1.5
3901.3	586.1	4487.4	
3161.5	1324.1	4486.1	
1115.0	3372.1	4487.1	
509.1	3978.4	4487.5	
428.5	4058.4	4486.9	

high lying levels are made on the basis of several gamma ray energies summing to these three values.

As a general review, it may be mentioned that the decay scheme is comprised of 34 levels whose energies have been deduced from gamma ray energy sums as shown in table 3.6. Out of 120 gamma transitions associated with these levels, 65 have been assigned from coincidence evidence and the remaining 55 on the basis of energy differences between levels. About 40 weak transitions have not been incorporated into the present scheme. Table 3.7 lists the observed gamma rays in the ^{89}Kr decay together with their relative intensities. The classification of assigned transitions in the decay scheme of figure 3.13 is shown in the third column. The fourth column indicates the main method used to place the particular gamma ray, that is, coincidence evidence (γ-γ) or energy sum (E) based on singles work. The final column tabulates the difference between the energies predicted from the decay scheme (E_{cal}) and those measured (E_{obs}). In reference to the Kitching and Johns work, 19 levels have been found to coincide while 15 levels are new additions. No evidence, in this study, exists either from the singles spectra or from the coincidence data regarding the existence of the remaining 14 levels at 1760, 2618, 3732, 3905, 4080, 4138, 4184, 4228, 4368, 4481, 4626, 4649 and 4690 keV proposed by Kitching *et al*. In

TABLE 3.7

Transitions in ^{89}Rb Following the Decay of ^{89}Kr

E_γ (keV)	I_γ	Classification	Basis for Classification	$E_{cal}-E_{obs}$ (keV)
74.9±0.5	0.06±0.02			
76.0±0.6	0.04±0.02			
79.4±0.5	0.14±0.02	577→498	E	+0.2
83.4±0.6	0.06±0.02	2867→2783 or	E	+0.1
		3456→3372	E	+0.6
197.1±0.3	2.5 ±0.5	2598→2402	γ-γ	+0.4
197.7±0.3	7.5 ±1.5	1196→998	γ-γ	+0.2
205.4±0.5	0.80±0.20	1530→1325	E	+0.1
220.9±0.2	100	221→0	γ-γ	0.0
264.3±0.4	3.3 ±0.6	1196→932	γ-γ	-0.3
267.2±0.5	0.21±0.05			
268.2±0.5	0.48±0.12	2867→2598	E	+0.2
338.6±0.4	1.4 ±0.2	1534→1196	γ-γ	-0.5
345.3±0.2	5.4 ±0.7	932→586	γ-γ	+0.1
354.1±0.4	0.67±0.15	932→577	γ-γ	+0.1
356.5±0.2	17.8 ±1.8	577→221	γ-γ	-0.1
365.3±0.2	3.8 ±0.5	586→221	γ-γ	-0.1
369.7±0.2	5.8 ±0.8	1694→1325	γ-γ	-0.1
411.9±0.2	10.9 ±1.1	998→586	γ-γ	-0.4
428.5±0.4	0.54±0.13	4487→4058	E	+0.1

Table 3.7 continued

E_γ (keV)	I_γ	Classification	Basis for Classification	$E_{cal}-E_{obs}$ (keV)
435.8±0.6	0.48±0.12	3534→3100	E	-1.4
438.1±0.4	4.4 ±0.6	2598→2160	γ-γ	-0.1
465.4±0.5	1.2 ±0.2	2867→2902	E	+0.5
466.5±0.4	3.7 ±0.6	2160→1694	γ-γ	-0.2
468.4±0.6	0.48±0.12	1999→1530	E	+0.4
491.4±0.5	1.0 ±0.2			
497.7±0.2	22.7 ±2.3	498→0	γ-γ	0.0
498.6±0.2	8.0 ±1.0	1694→1196	γ-γ	+0.1
509.1±0.5	0.76±0.20	4488→3978	E	0.0
510.1±0.5	0.60±0.20			
577.2±0.2	21.8 ±2.2	577→0	γ-γ	+0.1
586.4±0.2	69 ±7	586→0	γ-γ	-0.3
599.5±0.4	1.4 ±0.2	2598→1999	E	+0.1
626.3±0.3	3.2 ±0.5	1822→1196	γ-γ	+0.3
629.7±0.5	1.7 ±0.4	2160→1530	E	+0.7
696.6±0.5	8.4 ±1.0	1694→998	γ-γ	0.0
707.2±0.5	3.5 ±0.5	2401→1694	γ-γ	-0.3
710.0±0.5	2.5 ±0.5	931→221	E	-0.2
711.0±0.5	2.7 ±0.5	932→221	γ-γ	-0.4
716.2±0.5	1.3 ±0.3	4145→3429	E	-0.4
738.5±0.2	18.9 ±2.0	1325→586	γ-γ	0.0

Table 3.7 continued

E_γ(keV)	I_γ	Classification	Basis for Classification	$E_{cal}-E_{obs}$ (keV)
762.7±0.5	3.8 ±0.5	1694→932	γ-γ	0.0
763.3±0.5	2.3 ±0.5	1694→931	E	-0.6
776.5±0.5	5.9 ±0.7	998→221	γ-γ	+0.2
827.1±0.5	3.0 ±0.6	1325→498	γ-γ	+0.2
834.4±0.6	3.6 ±0.7			
836.6±0.6	3.5 ±0.6	2160→1325	γ-γ	-0.7
844.7±0.6	2.6 ±0.5	42.8→3372	E	
867.3±0.2	26.7 ±2.7	2402→1534	γ-γ	+0.2
886.3±1.0	1.0 ±0.5	4341→3456	E	-1.4
887.9±0.6	3.2 ±0.6	4218→3330	E	-0.2
890.4±1.0	1.5 ±0.5	1822→931	E	+0.2
891.6±1.0	1.0 ±0.5	1822→932	E	-0.2
895.3±1.0	1.5 ±0.5			
897.0±0.6	2.4 ±0.5			
902.8±0.6	4.0 ±0.7			
904.5±0.2	33 ±3	2598→1694	γ-γ	-0.2
930.5±0.6	2.3 ±0.5	931→0	E	+0.2
931.9±0.6	2.8 ±0.5	932→0	γ-γ	-0.4
946.6±0.6	2.3 ±0.5	1534→586	γ-γ	+0.9
962 ±2	2.3 ±0.9*		γ-γ	~0
974.5±0.6	6.4 ±1.0	1196→221	γ-γ	+0.1
976.4±0.6	2.4 ±0.4	4341→3363	E	+1.5

Table 3.7 continued

E (keV)	I	Classification	Basis for Classification	$E_{cal}-E_{obs}$ (keV)
999.4±0.7	3.4 ±0.6			
1038.5±0.8	1.6 ±0.4			
1103.2±0.6	3.8 ±0.6	1325→221	γ-γ, E	+0.5
1107.9±0.5	13.3 ±1.5	1694→586	γ-γ, E	+0.2
1112.6±0.8	1.7 ±0.4			
1115.0±0.8	0.8 ±0.3	4488→3372	E	0.0
1116.6±0.5	5.1 ±0.7	1674→577	γ-γ, E	+0.3
1119.6±0.7	1.9 ±0.5	37.9→2598	γ-γ, E	+0.9
1132.4±1.0	0.5 ±0.2	3534→2402	E	+0.5
1163.2±1.0	0.66±0.2	2160→998	γ-γ	-0.3
1173.1±0.6	3.8 ±0.5	2867→1694	γ-γ	-0.4
1185.6±0.8	0.91±0.3			
1236.2±0.7	2.7 ±0.4	1822→586	γ-γ	-0.2
1274.2±0.5	7.1 ±0.8	2598→1325	γ-γ	-0.3
1324.5±0.5	15.4 ±1.5	1325→0	γ-γ, E	+0.1
1365.9±1.5	0.74±0.2			
1374 ±1.0	1.0 ±0.5	(1960→536)†		
1412.3±0.8	1.27±0.3	1999→586	γ-γ	+0.5
1422.0±0.8	1.30±0.3	1999→577	γ-γ	-0.4
1457.1±1.0	0.41±0.12	3456→1999	E	0.0
1473.4±0.4	38.6 ±3.0	1694→221	γ-γ	-0.1

Table 3.7 continued

E_γ(keV)	I_γ	Classification	Basis for Classification	$E_{cal}-E_{obs}$ (keV)
1481.5±0.8	0.69±0.2			
1501.3±0.5	7.5 ±0.8	1999→498	γ-γ	-0.1
1530.4±1.0	20 ±3	1530→0	E	-0.2
1534.1±0.5	25 ±3	1534→0	E	-0.5
1545.2±1.5	0.50±0.2			
1555.0±0.8	0.60±0.2			
1571.8±1.0	0.34±0.10			
1574.8±0.8	0.85±0.15	2160→586	γ-γ	-0.4
1634.6±0.7	4.6 ±0.7	3330→1694	γ-γ	+1.1
1644.4±0.8	1.8 ±0.3			
1677.9±1.0	0.40±0.10	3372→1694	E	0.0
1694.3±0.5	26.1 ±2.6	1694→0	E	-0.1
1722.1±1.5	1.3 ±0.2	3719→1999	E	-1.0
1778.2±0.8	4.8 ±0.6	1999→221	γ-γ	-0.2
1789.2±1.0	0.65±0.20			
1826.3±0.8	0.43±0.14			
1832.2±1.5	1.0 ±0.2			
1840.3±0.8	2.8 ±0.4	3534→1694	E	-0.6
1877.3±1.0	0.42±0.14			
1903.8±0.6	5.6 ±0.6	2402→498	γ-γ	-0.4
1927.5±1.0	0.55±0.7	3456→1530	E	-1.6
1934.4±0.8	4.5 ±0.6	2160→221	γ-γ	+0.2

Table 3.7 continued

E_γ (keV)	I_γ	Classification	Basis for Classification	$E_{cal}-E_{obs}$ (keV)
1998.4±1.0	0.88±0.30	1990→0	E	+0.5
2012.3±1.0	9 ±2	2598→586	γ-γ	+0.1
2020.8±1.0	1.6 ±0.3	2598→577	γ-γ	+0.4
2046.0±1.0	1.0 ±0.3			
2100.7±0.7	5.6 ±0.7	2598→498	γ-γ	+0.1
2160.0±0.8	3.1 ±0.6	2160→0	E	+0.5
2239.8±1.5	0.26±0.15			
2249.0±1.0	0.42±0.15			
2322.3±1.0	0.64±0.2	4145→1822	E	+0.7
2335.2±2.0	0.5 ±0.3			
2352.7±1.5	1.4 ±0.4			
2378.1±0.8	4.5 ±0.6	2598→221	γ-γ	-0.5
2401.5±0.8	4.6 ±0.6	2402→0	E	-0.5
2510.8±2.0	1.2 ±0.5			
2535.4±1.5	0.34±0.12	3534→998	E	+0.2
2630.1±1.5	0.69±0.23			
2645.9±1.0	2.6 ±0.4	2867→221	γ-γ	+0.1
2722.3±1.5	0.58±0.2	3719→998	E	-0.9
2752.4±1.0	0.9 ±0.3	3330→577	γ-γ	+0.2
2758.3±1.0	0.55±0.2			
2783.4±0.8	4.7 ±0.6	2783→0	E	0.0
2794.5±1.0	4.4 ±0.6	3372→577	γ-γ	+0.3

Table 3.7 continued

E_γ (keV)	I_γ	Classification	Basis for Classification	$E_{cal}-E_{obs}$ (keV)
2805.9±1.0	0.66±0.2	4341→1534	E	+1.4
2821.2±1.5	0.28±0.14	4845→1325	E	-0.7
2852.0±1.5	1.1 ±0.3	3429→577	γ-γ	0.0
2858.9±1.5	0.27±0.4			
2867.4±0.8	11.0 ±1.5	2867→0	E	-0.5
2872.9±1.0	1.3 ±0.5	4406→1534	E	-0.2
2878.8±1.0	3.0 ±0.6	3100→221	γ-γ	+0.0
3028.6±1.5	2.2 ±0.4			
3099.8±1.5	0.6 ±0.2			
3109.5±1.0	1.7 ±0.3	3330→221	γ-γ	-0.5
3142.0±1.0	6.2 ±0.8	3719→577	γ-γ	-0.3
3220.7±1.5	1.8 ±0.5	3719→498	γ-γ	+0.6
3363.1±1.0	6.2 ±0.8	3363→0	E	-0.1
3372.5±1.0	3.6 ±0.6	3372→0	E	0.0
3401.2±1.5	0.66±0.2	3978→577	E	+0.1
3462.2±1.5	0.68±0.2			
3534.2±0.8	8.2 ±1.0	3534→0	E	0.0
3567.3±1.5	0.33±0.1	4145→577	E	+0.5
3574.0±1.5	0.32±0.15			
3584.9±0.8	1.8 ±0.3			
3719.2±0.6	5.9 ±0.8	3719→0	E	-0.2
3732.5±1.0	1.5 ±0.3			
3782.9±1.0	1.5 ±0.3			

Table 3.7 continued

E_γ (keV)	I_γ	Classification	Basis for Classification	$E_{cal}-E_{obs}$ (keV)
3837.5±1.5	0.50±0.15	4058→221	γ-γ	+0.0
3864.4±1.5	1.0 ±0.2	4341→498	E	+0.4
3901.3±1.5	0.98±0.3	4488→586	E	-0.3
3924.1±1.0	2.9 ±0.5	4145→221	γ-γ	+0.1
3966.3±1.0	1.2 ±0.3			
3978.4±1.5	2.3 ±0.6	3978→0	E	0.0
3996.7±1.5	0.96±0.3	4218→221	γ-γ	+0.8
4048.5±1.5	0.86±0.3			
4082.7±1.5	0.62±0.2			
4185.1±1.5	0.38±0.13	4406→221	γ-γ	+0.3
4340.8±1.0	1.0 ±0.3	4341→0	E	0.0
4448.5±1.5	0.20±0.07			
4487.9±1.0	1.1 ±0.3	4488→0	E	-0.4

* Not observed in singles work (I_γ deduced from γ-γ Ci_j's.)

† See discussion under 586 gate.

view of the poor quality of the Ge(Li) detectors available to these earlier workers, and the fact that they were forced to use NaI(Tl) detectors for their coincidence work, the agreement between the two sets of data is quite surprising. The stripping procedure, which Kitching and Johns were required to use in order to compensate for the inadequate resolution of their detectors, inevitably created weak peaks at certain energies.

A level comparison for beta transitions between the two investigations is listed in table 3.8. The beta gamma coincidence measurements of Kitching *et al*. showed that direct beta transitions occur to the 221 and 577-586 keV levels while this present work indicates an appreciable beta feed to the 577 keV level only. Although the previous workers found considerable feed to their 1533 keV level this is still consistent with the current investigation since the 1530 keV level is mainly beta fed while the 1534 keV level is populated mainly through gamma decay. In summary, it is found that there is almost no direct feed to the 221, 498, 931, 932, 998 and 1534 keV levels, while the levels at 577, 1324, 1530 and 1694 keV are strongly fed by beta decay. Other strongly beta populated levels occur at 2401, 2598, 2867 and 3719 keV.

B. Discussion of Results

Although the current literature available does not permit one to make spin and parity assignments to the levels

TABLE 3.8

Beta Decay Transitions in ^{89}Kr (Previous and Present Work)

Present Work						Kitching and Johns (1967)	
Level	gamma intensities			%		%	
	I_{in}	I_{out}	I_{direct}	β feed	log ft	β feed	log ft
0	-	-	-			<0.1	>8.5
221	107	100	-	<3.0	>8.0	4.0	7.8
498	24.6	22.7	-	<1.0	>8.4	3.3	7.8
577	16.0	40.1	24.1	6.5	7.5	7.5	7.4
586	65.3	72.8	7.5	2.0	8.0	5.0	7.6
931	3.3	4.8	1.5	0.4	8.5	-	-
932	8.6	12.1	3.5	0.93	8.2	-	-
998	17.5	16.9	-	<1.0	>8.2	-	-
1196	12.6	17.2	4.6	1.23	7.9	-	-
1325	17.5	41.2	23.7	6.4	7.1	4.4	7.5
1530	2.7	20.8	18.1	4.9	7.1	4.9	7.1
1534	28.8	28.7	-	<1.0	>8.0	-	-
1694	51.8	111.4	59.6	16.0	6.6	14	6.6
1822	2.0	8.4	6.4	1.71	7.4	-	-
1999	3.1	16.3	13.2	3.5	6.9	3.7	6.9

Table 3.8 continued

	Present Work					Kitching and Johns (1967)	
Level	gamma intensities I_{in}	I_{out}	I_{direct}	% β feed	log ft	% β feed	log ft
2160	7.9	19.4	11.5	3.1	7.0	2.9	7.0
2401	6.2	40.4	28.2	9.7	6.3	8.9	6.3
2598	2.4	69.1	65.7	17.6	5.9	12.3	6.1
2783	-	4.7	4.7	1.26	6.9	-	-
2867	-	22.7	22.7	6.1	6.2	6.0	6.1
3100	0.5	3.0	2.5	0.67	7.0	-	-
3330	3.2	6.7	3.5	0.93	6.6	-	-
3363	2.4	8.2	5.8	1.6	6.6	4.0	5.9
3372	3.4	8.4	5.0	1.3	6.4	-	-
3429	1.3	0.9	-	-	-	-	-
3456	1.0	1.0	-	-	-	-	-
3534	-	12.9	12.9	3.46	5.8	2.9	5.9
3719	-	17.7	17.7	4.7	5.5	2.0	5.9
3978	0.76	3.0	2.2	0.59	6.1	0.5	6.1
4058	0.5	0.5	-	-	-	-	-
4145	-	3.4	3.4	0.91	5.6	0.4	6.0

Table 3.8 continued

	Present Work					Kitching and Johns (1967)	
Level	gamma intensities			%		%	
	I_{in}	I_{out}	I_{direct}	β feed	log ft	β feed	log ft
4218	-	6.8	6.8	1.82	5.2	-	-
4341	-	6.2	5.2	1.66	5.1	0.14	6.1
4406	-	1.7	1.7	0.45	5.4	-	-
4487	-	4.1	4.1	1.1	5.0	0.2	5.6

established in ^{89}Rb, (no reaction studies of any kind have been so far carried out) it is still possible to draw some tentative conclusions concerning the nature of states by using the present measurements, nuclear models and information gained from other sources.

The shell model predicts that the ground state of $^{89}_{37}\mathrm{Rb}_{52}$ is characterized by a $(f\ 5/2)^{-1}$ or $(P\ 3/2)^{-1}$ hole state. In $^{83}_{37}\mathrm{Rb}_{46}$ and $^{85}_{37}\mathrm{Rb}_{48}$, the measured spins of $5/2^-$ indicate that the configuration is $(f\ 5/2)^5\ (P\ 3/2)^4$ while the evidence for $^{87}_{37}\mathrm{Rb}_{50}$ and ^{89}Rb suggests that the configuration is $(f\ 5/2)^6\ (P\ 3/2)^3$. The increased stability of the f 5/2 shell over the P 3/2 shell, as the neutron number increases is rather characteristic of nuclei in this mass range. The configuration of $(f\ 5/2)^5\ (P\ 3/2)^4$ is expected at a very low level of excitation, and the 221 keV state is a good candidate. The 498 keV state deexcites strongly to the ground state and not to the 221 keV state, thereby suggesting that it is the $(f\ 5/2)^6$ $(P\ 3/2)^2\ (P\ 1/2)^1$ configuration. Since there will be a number of very complex excited states associated with such configurations of the form $(f\ 5/2)^6\ (P\ 3/2)\ (P\ 1/2)^2$, or $(f\ 5/2)^5\ (P\ 3/2)^2\ (P\ 1/2)^2$, etc., it seems futile to speculate further with this approach. As an alternative to this type of view, one may consider the coupling of a proton hole or particle states to the vibrational state of a neighbouring even-even nuclear core such as $^{90}_{38}Sr_{52}$ or $^{88}_{36}Kr_{52}$. Here, the association of the $(P\ 3/2)^{-1}$ state to the 2+ first excited vibrational state yields levels of spin $1/2^-$, $3/2^-$, $5/2^-$ and $7/2^-$. Again, complications set in very rapidly so that further conjecture on the basis of the present data cannot be fruitful.

An inspection of log ft values suggests that the beta transitions to states below 2160 keV are first forbidden while many of those to states above this energy are definitely allowed. This indicates that the low lying states populated in beta decay are mainly of positive parity. These must arise from multiproton configurations involving holes in the (d 3/2) state or particles in the (g 9/2), (g 7/2) or (d 5/2) states. The ground state spin-parity of $^{89}_{36}Kr_{53}$ is believed to be $\frac{5}{2}+$ associated with the expected $(d\ 5/2)^3$ configuration involving three neutrons above shell closure.

In order to aid in the accurate determination of spins of levels in ^{89}Rb, it is suggested that gamma-gamma correlation studies and reaction experiments of the type $^{87}Rb(t,p)^{89}Rb$ be carried out.

SUMMARY

The gamma ray transitions in ^{89}Rb following the decay of 3.2 minute ^{89}Kr have been studied by singles and coincidence techniques using high resolution Ge(Li) detectors of various volumes. Thirty-four excited levels in the ^{89}Rb nucleus have been established, of which twenty had been postulated by earlier workers. Out of the 160 gamma rays associated with the decay of ^{89}Kr, 65 transitions have been assigned to the present decay scheme from coincidence evidence while 55 have been placed on the basis of energy sums. Forty weak photons have not been classified.

REFERENCES

Anderson, H.L., Fermi, E., Grosse, A.V. (1941).Phys. Rev. 59, 52.

Archer, N.P. (1965). Ph.D. Thesis, McMaster University.

Archer, N.P., Keech, G.L. (1966). Can. J. Phys. 44, 1823.

Arya, A.P. (1966). "Fundamentals of Nuclear Physics", Allyn and Bacon, Boston.

Ball, J.B., Johns, M.W., Way, K. (1970). Nuclear Data Tables A8, 407.

Bernthal, F.M. (1969). Ph.D. Thesis, UCRL-18651.

Bevington, P.R. (1969). "Data Reduction and Error Analysis for the Physical Sciences", McGraw-Hill Book Co. Inc., Toronto.

Blatt, S.L. (1967). Nucl. Inst. Meth. 49, 235.

Bohr, A., Mottelson, B.R. (1953). H. Danske Vidensk. Selsk. Mat.-Fys. Medd. 27, No. 16.

Brennan, M.H., Bernstein, A.M. (1960). Phys. Rev. 120, 927.

Camp, D.C. (1967). UCRL Report 50156.

Camp, D.C., Meredith, G.L. (1971). Nuc. Phys. A166, 349.

Campbell, J.L., Smith, H.J. Mackenzie, I.K. (1971). Nucl. Inst. Meth. 92, 237.

Carlson, G.C., Schick, W.C., Jr., Talbert, W.L., Jr., Wohn, F.K. (1969). Nuc. Phys. A125, 267.

Carraz, L.C. Monnand, E., Moussa, A. (1971) Nuc. Phys. A171, 209.

Chase, R.L. (1962). "Nuclear Pulse Spectroscopy", McGraw-Hill Book Co. Inc., Toronto.

Chase, G.D., Rabinowitz, J.L. (1967). "Principles of Radioisotope Methodology", Burgess Publishing Co., Minneapolis.

Christy, R.W., Pytte, A. (1965). "The Structure of Matter: An Introduction to Modern Physics", W.A. Benjamin, Inc., New York.

Cowan, C.L., Reines, F. (1957). Phys. Rev. 107, 528.

Davisson, C.M. (1966). Alpha, Beta, and Gamma Ray Spectroscopy", ed. K. Siegbahn, Vol. 1, North-Holland Publishing Co., Amsterdam.

De-Shaltt, A. (1961). Phys. Rev. 122, 1530.

Dillard, J.W., Adams, R.M., Finston, H., Turkevich, A. "Radio-Chemical Studies 'The Fission Products'", C.D. Coryell, and N. Sugarman, ed. National Nuclear Energy Series, Plutonium Project Record, McGraw-Hill Book Co. Inc., New York.

Eisberg, R.M. (1964). "Fundamentals of Modern Physics", John Wiley and Sons, Inc., New York.

Enge, H.A. (1966). "Introduction to Nuclear Physics", Addison-Wesley (Canada) Limited, Don Mills.

Ewan, G.T., Graham, R.L., Mackenzie, I.K. (1966). IEEE, Trans. Nucl. Sci. NS-13(3), 297.

Fano, V. (1947). Phys. Rev. 72, 26.

Fermi, E. (1934). Zeits. f. Phys. 88, 1961

Fiedler, H.J. (1966). Private communication.

Gibson, W.M., Miller, G.L. Donovan, P.F. (1966). "Alpha, Beta, and Gamma Ray Spectroscopy", ed. K. Siegbahn, Vol. 1, North-Holland Publishing Co., Amsterdam.

Goodman, C.D., Hughes, T.A., Johns, M.W. (1970). Nuclear Data Tables A8, 345.

Goulding, F.S. (1966). "Alpha, Beta, and Gamma Ray Spectroscopy", ed. K. Siegbahn, Vol. 1, North-Holland Publishing Co., Amsterdam.

Goulding, F.S. (1964). IEEE Trans-Nucl. Sci. NS-11(3), 177.

Gove, N.B. (1966). "Nuclear Spin-Parity Assignments", Academic Press, New York.

Graham, R.L., Machenzie, I.K., Ewan, G.T. (1966). IEEE. Trans. Nucl. Sci. NS-13(1), 72.

Green, A.E.S., Sawada, T. Saxon, D.S. (1968), "The Nuclear Independent Particle Model", Academic Press, New York.

Hahn, O., Strassemann, F. (1939). Die Naturwissen Schaften 27, 11.

Haxel, O., Jensen, J.H.D., Suess, H.E. (1949). Phys. Rev. 75, 1766.

Haxel, O., Jensen, J.H.D., Suess, H.E. (1950). Z. Physik 128, 295.

Heath, R.L. (1964). AEC Report IDO-16880-1.

Hofstetter, E.M. (1964). "The Mathematics of Physics and Chemistry", ed. H. Margenau and G.M. Murphy, Vol. 2, D. Van Nostrand Co. Inc., Toronto.

Johns, M.W., Park, J.Y., Shafroth, S.M., Van Patter, D.M. (1970). Nuclear Data Tables A8, 373.

Katcoff, S. (1960). Nucleonics 18, November, 201.

Kitching, E.J. (1966). Ph.D. Thesis, McMaster University.

Kitching, J.E., Johns, M.W. (1966). Can. J. Phys. 44, 2661.

Kitching, J.E., Johns, M.W. (1967). Nuc. Phys. A98, 337.

Koch, R.C., Grandy, G.L. (1960). Nucleonics 18, July, 76.

Kofoed-Hansen, O., Nielson, K.O. (1951). Phys. Rev. 82, 96.

Kotani, T., Ross, M. (1959). Phys. Rev. 113, 622.

Lederer, M.C., Hollander, J.M. Perlman, I. (1968). "Table of Isotopes Sixth Edition", J. Wiley & Sons, Inc., New York.

Lee, T.D., Yang, C.N. (1956). Phys. Rev. 104, 254.

Lycklama, H., Archer, N.P., Kennett, T.J. (1969). Can. J. Phys. 47, 394.

Lycklama, H., Kennett, T.J. (1970). Can. J. Phys. 48, 754.

Malmstadt, H.V., Enke, C.G., Toren, E.C. (1963). "Electronics For Scientists", W.A. Benjamin, Inc., New York.

Marion, J.B. (1968). Nuc. Data 4, 308.

Mason, J.F., Johns, M.W. (1970). Can. J. Phys. 48, 2056.

Mason, J.F., Johns, M.W. (1970). Can. J. Phys. 48, 2895.

Mayer, M.G. (1949). Phys. Rev. 75, 1969.

Mayer, M.G. (1950). Phys. Rev. 78, 16.

Mayer, M.G., Jensen, J.H.D. (1966). "Alpha, Beta, and Gamma Ray Spectroscopy", ed. K. Siegbahn, Vol. 1, North-Holland Publishing Co., Amsterdam.

Meitner, Lise., Frisch, O.R. (1939). Nature 143, 239.

Melissinos, A.C. (1966). "Experiments In Modern Physics", Academic Press, New York.

Merzbacher, E. (1961). "Quantum Mechanics" John Wiley & Sons, Inc., New York.

Miller, G.L., Gibson, W.M., Donovan, P.F. (1962). Ann. Rev. Nuc. Sci., ed. E. Segre, 12, Annual Reviews, Inc., Palo Alto, Cal.

Moszkowski, S.A. (1966). "Alpha, Beta, and Gamma Ray Spectroscopy", ed. K. Siegbahn, Vol. 2, North-Holland Publishing Co., Amsterdam.

Norris, A.E., Wahl, A.C. (1966). Phys. Rev. 146, 146.

Ochenden, D.W., Tomlinson, R.H. (1962). Can. J. Chem. 40, 1594.

Ortec. (1970). "Timing With Ge(Li) Detectors", Application Note 13, Ortec, Inc., Tenn.

Ouseph, P.J., Schwartz, M. (1970). Phys. Teach. 7, 374.

Pauli, W. (1934). Rapports Du Septieme Conseil De Physique Solvay, Brussels, 1933, Paris: Gauthier-Villars Et Cie.

Powell, J.L., Crasemann, B. (1961). "Quantum Mechanics" Addison-Wesley Publishing Company, Inc., Reading, Mass.

Prakash, S. (1960). Z. Electrochem. 64, 1037.

Preston, M.A. (1962), "Physics of the Nucleus", Addison-Wesley Publishing Co. Inc., Reading, Mass.

Segre, E. (1964). "Nuclei and Particles", W.A. Benjamin, Inc., New York.

Smith, H.J. (1972). Private communication.

Tavendale, A.J. (1967). Ann. Rev. Nuc. Sci., ed. E. Segre, 17, Annual Reviews, Inc., Palo Alto, Cal.

Talbert, W.L., Jr. Duke, C.L., Nielsen, K.B. (1969). Private communication.

Wahl, A.C., Ferguson, R.L., Nethaway, D.R., Troutner, D.E., Wolfsberg, K. (1962). Phys. Rev. 126, 1112.

Wahl, A.C., Norris, A.E., Ferguson, R.L. (1966). Phys. Rev. 146, 931.

Wahlgren, M.A., Meinke, W.W. (1962). J. Inorg. Nucl. Chem. 24, 1527.

Walter, F.J., Moore, B.J. (Nov. 1968). Paper Given at "68 Eastern Analytical Symposium".

Weisskopf, V.F. (1951). Phys. Rev. 83, 1073.

Williams, G.N., McPherson, D. (1968). Chalk River Nuclear Laboratories (CRNL) Progress Report #PR-P-76.

Wolfsberg, K. (1965). Phys. Rev. 137, B929.

Wu, C.S., Ambler, E., Hayward, R.W., Hoppes, D.D., Hudson, R.P. (1957). Phys. Rev. 105, 1413.